REPRESENTATION OF PLUME DYNAMICS BY MITRAL AND TUFTED CELLS IN THE FIRST RELAY OF MOUSE OLFACTORY PROCESSING

Suzanne Michelle Lewis

A dissertation

submitted in partial fulfillment of the

requirements for the degree of

Doctor of Philosophy

University of Washington

2022

Reading Committee:

David Gire, Chair

Sheri Mizumori

Andrea Stocco

Program Authorized to Offer Degree:

Department of Psychology

University of Washington

Abstract

Representation of Plume Dynamics by Mitral and Tufted Cells in the First Relay of Mouse Olfactory Processing

Suzanne Michelle Lewis

Chair of the Supervisory Committee:

David Gire

Department of Psychology

In ethologically relevant environments odor molecules travel in plumes. As a result, an odor does not diffuse slowly through the air, but rather is pulled and pushed stochastically away from its source in discrete filaments. From the perspective of an olfactory searcher, filaments are experienced as discrete whiffs of odor. The frequency, strength, and duration of whiffs contain information regarding an odor and the location of its source. Thus, the spatiotemporal dynamics of plumes are theoretically informative tools for olfactory search, but it is unclear how these complex cues are used by mice to create internal representations of their odor environments. In the past, recording from plumes without disruption their dynamics has been difficult. Thus, simultaneously obtaining neural recordings of olfactory processing in the first olfactory relay, the olfactory bulb (OB), and odor recordings of the concentration of natural stimulus as it changes over time has been difficult. This dissertation investigates methods of exploring the response of the OB to natural odor scenes. We used wide-field imaging to examine the collective responses of mitral and tufted cell (MTC) activity in the dorsal OB. We segmented MTC activity into

glomerular complexes and found that some complexes were significantly correlated with odor concentration across plume encounters. The magnitude of this correlation with plume dynamics, or plume following ability, was positively associated with more reliable responses and stronger response dynamics. Thus, these recordings determine that plume dynamics play an important role in structuring information processing in the OB. We also used new high-density Neuropixel 2.0 probes to perform electrophysiological recordings of OB activity at the cellular level during plume presentation, establishing a method for examining how this plume following behavior of glomeruli related to the individual cells that make up glomeruli. This approach could help determine if observed plume following in wide-field recordings is due to similarly tuned MTCs or is the collective result of MTCs heterogeneously tuned to dynamic features of plumes. For the Neuropixels recordings we also propose the use of correlated changes between different LFP frequency domains to locate the position of the mitral cell layer (MCL) along the electrode array. Theta oscillations, gamma oscillations, and spiking activity all have characteristic changes observable near the mitral cell layer (MCL). Thus, the MCL was located by identifying coincident locations where theta and gamma power dipped and spiking power began to rise. The switch from isolated features to natural odor scenes has been important in the study of visual processing. In this dissertation we study neural responses in the first olfactory relay in mice as they process the full complexity of natural odor scenes, plumes.

TABLE OF CONTENTS

LIST OF FIGURES

LIST OF TABLES

ACKNOWLEDGEMENTS

I am grateful for the patience and mentorship many people have shown me throughout graduate school. Thank you to my advisor David Gire for your mentorship. You encouraged new ideas, helped me interpret and convey the bigger picture of the data, and pushed me to have confidence in my work. Thank you to all the members of the Gire Lab for helpful conversations and feedback. Thank you to my research assistants, Jin Young Park, Lai Xu, and Lucas Suarez, for all your help.

Thank you to Merav Stern for your friendship and mentorship.

Thank you to our collaborators Nicola Rigolli and Agnese Seminara for your help and for all the fun Zoom meetings talking about plumes.

Thank you to Nick Steinmetz for your mentorship and advice on data analysis, and thank you to the Steinmetz Lab for advice on our Neuropixels setup and analysis pipeline.

Thank you to Kelly Chang for your friendship and advice about life and about statistics. Thank you to Katie Johnson and Pratik Sachdeva for making the summer workshop fun and the conferences after the workshop something to look forward to.

Thank you to my family and friends for your support. Especially my parents, Kevin, and Sammy.

Thank you to everyone on my committee, David Gire, Sheri Mizumori, Andrea Stocco, Eric Shea-Brown, and Bing Brunton, for all your guidance.

Chapter 1. Introduction

1.1 Plume cues carry information of odor source location

In ethologically relevant environments, odor molecules travel in plumes. At a scale relevant to rodents, turbulence governs the transport of the plume and its contained odors. This turbulence causes transport to occur predominantly via dispersion as opposed to passive diffusion (Wright & Thomson, 2005). In the absence of dispersion, odors diffuse into concentration gradients where navigation can be achieved by monotonic concentration ascent, but dispersion complicates odor environments. Rather than a continuous signal, olfactory searchers experience plume intermittently and often sparsely (Celani et al., 2014; Mylne & Mason, 1991). Within the range of the plume, the searcher experiences a series of filament encounters, resulting in whiffs, odor on, and blanks, odor off, periods. Simple search strategies dependent on odor concentration comparisons are used by bacteria to traverse concentration gradients(Vladimirov & Sourjik, 2009), but these strategies are not sufficient to explain the speed with which we observe mice navigating to odor sources (Boie et al., 2018; Gumaste et al., 2020). Some of the plume dynamics experienced by the animal, the timing and intensity of the odor concentration dynamics, have been shown to inform odor source location (Boie et al., 2018; Rigolli et al., 2021; Webster & Weissburg, 2001). Additionally, plume dynamics are hypothesized to inform decision making during navigation (Mafra-Neto & Carde, 1994; Pang et al., 2016; Vickers, 2000). Therefore, much ethologically inspired research in olfaction works to quantify the statistics of plume dynamics and understand how informative they may be for odor-guided navigation.

To understand what plume features may be efficient tools for olfactory searchers, we must first identify statistically reliable features of olfactory space. Plume dynamics are complex

and odor concentration levels de-correlate even on small spatial scales (Vickers, 2000). Dispersion and diffusion create fluctuations across the plume, which are experienced by an animal moving through the plume as unpredictable durations of odor presence with stochastic levels of odor concentration (Schikorski & Stevens, 1999). Despite this complexity, there exist statistical regularities. Particularly, there is organization to how odor dynamics evolve across space as one moves further away from an odor source (Boie et al., 2018; Celani et al., 2014; Connor et al., 2018; Justus et al., 2002; Mylne & Mason, 1991; Yeung & Pope, 1992). Thus, relevant concentration dynamic features could theoretically provide cues for olfactory searchers, but which spatiotemporal features are utilized by navigating mammals is still not yet fully understood.

It is important to first understand the larger architecture of the plume before discussing what dynamical features may be efficient cues for olfactory navigators. In airborne settings, plumes are conical in nature (Rigolli et al., 2021). The cone does not represent the boundaries of a continuous odor cloud, but rather the area in which an odor encounter is reasonably likely, and thus is sometimes referred to as the 'cone of detection' (Celani et al., 2014; Rigolli et al., 2021). Near the odor source, relative to the longitudinal axis of the plume, the frequency of odor whiffs is higher (Mylne & Mason, 1991), and the peak concentration of whiffs is stronger (Figure 1.1) (Webster et al., 2001). As one traverses downwind away from the source, whiffs begin to spread apart (Murlis et al., 1992) and each whiff expands (Young et al., 2020) resulting in a more diluted plume. Put another way, both blank and whiff duration increase. This results in a decrease in whiff frequency. In ethologically relevant odor environments, far from the odor source downwind, the whiff expansion leads to an overall decrease in plume sparsity (Murlis et al., 1992; Rigolli et al., 2021). Thus, downwind distance from the odor source leads to

predictable changes in the plume dynamics, providing a possible source of information for navigators.

In addition to downwind changes, the plume also has crosswind organization. For a circular cross-section of the plume, if one moves from the center to the edges of the cross-section, or in a crosswind direction, dynamics transition, and do so at a faster rate than changes observed when moving downwind. This is due in part to the fact that transitions from mean concentration at the midline to zero concentration at the edges must occur within the radius of the crosswind section. Moving crosswind results in decays in whiff duration and increases in whiff frequency near the plume edges. The rate of change in whiff duration is superlinear moving toward the edges such that changes occur most rapidly closest to the edge (Celani et al., 2014; Mylne & Mason, 1991). Unlike moving downwind though, this decrease in average concentration is driven less by a decrease in peak concentration and more by decreasing whiff durations and increased sparsity (Mylne & Mason, 1991). As sparsity is lowest and whiffs are longest along the midline, the odor is above a detectable threshold most often there (Mylne & Mason, 1991; Rigolli et al., 2021). Another change that occurs when moving crosswind is an increase in the intensity of odor fluctuations (Murlis et al., 1992; Mylne & Mason, 1991). Taken together this means that the decrease in whiff duration and increase in sparsity is paired with an increase in whiff frequency when moving crosswind. Therefore, both longitudinal and crosswind plume dynamics vary as a function of position relative to odor source, although which features provide efficient measures for searchers to estimate their position within the plume is still under investigation.

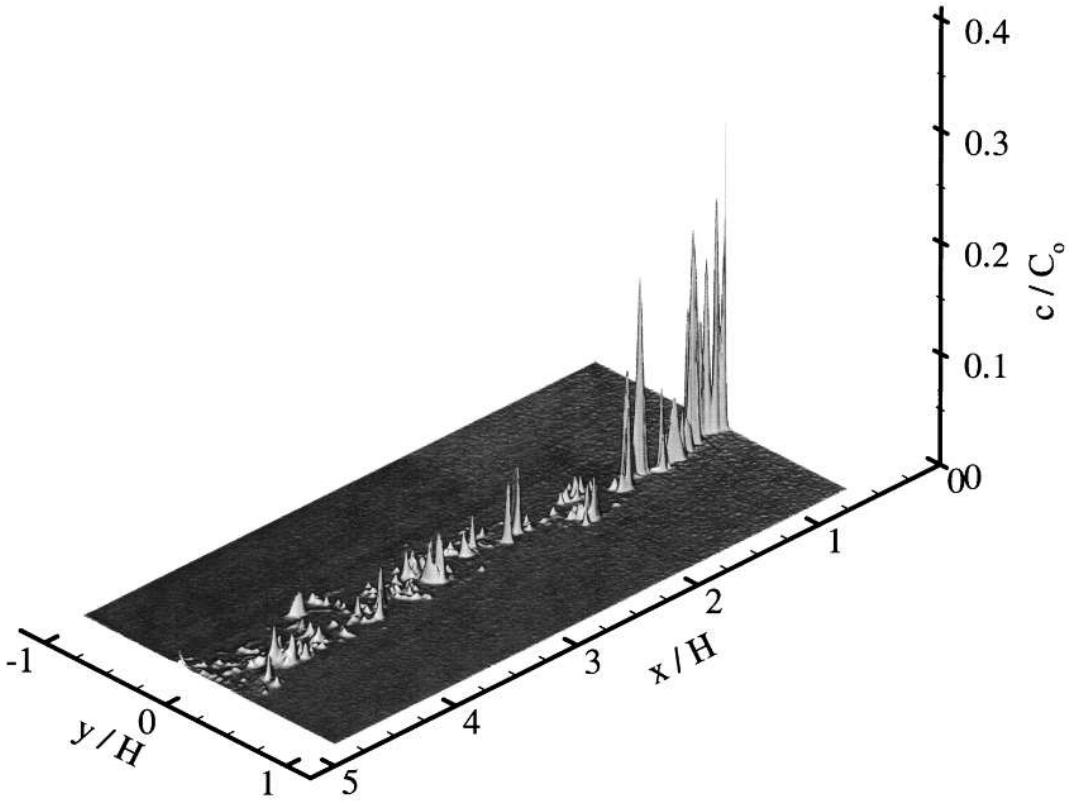

Figure 1.1: Example of instantaneous concentration field of a plume.
The plotted instantaneous concentration field example from a plume exhibits an example of how the plume is experienced by a searcher as intermittent, and the magnitude of encounters changes depending on the searchers position relative to the plume's source. x/H plots downwind distance from the odor source (at the origin) and y/H plots cross wind displacement. The magnitude of concentration is plotted as $\frac{c}{C_0}$ where magnitude is normalized by C_0, the concentration at the source. Figure used with permission from (Webster et al., 2001).

Spatiotemporal features are generally divided into two classes, intensity cues and timing cues (Celani et al., 2014; Rigolli et al., 2021). Intensity cues can provide a sufficient strategy for many animals navigating laminar flow, which occurs close to the ground floor or on small scales within plumes. The bacterium Escherichia coli is a classic example of an animal that uses intensity cues in laminar flow to follow concentration increases to an odor source (B. Hu & Tu, 2014). In their environment, odor plumes consist of stable concentration gradients, such that an increase in intensity is a strong signal that the bacterium has moved closer to an odor source. In the case of airborne plumes, odor is moved predominantly by dispersion as opposed to passive diffusion (Celani et al., 2014; Yeung & Pope, 1992). As a result, odor concentration is highly varied as measured from any single position within the plume (Mylne & Mason, 1991). Thus, a single intensity measurement reduces less uncertainty about source location than it would in laminar flow. Were the mouse to sample for seconds, it could resolve a concentration gradient similar to laminar flow over time (Webster & Weissburg, 2001) and avoid the uncertainty of intensity and timing features of plume dynamics. This is unlikely though as mice navigate on a faster timescale than would be required to resolve a concentration gradient (Boie et al., 2018). Therefore, mice seem to utilize plume dynamics to navigate to odor sources.

Intensity cues are known to be important for plume navigation, despite the fact that their standard deviation usually exceeds the mean when measured across much of the plume (Mylne & Mason, 1991; Webster & Weissburg, 2001). Mice are thought to sample odor using both in stereo, simultaneous comparisons between nares, and serial, sniff to sniff, comparisons. Sampling intensity cues in stereo is not thought to be the dominant cue utilized by mice tracking plumes, but is hypothesized to play a role in olfactory tracking behavior (A. Liu et al., 2020). It has also been shown that mice are capable of making binasal intensity comparisons and do so when

tracking trails of odor on the ground (P. W. Jones & Urban, 2018). Recent research compared the performance of both modeled and robotic searchers to mice on an odor localization task using intensity cues. Modeled and robotic searchers were equipped with stereo intensity comparisons (and wall-avoidance) to determine their navigation decisions. All three searcher groups achieved similar success for the simpler plume dynamic condition, but when dynamics were made to be more turbulent and complex, the mouse showed no change in performance but the performance of modeled and robotic searchers dropped. This finding suggests that stereo intensity comparisons are theoretically useful for olfactory search, but their informative value is not robust across environmental conditions, and not the sole cue used by navigating mice. Another odor localization study tested the importance of stereo intensity cues directly and found they are not necessary for mice tracking air-borne odors (Findley et al., 2021). Findley et al., found that mice navigating with only one functioning nostril suffer no cost to their search efficiency. Together this research suggests that stereo intensity sampling theoretically informs odor location, and may be an employed, though not necessary, cue for mice tracking air-borne odors.

Serial sampling of intensity cues refers to the comparison of odor concentration across multiple sampling cycles, or sniffs in the case of the mouse. As peak concentration of odor whiffs decreases only the longitudinal axis of the plume, comparing odor concentration across sniffs may help an animal determine its relative position within the plume. Considering both the concentration intensity between consecutive sniffs and the distance traveled between those sniffs, a mouse can gain information about its relative position within the plume (Jacobs, 2012; A. Liu et al., 2020). In mice, serial intensity comparisons have been shown to be informative (A. Liu et al., 2020; Rigolli et al., 2021) and employed (Findley et al., 2021). In fact, the comparison of intensity between subsequent sniffs, or the direction and magnitude of odor change, was found to

be directly encoded in early olfactory cortex (Parabucki et al., 2019). Therefore, both stereo and serial intensity samples of odor concentration levels are likely utilized by mice. Combining the two methods has been shown to increase the accuracy of odor search estimates (Boie et al., 2018). This suggests intensity cues are important for odor localization as sampled over both the spatial, in stereo, and temporal, serial, structure of the plume.

Another class of cues, timing cues, is important for navigators. This class of cues is defined by the temporal features of odor events. For example, whiff frequency is a timing cue defined by the rate at which odor is encountered and does not consider the odor concentration level of the whiff. *Mustelus canis* sharks use fine scale timing cues for olfactory search, as their turning behavior is moderated by arrival time differences between their nares, rather than intensity differences (Gardiner & Atema, 2010). This preference for a timing cue over an intensity cue remained even when concentration levels differed by two orders of magnitude. Some timing cues have been shown to be more robust than intensity cues with respect to changes in odor source properties or environmental properties, such as how much odor is released at the odor source or the flow rate of the plume (Park et al., 2016).

One timing cue known to be of particular importance is whiff frequency. As mentioned previously, whiff frequency is higher near the odor source and decreases moving downwind or crosswind from the source (Mylne & Mason, 1991). Because frequency decreases faster across space at the plume edges, these zones can be particularly informative as the frequency difference measured between two points set at a fixed distance apart is greater and likely may provide a more sensitive measure for distance estimates. In fact, computational modeling using aquatic plumes determined that navigation guided by whiff frequency comparisons resulted in the average search trajectory navigating first to the edge of the plume, and then following the plume

edge to the source (Michaelis et al., 2020). Whether mice utilize frequency of whiff detection in olfactory search is not yet clear, but some animals display search behavior reliant on this timing cue. In some species of moth, for example, the frequency of odor whiffs is known to be important (Vickers & Baker, 1996) or even necessary (T. C. Baker et al., 1985; Lei et al., 2009; Mafra-Neto & Carde, 1994) for successful olfactory search. Moths will surge upwind toward an odor source as long as odor filaments are encountered within a certain frequency range. If the odor becomes too sparse or too constant, a behavioral switch is made to cast crosswind until sufficient intermittency ranges are again detected (Vickers, 2006). Whiff frequency increases were also shown to moderate movement in walking flies engaged in plume-guided navigation (Demir et al., 2020). Higher whiff frequency biased the animals towards more walking behavior as compared to lower whiff frequency. Thus, the timing with which an animal encounters odor within a plume has been determined to provide important cues to moderate search behavior for some species. Therefore, whiff frequency informs odor source location and seems to be more informative at plume edges where whiff frequencies decreases quickly and odor fluctuations are stronger, meaning transitions between blanks and whiffs are steeper.

Other important timing cues known to vary with distance from an odor source include whiff and blank duration and intermittency (Celani et al., 2014; Jacob et al., 2017). Whiff and blank duration both increase at a similar rate moving away from the odor source (Celani et al., 2014) and have been shown to inform and help predict odor source location (Rigolli et al., 2021). Intermittency is the proportion of time the odor is detectable. (Intermittency is also defined as the portion of time odor is below a detection threshold or as whiff frequency, but this work will only define intermittency as the proportion of time odor is above a detectable threshold.) Intermittency is highest near the midline of the plume where odor is above a detectable threshold

most frequently. Thus, timing cues are robust across plume conditions, informative for the search strategy of some species, and theoretically inform odor location.

The fact that intensity and timing features vary in their relevance across the plume's structure suggest that using only one feature may not be optimal. Likely, the olfactory search strategies of efficient searchers, like mice, use some combination of timing and intensity cues. Mentioned previously, whiff frequency-driven navigation resulted in edge-following behavior in the Michaelis et al., study. In the same study, when searchers used only stereo odor concentration comparisons, searchers first navigated to the center of the plume (where odor concentration is detected more often) before navigating upstream to the source (Michaelis et al., 2020). In this case, it is possible that using both intensity and whiff frequency cues may have allowed searchers to navigate efficiently toward the odor source without having to first relocate within the plume. Rigolli et al,. found that in general, intensity cues outperformed timing cues when modeled searchers were tasked with estimating the location of an odor source using turbulent plume dynamics. When they used a mixture of timing and intensity cues though, the features utilized in tandem show better search performance than either class in isolation (Rigolli et al., 2021). Combining one intensity cue, either absolute concentration or change in concentration, with one timing cue, either whiff duration, blank duration or intermittency, improved location estimates. Thus, optimal and flexible navigation of turbulent plumes may necessitate the use of multiple dynamical features.

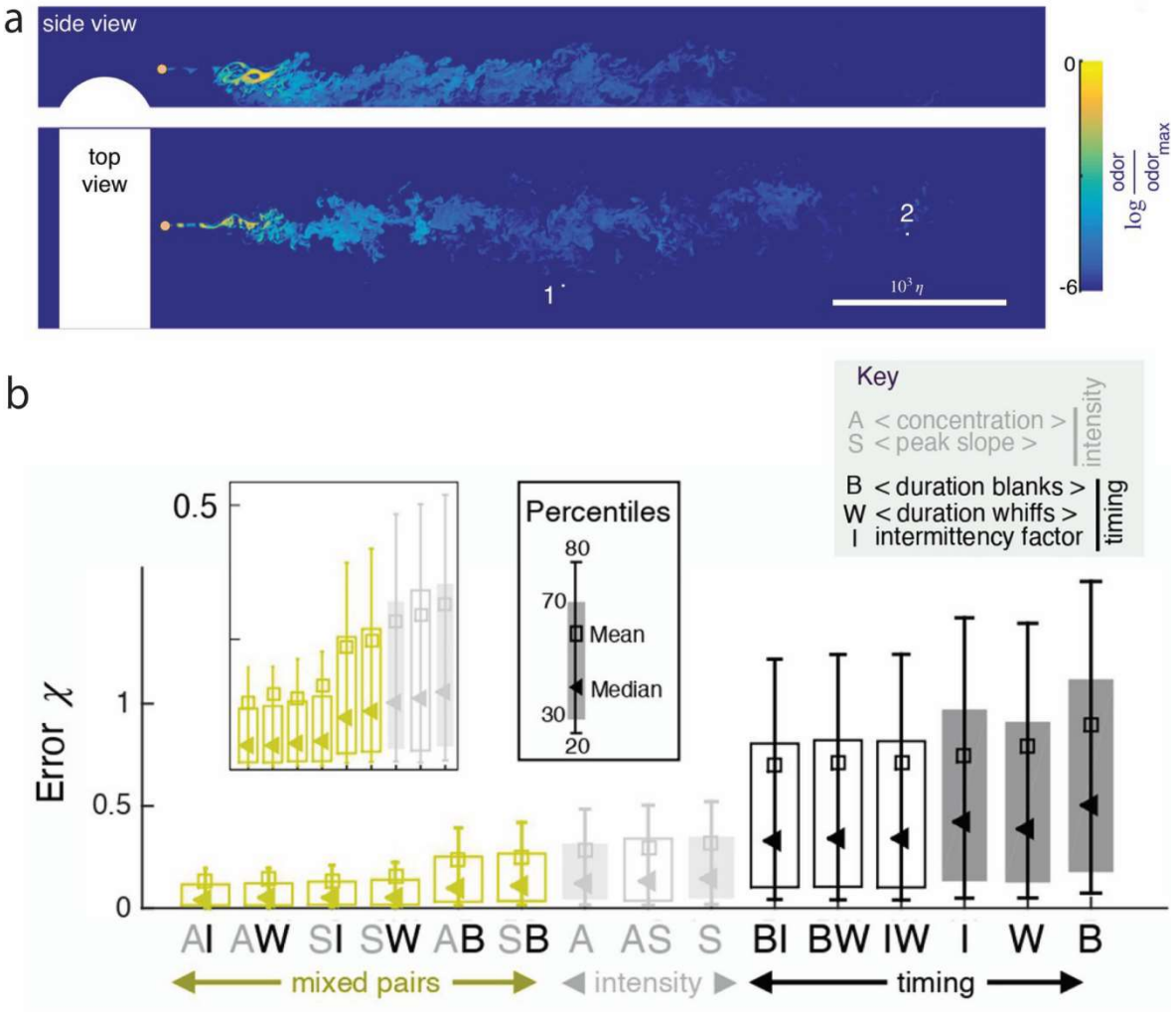

Figure 1.2: Timing and intensity features of turbulent plume dynamics differentially inform odor source location.

a) Snapshot of an odor concentration field of a turbulent plume from the side view (top) and the top view (bottom) at the height of the odor source**.** Odor concentration is plotted as the log of the odor concentration normalized by the max odor concentration. **b)** To determine if different cues provide information of odor source location, a machine learning algorithm that predicted odor source location using different features of plume dynamics was used. The error between the estimated source location and actual source location was used as an indicator for the efficiency of the features(s) to provide information on odor source location. Here the predicted error *x* of different timing and intensity features or combinations of features is plotted showing that intensity features outperform timing features, but that pairing an intensity feature with a timing feature outperforms either type in isolation. Figure generated from Figure 1B,C and Figure 4A and is used with permission from (Rigolli et al., 2021).

Despite uncertainty regarding the full features space of plume dynamics, computational work has clearly shown that plume dynamics can theoretically inform olfactory searchers. Understanding how well early mammalian olfactory cortex resolves odor dynamics as they evolve over time will determine what types of cues are available to navigating mice and possibly restrict the search of the complex feature space of plumes. This in turn may help to guide the design of future studies to probe how the availability or loss of these cues affect plume guided navigation. This body of work will focus on how excitatory populations in the OB, the first olfactory relay in mice, respond to and are moderated by plume dynamics.

1.2 Early Olfactory Processing

How mice detect and process odorants in the environment will determine how well they are able to resolve the odor concentration dynamics of the plume. Odorants first bind to receptors inside the nose and then these receptors send information to the first olfactory relay of mice, the main olfactory bulb (OB). Inside the OB the signal is processed and then relayed to multiple higher-level areas of the olfactory cortex.

A rodent does not passively and continuously sample odorants in the environment, but rather, they must sniff to draw packets of odor into the nose. Thus, olfaction is a largely discrete and active sensing process where both airflow (Wu et al., 2017) and the speed with which an animal sniffs (Carey & Wachowiak, 2011) are shown to affect the activity of primary sensory neurons and neurons in the first relay of olfactory processing, respectively. Sniffing is further related to olfactory processing in that individual cells can be more likely to fire during certain phases of the sniff cycle than others (Ackels et al., 2020; Fukunaga et al., 2012). Thus, the manner in which odor is actively sampled from the environment is one of the first moderators of early olfactory processing.

Olfactory encoding begins with odor transduction. Once odorants have been drawn into the nasal cavity of a rodent, they arrive at the epithelial surface. Embedded in the epithelial surface are olfactory sensory neurons (OSNs) which bind to physical features of the odorant proteins. Each OSN expresses one type of olfactory receptor (OR) gene (Buck, 2004), of which there are approximately 1000 different types (Ressler et al., 1994). OSNs transduce odorants when their receptor sites bind to a molecular feature of an odorant (Gaillard et al., 2002). Binding is not a deterministic event but occurs at a probability dependent largely on binding affinity, the compatibility of fit between an odorant feature and a receptor site (Kajiya et al., 2001; Katada et al., 2005). A single feature is compatible with multiple ORs, and a single OR can bind multiple molecular features (Kajiya et al., 2001; Katada et al., 2005; Malnic, 2007; Vassar et al., 1994). Thus, each odor is encoded by an OSN ensemble, where the members of the ensemble inform the likelihood of some set of odorant features present at the nasal epithelium. OSNs responding the fastest and strongest within the ensemble indicate that the odorant features to which they have the highest binding affinity are the most likely to be present at the surface. Thus, odor identity is not directly encoded, but is inferred based on which OSNs activate, how strongly they activate, which library of features each OSN binds, and the respective affinity for each possible binding combination.

Once an ensemble of OSNs has been activated, they convey the signal to the OB, the first relay of olfactory processing. The OB is a laminar structure, and its allocortex is divided into six main layers (though this is not to be confused with the six classical layers of neocortex) (Figure 1.3) (Shipley & Ennis, 1996). From superficial to deep, the layers are: olfactory nerve layer (ONL), glomerular layer (GL), external plexiform layer (EPL), mitral cell layer (MCL), internal plexiform layer (IPL), and granule cell layer (GCL). Input from the OSNs enters the OB by first

traveling through the superficial ONL. The ONL has no somas but consists entirely of OSN afferent axons. OSN axons continue to travel deeper, extending inward toward the GL until their terminal boutons synapse onto principal neurons in spherical structures of neuropil called glomeruli. Within each glomerulus, thousands of OSN axons (Schoppa & Urban, 2003) of the same receptor type converge onto tens of excitatory output cells of the OB (Nagayama et al., 2014; Ressler et al., 1993). These glomeruli have strong topographic organization due to the exclusive nature of all OSNs within the same glomerulus expressing the same OR. As a result, activation of a single glomerulus is driven only by a single type of OR activation (Buck, 2004). In this way, a set of OSNs active on the epithelial surface is converted to a topographical map of activated glomeruli across the GL of the OB. Since the odorant features with the highest binding affinity bind first to their respective ORs, the order of glomerular activation is related to binding affinity and thus informs the likelihood with which certain molecular features may be present at the epithelial surface. Therefore, odor identity is encoded by spatiotemporal maps of glomerular activation as both the ensemble and the activation order of glomeruli convey information about identity (Spors & Grinvald, 2002).

Glomeruli occupy the bulbar layer named after them, the GL (Figure 1.4), and the cells that innervate glomeruli are hypothesized to function as a unit (Wachowiak et al., 2004). OSN inputs to the glomerulus are similar (Wachowiak et al., 2004), and some response properties of output cells are correlated (Arneodo et al., 2018; Dhawale et al., 2010; Schoppa & Westbrook, 2001). Also, OSN input drives glomerular activation in a more binary manner, and cells associated with a given glomerulus tend to activate as a group (Gire & Schoppa, 2009). Therefore, encoding of odor identity and odor properties is often considered at the glomerular level as well at the cellular level.

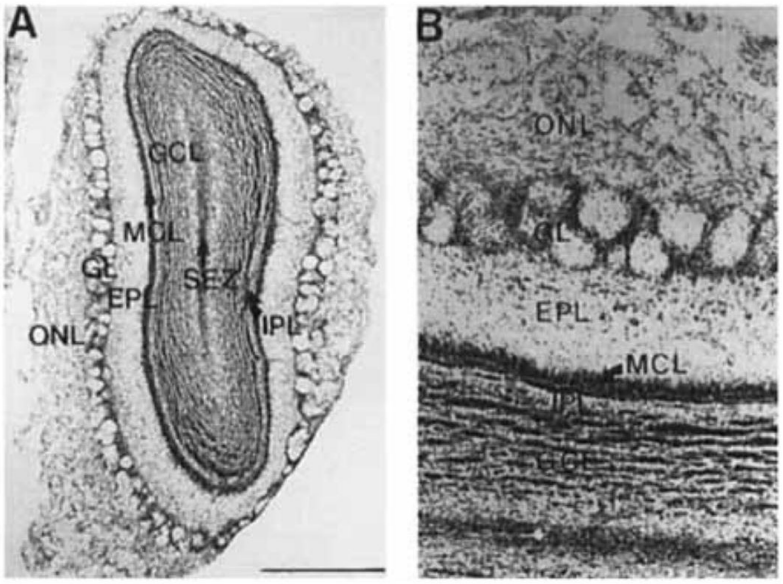

Figure 1.3: Layers of the OB Depicted Across a Coronal Section.
a) Cresyl violet stained, coronal section of the OB depicts the OB layers (ONL, GL, EPL, MCL, IPL, GCL) as well as the (SEZ, subependymal zone). b) A close up along the superficial edge of the OB shows a close up of the layers. Figure from (Shipley & Ennis, 1996) and used with permission.

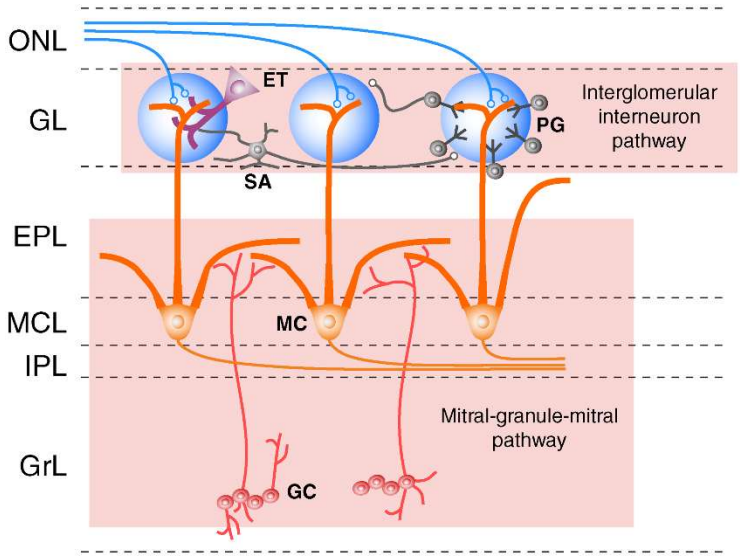

Figure 1.4: Interglomerular pathways of the main olfactory bulb circuit.
a) A schematic depicting connectivity between the major cell types across the layers of the OB (with the exception of TC somas know to populate the EPL). Figure from (Uytingco et al., 2016), and reused following the guideline of its Creative Commons Attribution 4.0 International License.

Glomeruli have both excitatory and inhibitory neurons which help coordinate their activity, facilitating their ability to function as a single unit for olfactory coding (Homma et al., 2013). Juxtaglomerular interneurons have somas located in the interglomerular space of the GL and moderate intraglomerular and interglomerular processing, but do not project to upstream cortex. Three main juxtaglomerular cells are periglomerular cells (PGs), superficial short-axon cells (sSACs), and external tufted cells (eTCs) (Shipley & Ennis, 1996). eTCs are the one excitatory juxtaglomerular cell type. They are typically uniglomerular (Imamura et al., 2020) and show fast, bursting responses just after inhalation, responding earlier than other principal OB cells to OSN input (Mori & Sakano, 2020). eTCs are thought to be a driver and synchronizer of glomerular activation through their feedforward excitation onto MCs mostly within the same glomerulus (de Jan et al., 2009; Gire et al., 2012; Hayar et al., 2004).

PGs are inhibitory and make up the majority of the juxtaglomerular population. They, like eTCs, are typically uniglomerular (Nagayama et al., 2014), and their dendrites tend to extend around a portion of the periphery of a glomerulus (Burton, 2017). PGs have multiple subclasses, some of which receive direct input from OSNs and others which do not (K. Kosaka et al., 1998). Collectively, PGs play an important role in inhibiting OSN input and MTC output activity, and moderating the activity of other PG cells (Nagayama et al., 2014; Parsa et al., 2015). One important hypothesized role of PGs is gating glomerular input by silencing glomeruli receiving only weak OSN input (Gire & Schoppa, 2009). With weak stimulation, PGs inhibit eTCs before they can drive further activation in MTC populations. This threshold filtering of OSN input increases sparsity in the spatiotemporal maps of glomeruli. Keeping representations sufficiently sparse reduces overlap in sensory representations and in turn facilitates differentiation and recognition of odors (Davison & Katz, 2007). Therefore, PGs play an important role in

intraglomerular processing and may help silence glomeruli that do not reach a sufficient activation threshold, which may aid odor coding in the OB (Gire & Schoppa, 2009).

The other inhibitory juxtaglomerular cells are sSACs. This cell class is less prevalent than PGs and make up only ~10% of the juxtaglomerular population (Nagayama et al., 2014). Unlike the other juxtaglomerular cell types, they are not uniglomerular. With dendrites extending across multiple glomeruli, they are hypothesized to play a role in interglomerular processing (Boyd et al., 2012; X. Liu & Liu, 2018), including the facilitation of lateral inhibition between glomeruli (Imai, 2014). They are also unique from the other juxtaglomerular cells in that they receive both direct OSN input and centrifugal feedback, moderating MTC activation from both a bottom-up and top-down manner (Imai, 2014).

Internal from the glomerular layer lie the somas of the output cells of glomeruli- MCs and TCs (TCs here refers to all tufted cell subclasses except eTCs). MCs and TCs have a similar dendritic feature where they extend one apical dendrite into a single glomerulus, making them uniglomerular in nature (Shipley & Ennis, 1996). They also have lateral dendrites which play a role in lateral inhibition within MC and TC populations (Nagayama et al., 2014). Aside from these shared dendritic features and their mutual function as output neurons, MCs and TCs have many differences. These include differences with regard to their position within the bulb, how they project to higher areas of olfactory cortex (Igarashi et al., 2012; Nagayama et al., 2010), and their activity profiles (Ackels et al., 2020; Burton & Urban, 2014; Eiting & Wachowiak, 2020; Kikuta et al., 2013). Due to the degree of these differences, they are hypothesized to form two streams of parallel output (Cavarretta et al., 2018; S. Jones et al., 2020; Nagayama et al., 2004).

Of these two output cell types, TCs are located more superficially in the OB and their somas are found in the EPL. Superficial tufted (sTCs), middle tufted (mTCs) and internal tufted (iTCs),

are the other main subclasses of tufted cell type aside from eTCs, and their somas are positioned from most to least superficially, respectively (Imamura et al., 2020). TCs receive direct OSN input via their apical dendrite and also interact with PGs and sSACs. TCs also extend lateral dendrites across the EPLs allowing them to interact with other TCs and MCs either directly or indirectly through dendro-dendritic interactions with inhibitory interneurons known as granule cells (GCs)(Burton, 2017). TCs contribute to recurrent processing and convey OB output to anterior regions of higher olfactory cortex, namely the anterior olfactory nucleus and anterior piriform cortex (Ennis et al., 2007; Eyre et al., 2008; Nagayama et al., 2014).

MCs are the other type of principal OB neuron and their tightly packed somas stretch across the bulb just beneath the EPL, forming the MCL. Unlike the relatively sparsely distributed and wide EPL layer, the MCL is only about the width of the average MC soma (Greer et al., 2008). Like TCs, MCs receive direct input from OSNs, but their activity is hypothesized to be driven to a greater degree by feedforward excitation from eTCs (Gire et al., 2012). MCs within a glomerulus, sister MCs, are known to be connected by gap junctions and show correlated activity patterns to OSN input as a result (T. Kosaka & Kosaka, 2004). Through their lateral dendrites, MCs exhibit both recurrent and lateral inhibition through their interaction with GCs (Margrie et al., 2000). Centrifugal feedback drives both inhibition and excitation in MCs though both direct feedback on MCs and indirect feedback via sSACs and GCs. Afferents from the anterior olfactory nucleus feedback directly on MCs (Matsutani, 2010) and have been shown to drive brief excitation followed by hyperpolarization (Markopoulos et al., 2012). Afferents from the piriform feedback to both the GL and the GCL, both inhibiting and enhancing MC activity to decorrelate population responses to learned odors, enhancing their separability (Otazu et al., 2015). MCs project axons upstream more sparsely but more broadly than TCs, projecting not just

the anterior portion, but across the olfactory cortex (Nagayama et al., 2010). Therefore, MCs communicate more directly across more of the olfactory cortex than TCs via both their output efferents and centrifugal afferents.

In addition to location and connectivity differences, MCs and TCs have markedly different activity profiles. TCs receive stronger OSN input currents (Nagayama et al., 2014), are more excitable (Burton & Urban, 2014), and have higher firing rates (Igarashi et al., 2012; Nagayama et al., 2014). They also tend to have broader tuning. With regards to odor identity tuning, they respond to a larger repertoire of odorant types than MCs (Chae et al., 2020). They also have broader intensity tuning, responding across a larger range of odor concentration due to their lower activation thresholds (Chae et al., 2020). The two principal neurons also respond on different timelines. Though there are discrepancies on the matter, many reports observe MCs responding after TCs (Burton & Urban, 2021; Cavarretta et al., 2018; Igarashi et al., 2012). Additionally, MCs have been observed to have sustained responses, continuing to fire even after the OSN input terminates (Imamura et al., 2020). Together, these findings may suggest that TCs operate on a faster or sharper temporal timeline than MCs, although a lack of studies comparing the responses of MCs and TCs to olfactory stimuli that vary over time make any such hypothesis difficult to access. Regardless, the activity profiles of MTC cell types are different in both the nature and timing of their response, and thus likely convey non-redundant information to their respective upstream targets.

In the deepest and largest layer of the OB are the granule cells (GCs). There are many subclasses of granule cells and they inhibit both MTs and TCs (Nagayama et al., 2014). GCs are the primary target of centrifugal feedback and play an important role in top-down regulation of OB activity (Matsutani, 2010). GC populations are thought to have a more complex role in

modulating bulbar activity than simply acting as gain control. Computational work suggests GC effects on bulbar activity are complex, leading to both increased synchrony and decorrelated odor representations in turn (Chen & Padmanabhan, 2020).

Together, juxtaglomerular cells, MTCs, and GCs form the shallow, but highly recurrent, network that characterizes activity in the OB. Exactly how this connectivity leads to sparse and specific spatiotemporal maps at the glomerular level is not yet fully understood, but glomeruli reliably encode odor identity and information about odor intensity to upstream olfactory cortex.

1.3 Odor concentration dependent responses in the first olfactory relay

Changes in stimulus intensity generally result in changes in the neural representation of the stimulus. The ability to generalize across these differences and recognize stimuli is important for sensory systems. In olfaction, rodents must identify odors across all levels of odor concentration, a measure closely related to odor intensity (Mainland et al., 2014). The spatiotemporal map of glomeruli responding to a given odor changes with odor concentration, and changes in glomerular maps have been shown to translate to changes in odor perception. As the spatiotemporal dynamics between two glomerular maps diverge, it becomes easier for a rodent to perceive the difference between the two odors (Bhattacharjee et al., 2019). Thus, an animal must be able to identify odors even when changes in concentration introduce variability to the glomerular maps that encode them. Despite this variability and the perceptual changes that it may entail, olfactory encoding is able to generalize odor identity across many levels of odor concentration (Belluscio & Katz, 2001). Due to this ability, olfactory processing is often referred to as concentration-invariant coding (Bolding & Franks, 2018; Wilson et al., 2017).

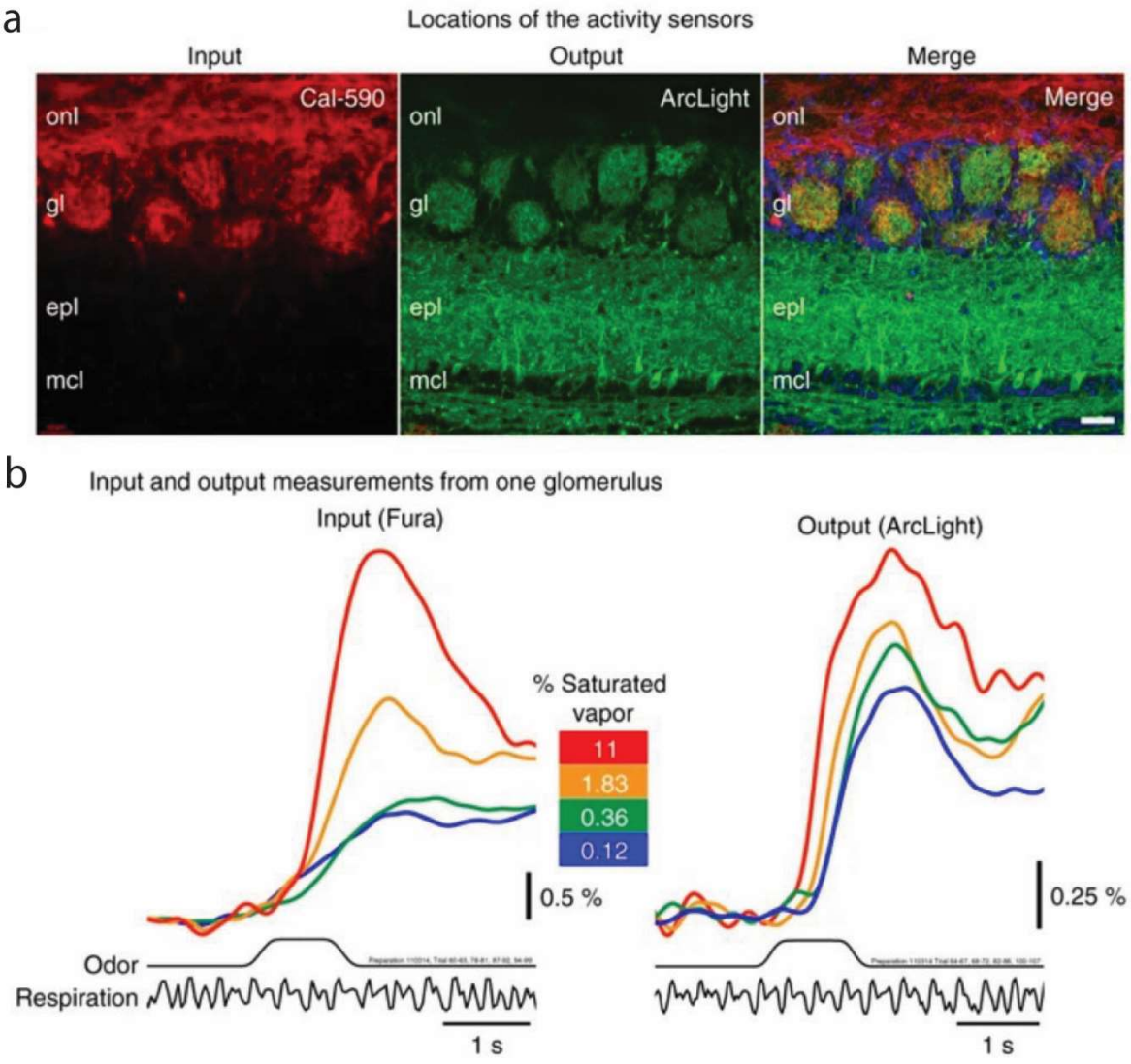

Figure 1.5: Simultaneous imaging glomerular input and output shows a reduction in response variability across concentration levels at the output level.

a) Histology depicting cell type specific targeting of input and output of the same glomerulus. (left) Olfactory receptor nerve input to the glomeruli was labeled with calcium sensitive dextran (Cal-590) dye, (middle) the output of glomeruli (MTCs) exhibiting cre-dependent expression of ArcLight, and (right) the merged image with DAPI showing overlapping of expression capturing input and output responses within the same glomeruli. **b)** The average input (left) and output (right) response from an example glomerulus responding to ethyl tiglate at different concentration levels (.12%-11% saturated vapor) shows that glomerular output is more similar across concentration levels than input. This suggests there is a transformation between glomerular input and output that makes responses to an odor more similar across concentration

levels. Example odor trace and respiration trace (sniffing signal) from one of the five trials are plotted below. This figure is Figure 1B-C of (Storace & Cohen, 2017) and reused following the guideline of its Creative Commons Attribution 4.0 International License.

The input to glomerular maps is formed by the ensemble of OSNs that activate at the epithelial surface in response to an odor. As mentioned, the OSN ensemble members and their respective activation levels are based on what odor features are present at the epithelial surface and the binding affinity of those features with their respective ORs. When an odor is present at a low concentration, OR's with the highest binding affinity to the odorant feature(s) bind first (Bolding & Franks, 2018). Therefore, when odorants are sparse, OSN ensembles are smaller as high affinity OSNs bind all the odorants before the low affinity OSNs are given sufficient interaction to bind. Conversely, when odorants are densely distributed along the epithelium, there is sufficient interactions across OSNs such that even low affinity ORs eventually bind. Thus, increases in odor concentration result in more opportunities for binding and larger OSN ensembles. In addition to larger ensembles, for OSNs that are responsive, concentration increases lead to increased firing rates (Tan et al., 2010; Zak et al., 2020). Thus, for the input to the first olfactory relay, concentration levels are positively correlated with both the size and strength of a responding OSN ensemble (Spors & Grinvald, 2002).

In response to OSN input, a subset of the glomeruli will reach a sufficient threshold to generate MTC output. Within a glomerulus, MTC output has characteristic differences from the input. In the transformation from input to output, one observed difference is that the bulb reduces the representation of concentration, by partially normalizing MTC output across concentration levels (Banerjee et al., 2015; Storace & Cohen, 2017, 2021). In imaging the input and output of glomeruli simultaneously, Storace and Cohen found that within a glomerulus, OSNs vary their response strength more when concentration changes resulting in a wider range of responses across odor concentration levels than MTC output. Although MTCs also increase their response strength with concentration, their response stays more similar across concentration levels. Thus,

at the first relay of olfaction, sensitivity to odor concentration changes is reduced such that glomerular output is more concentration-invariant than its input. Reducing the variability of glomerular output maps encoding an odor facilitates odor identification that is robust to concentration and intensity changes.

Despite this active role that OB takes in increasing concentration invariance, concentration changes still significantly alter the spatiotemporal dynamics of glomerular output ensembles. As mentioned above, higher concentration results in stronger MTC responses. Concentration increases also decrease response latencies. When more odorant molecules are present at the epithelial surface, there are more opportunities for binding interactions. In turn, higher concentrations elicit faster OSN responses and the average time needed to sufficiently excite a glomerulus decreases (Zak et al., 2020). Additionally, when the number of OR types activated increases at higher concentrations, it follows that the number of active glomeruli increases as well. These changes in recruitment of glomeruli are not subtle. Many single odorant molecules, when present in low enough concentrations, only sufficiently excite one to a few glomeruli (Burton et al., 2022), but odors can excite several to tens of glomeruli at higher concentrations. Therefore, increases in odor concentration result in strengthened responses, decreased response latency, and the recruitment of new glomeruli to the ensemble (Fukunaga et al., 2012; Spors & Grinvald, 2002; Wilson et al., 2017; Zhou & Belluscio, 2012). These changes lead to qualitative changes in the spatiotemporal activity maps of the OB.

The way in which concentration changes the responses of glomeruli within an ensemble is not homogeneous. Glomeruli do not all increase their responses to the same degree or at the same rate. First, glomeruli have different maximum response strengths with regard to their concentration tuning for a given odor (Fletcher et al., 2009). Additionally, maximum response

strength is not directly related to binding affinity as the glomeruli that are activated early are not necessarily those that respond the strongest. Some glomeruli that do not respond at low concentrations, reach a greater maximum response strength when activated at higher concentration levels. As a result, the most sensitive glomeruli may have strong contributions to the ensemble at low concentration levels, but may contribute relatively little at high concentrations when glomeruli with stronger maximum responses begin to activate (Fletcher et al., 2009). In addition to differences in activation strength, glomeruli do not have the same response tuning curves. Their responses can scale to different degrees and at different rates with respect to concentration (Fried et al., 2002). For example, a glomerulus that responds across only a narrow range of concentration and activates at low concentration levels, will saturate early and reach their maximum response strength at low concentration levels. Another glomerulus may respond over a much larger range in concentration, increasing its response slowly as concentration increases. Together, these differences in response strength and tuning lead to concentration-driven changes in the spatiotemporal activity maps responding to the same odor. Thus, not only does concentration change glomerular ensembles and scales their responses, but it does so differentially among ensemble members leading to qualitative changes in how each glomerulus represents an odor across concentration levels.

Despite odor concentration's notable influence on olfactory coding in the OB, odor identity is still encoded robustly across changes in odor concentration (Belluscio & Katz, 2001). There is one largely preserved aspect of spatiotemporal maps that does not vary with concentration-relative response latency. Although increases in odor concentration decrease the latency of responding glomeruli, they do so in a similar manner that preserves the order of responding glomeruli. Therefore, response latencies time drop by similar enough measures that

higher binding affinities will still bind faster than the glomeruli with lower binding affinities. This concept is known as latency coding (Margrie & Schaefer, 2003; Spors & Grinvald, 2002; Wilson et al., 2017), and is hypothesized to be one of the main methods of concentration invariant coding in the OB.

Despite its concentration invariant nature, the OB still encodes information about odor concentration levels via the changes to glomerular spatial maps. There is evidence though that in addition to odor concentration level, the bulb encodes information about odor concentration dynamics. Intracellular recordings of MTCs show that their subthreshold membrane potentials follow odor fluctuating in the 2-20 Hz range (Dasgupta et al., 2022). Additionally, mice can discriminate between odors fluctuating as fast as 40 Hz, showing they are capable of discerning fast changes in concentration dynamics (Ackels et al., 2021). The ability to perceive dynamics within these levels of temporal resolution is relevant for navigating natural odor environments, as a majority of dynamics in ethologically relevant plumes are thought to lie below this threshold (Justus et al., 2002; Mylne & Mason, 1991). In the same experiments, Dasgupta et al., 2022 found that a subset of MTCs change their spiking activity significantly when odors fluctuate at low (2 Hz) versus high (20 Hz) frequencies. This suggests MTCs responding to the same odor presented at the same concentration range moderate their spiking activity depending on the time course of odor concentration changes, or concentration dynamics. Furthermore, MTCs have also been observed to directly encode directional changes in odor concentration (Parabucki et al., 2019). MTCs show different responses to a given level of concentration when it differs from the previous sniff than they show to those same concentration levels presented in isolation. Therefore, despite the fact that glomerular processing seems to discard some information

regarding odor concentration, the OB still informs odor concentration levels and encodes concentration dynamics.

Rodents are hypothesized to perceive some spatiotemporal cues of plumes to aid their adept olfactory search behaviors. In addition to identifying and discriminating odors, the OB plays a role in encoding odor concentration and the dynamics with which concentration changes over time. To understand how rodents are capable of adept olfactory search, we must understand what types of spatiotemporal cues they may be capable of perceiving and how odor concentration dynamics present in natural plumes shape activity at the first relay of olfactory processing.

Chapter 2. Plume Dynamics Structure the Spatiotemporal Activity of Mitral/Tufted Cell Networks in the Mouse Olfactory Bulb (Lewis et al., 2021)

2.1 Abstract

Although mice locate resources using turbulent airborne odor plumes, the stochasticity and intermittency of fluctuating plumes create challenges for interpreting odor cues in natural environments. Population activity within the olfactory bulb (OB) is thought to process this complex spatial and temporal information, but how plume dynamics impact odor representation in this early stage of the mouse olfactory system is unknown. Limitations in odor detection technology have made it difficult to measure plume fluctuations while simultaneously recording from the mouse's brain. Thus, previous studies have measured OB activity following controlled odor pulses of varying profiles or frequencies, but this approach only captures a subset of features found within olfactory plumes. Adequately sampling this feature space is difficult given a lack of knowledge regarding which features the brain extracts during exposure to natural olfactory scenes. Here we measured OB responses to naturally fluctuating odor plumes using a miniature, adapted odor sensor combined with wide-field GCaMP6f signaling from the dendrites of mitral and tufted (MT) cells imaged in olfactory glomeruli of head-fixed mice. We precisely tracked plume dynamics and imaged glomerular responses to this fluctuating input, while varying flow conditions across a range of ethologically-relevant values. We found that a consistent portion of MT activity in glomeruli follows odor concentration dynamics, and the strongest responding glomeruli are the best at following fluctuations within odor plumes. Further, the reliability and average response magnitude of glomerular populations of MT cells are affected by the flow condition in which the animal samples the plume, with the fidelity of plume following by MT cells increasing in conditions of higher flow velocity where odor

dynamics result in intermittent whiffs of stronger concentration. Thus, the flow environment in which an animal encounters an odor has a large-scale impact on the temporal representation of an odor plume in the OB. Additionally, across flow conditions odor dynamics are a major driver of activity in many glomerular networks. Taken together, these data demonstrate that plume dynamics structure olfactory representations in the first stage of odor processing in the mouse olfactory system.

2.2 Introduction

Mice are adept at localizing odor sources (K. L. Baker et al., 2018; Gire et al., 2016; Gumaste et al., 2020; A. Liu et al., 2019), but the spatiotemporal information in olfactory environments that aids this search behavior is largely unknown. Odors travel in plumes which pull odor away from its source in filaments that are broken and distorted as they travel in air, creating complex odor environments. From the perspective of an olfactory searcher, these intermittent filaments create stochastic odor encounters, or whiffs, such that odor concentration dynamics fluctuate rapidly from moment to moment. Features of these complex plume dynamics contain information regarding odor source location (Celani et al., 2014; Murlis et al., 2000). For example, as a searcher encounters odors, the frequency, strength, and timing of encounters provide complex cues about an odor source (Ache et al., 2016; Atema, 1996; Michaelis et al., 2020; Vergassola et al., 2007).

A simple strategy, such as averaging odor concentration across whiffs could eliminate the complexity of an odor plume, allowing an animal to simply follow an increasing odor concentration gradient to the odor source. However, an animal dependent on this search strategy would operate at a timescale far slower than that observed in mice engaged in olfactory-guided search (Gumaste et al., 2020). This suggests that rodents most likely extract information from the

complex spatiotemporal dynamics of olfactory environments to support their efficient odor-guided search behavior.

The extraction of information from fluctuating odor plumes will necessarily be impacted by the physics of odor transport. Factors such as wind speed and the Reynolds number of the plume could impact early olfactory processing in mammals. Precise olfactometers have been used to model certain features found in natural odor environments, such as fluctuating and intermittent odor concentration dynamics. Although this work provides important insights, olfactometers do not capture the full complexity of the odor environment. One problem is a lack of knowledge regarding which features of the plume are relevant to olfactory search, constraining which features olfactometers have been used to mimic. In addition, olfactometers create artificial plumes that decouple odor concentration from features present in olfactory environments. This omits correlations between concentration fluctuations and the surrounding air flow as well as small scale details of odor transport like diffusion. Decoupling these factors creates challenges for interpretation because it implicitly disrupts processing moderated by these features, such as the impact of wind speed on the vibrissal system (Yu et al., 2016) or feedback regarding bilateral nasal sampling (Esquivelzeta Rabell et al., 2017; Markopoulos et al., 2012). Directly observing how MT activity is impacted by the plume dynamics of natural olfactory scenes will thus constrain hypotheses regarding which spatiotemporal features of natural odor stimuli are conveyed by the brain.

We studied the response of MT cells in the OB to odor concentration dynamics in awake mice as they processed natural olfactory scenes, i.e., odor plumes. We used wide-field calcium imaging to measure MT activity, allowing us to study MT activity contributing to OB output at the level of glomerular complexes on the dorsal surface of the OB. Simultaneous recordings of

the OB and plume dynamics show glomerular population activity follows fluctuations of odor concentration during plume encounters. The reliability and following behavior of glomerular responses were moderated by wind speed and the resulting changes in plume structure. The fidelity of odor concentration tracking increased when concentration dynamics were skewed, creating intermittent odor encounters across the plume presentation. In addition, as the strength and reliability of odor-evoked activity in MT cells increased, this activity more accurately followed plume dynamics. Together, these data demonstrate for the first time that the rapid fluctuations present in natural olfactory scenes significantly structure the activity of glomerular MT cell populations in the mouse OB.

2.3 Materials and Methods

2.3.1 Olfactory Stimuli

Olfactory stimuli were released by an automated odor port within a 40 × 40 × 80 cm acrylic wind tunnel where airspeed was controlled by a vacuum at the rear of the wind tunnel, posterior to the animal's location (Figure 2.1A). Concentration dynamics of olfactory stimuli varied stochastically from trial to trial creating plumes with unique concentration dynamics on each trial. Adjusting the velocity of wind flow allowed for variation in the Reynolds number, resulting in characteristic changes of plume dynamics for different flow levels (Appendix Supplementary Figure 1). Reynolds numbers were calculated using the mean flow of each condition and the half height of the tunnel (20 cm) as the head-fix setup is placed on a stage such that it is elevated ~20 cm from the tunnel floor (Figure 2.1B). Low, medium, and high flow Reynolds numbers were 2,400 ± 1,000, 8,800 ± 400, and 9,800 ± 200, respectively (mean ± st. dev), hence the medium and high flow conditions are fully turbulent, while the low flow is in the chaotic mixing regime. Across all flow conditions, plume presentations are stochastic and plume

dynamics do not correlate across time within trials (Appendix Supplementary Figure 2A) or across trials (Appendix Supplementary Figure 2B). Odor statistics confirm that high and medium conditions are fully turbulent (as seen from large skewness levels implying intermittency (Figures 2.1E–G) and spectra close to the expectation for turbulent flows, see Appendix Supplementary Figure 1D). The low flow condition is not yet fully turbulent [as seen from the low values of skewness and symmetric odor distribution (Figures 2.1E,G) and flatter spectrum (Appendix Supplementary Figure 1D)]. Absolute velocities of low, medium and high flow conditions were 0.40 ± 0.16, 1.31 ± 0.05, and 1.81 ± 0.17 fpm and velocity fluctuations were 14 ± 3, 6 ± 2, and 5.3 ± 1.5 fpm, respectively.

A single session consisted of forty trials of odor presentation. Odor ports were located upwind ~13 cm anterior to the animal's nose (Figure 2.1B), and each plume presentation had a duration of 10 s. Odor release began ~10 s into the trial. In order to avoid responses predicting the beginning of the plume, the exact time of odor release was randomized by adjusting the duration of the 5 s intertrial interval by a length of time (s) drawn randomly from a uniform distribution, U(−2, 2). Random clicking noise was used to control for the clicking sound of the port serving as a cue for plume onset. Starting 5 s prior to plume onset, a number was drawn from a uniform distribution, U(0, 1), for each camera frame, and if the number exceeded 0.95 a clicking sound was produced.

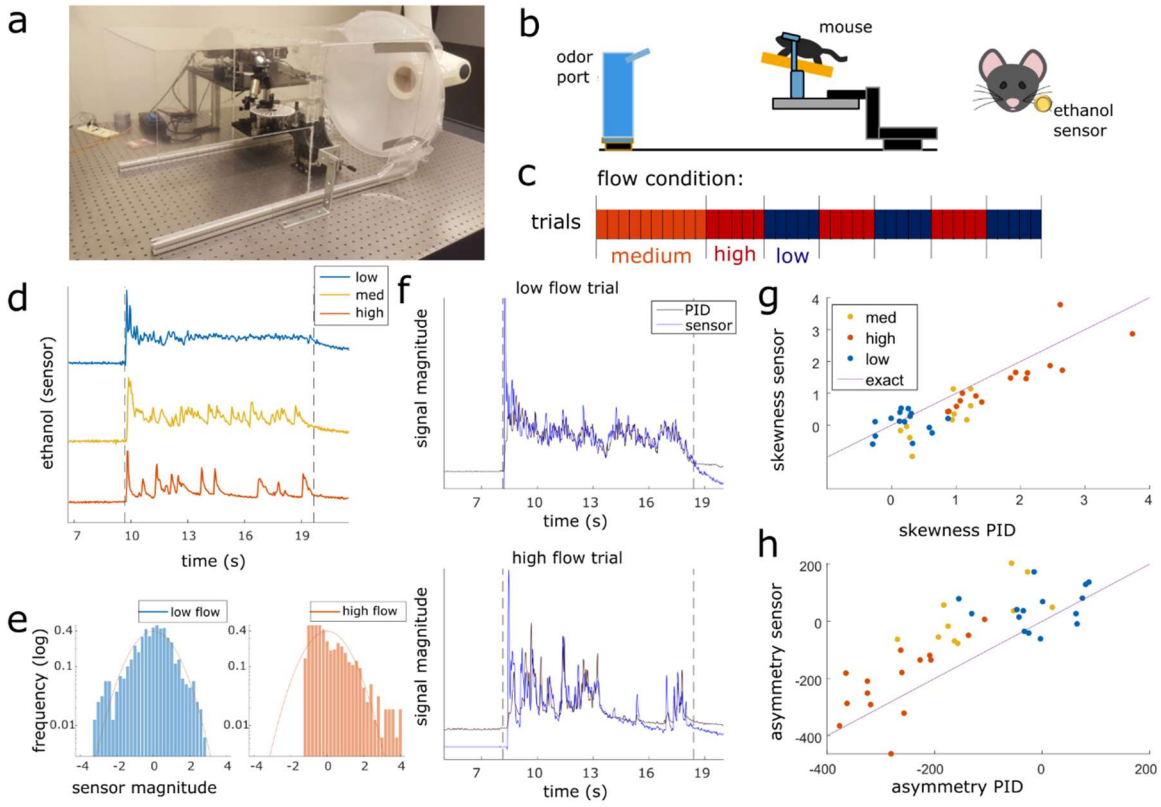

Figure 2.1: Plume presentations and head-fix setup for *in-vivo* recording experiments. **a)** All experiments conducted in a 40 × 40 × 80 cm wind tunnel for quick clearing of odor presentations. The odor port (not pictured) was located ~13 cms upwind of the animal's nose. **b)** (Left) Graphic detailing experimental setup. (Right) Ethanol odor concentration measured using a modified, commercially available ethanol sensor placed ~4 mm from the outer edge of the mouse's nostril. **c)** Diagram depicting flow conditions (high, medium, or low) of the 40 trials within a single session. **d)** Example odor traces are depicted for each flow condition. **e)** Histograms of the odor concentration magnitude sampled across two examples trials show a change in skewness between low flow (left, blue) and high flow (right, red), with skewness increasing with increased airflow during plume presentations. **f)** Comparisons between the deconvolved sensor signal and a PID signal during a set of paired recordings show odor concentration dynamics of the deconvolution can recover dynamics observed in the PID recordings ($r = 0.61$, $p < 0.001$). An example from low flow (top) and high flow (bottom) are shown. **(g-h)** Skewness **(g)** and asymmetry **(h)** of the deconvolved ethanol signal vs. the PID traces for each trial. All points lie close to the bisector (Purple line, labeled “exact”) showing that the deconvolution preserves measures of skewness and asymmetry consistent to the PID trace. High flow trials (orange) are separable from low flow trials (blue) and are substantially different from 0 (the expectation for any symmetric distribution, e.g., a Gaussian).

Ethanol concentration throughout each trial was measured by a modified, commercially available ethanol sensor placed within 3.5–4 mm from the mouse's right nostril (Figure 2.1B). For the experimental flow sessions, a benzaldehyde and ethanol odor solution (0.6% benzaldehyde, 85.7% 200 proof ethanol, and 13.7% distilled water) was used as the plume source for all trials. Odor solutions were stored in odor reservoirs (centrifuge tubes) with air-tight, customized tops. Tops had two openings connected to tubing. One tube was connected to a Clippard electric valve (part no. EV-2-12) to create airflow and the other was attached to a 3D printed odor port. For each plume presentation, the valve was opened to allow airflow into the tube such that odor vapors exited the odor reservoir and traveled through cylindrical tubing (1/16″ inner diameter) to the release point at the odor port. The odor port mounted the end of the tubing so that it was suspended at roughly nose height and located ~13 cm directly upwind of the animal's nose (Figure 2.1B).

One set of experiments consisted of an odor panel during which 3 odors were released across forty trials. For these sessions, wind speed was held constant and only odor changed. For all trials, plumes were presented at high flow. For the first ten trials, ethanol was presented (solution for plume source 86.3% 200 proof ethanol and 13.7% distilled water), for trials 11–25 a benzaldehyde-ethanol mixture was presented (solution same as flow experiments), and for trials 26–40 an isoamyl acetate- ethanol mixture was presented (solution for plume source consisted of 0.6% isoamyl acetate, 85.7% 200 proof ethanol, and 13.7% distilled water). Solutions were stored in three separate reservoirs, each with its own separate value and tubing. To change between odors during a session, the tubing running into the odor port was switched out manually during the appropriate intertrial intervals dividing odor conditions.

2.3.2 Implantation of Cranial Window

Implantation of the cranial window was adapted from methodology detailed in Batista-Brito et al. 2017 (Batista-Brito et al., 2017). Mice (n = 3 flow panel, n = 2 odor panel) were anesthetized with isoflurane for surgery. 2 × 2.5 or 2 × 3 mm craniotomies were performed above the olfactory bulbs and custom cut double windows were implanted. A customized stainless-steel head plate was glued directly on the skull posterior to the window, and two stainless steel screws (Neuroscience Invivo Research Components) were placed posterior to the head plate. Metabond was then added to cover all exposed skull and a thin layer built to cover the screws and the central surface of the head plate. The position of the craniotomy was biased toward either the left or right bulb.

2.3.3 In vivo Imaging

Widefield fluorescent microscopy was used for awake, head-fixed imaging in Thy1-GCaMP6f-GP 5.11 (IMSR Cat# JAX:024339, RRID:IMSR_JAX:024339) mice to view neural activity in the dorsal OB. Mice were between 11 weeks and 13 months old when imaged. 488 nm LED stimulation was used for the duration of the trial (~30 s), but was absent during intertrial intervals (~5 s) to avoid excessive bleaching. All mice were imaged at 30 Hz with 4 × 0.13 NA objective (Nikon). Neural activity was recorded using a Teledyne Photometrics Prime 95B sCMOS camera. For each session, mice were head-fixed above a freely rotating, circular track, allowing mice to run at will during imaging sessions.

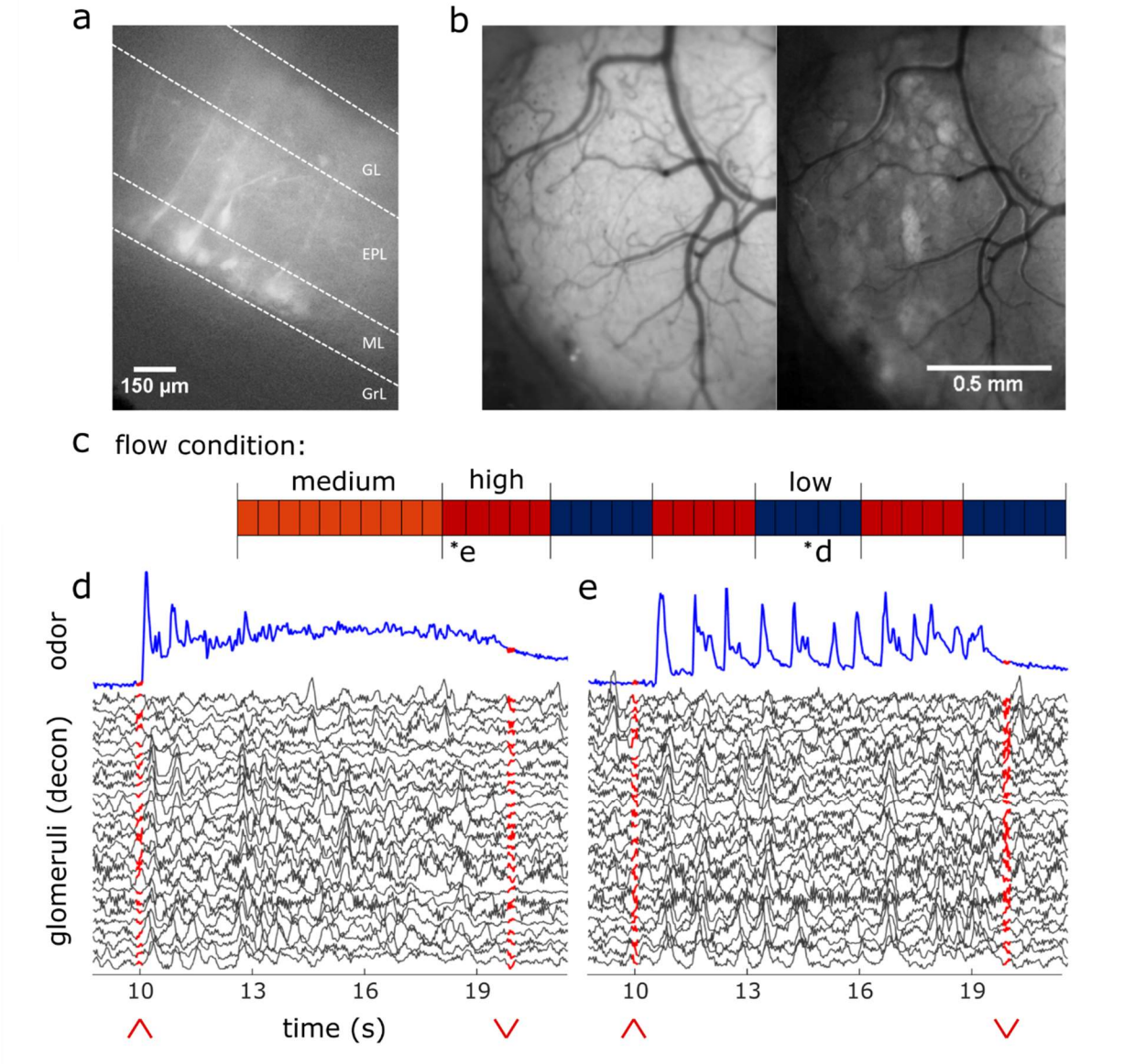

Figure 2.2: *In-vivo* recording of glomerular population response.
a) Change in fluorescence of MT cells in an acute *in vitro* OB slice preparation averaged over 3 s following a puff of high K+ solution. **b)** *In vivo* view of the dorsal olfactory bulb through an implanted cranial window. (Left) Window activity averaged across a single trial. (Right) Projected standard deviation for the same trial shows MT activity in the dorsal OB responsive to the odor presentation. **c)** Diagram depicting flow conditions (high, medium, or low) of the 40 trials within a single session. **d)** The deconvolved ethanol trace (blue) compared to the deconvolved response of each glomeruli (black) within the recorded FOV during a single low flow trial depicted by asterisk in **(c)**. Red arrows indicate onset and offset of plume presentation. **e)** Same as **(d)** but for a single high flow trial from the same session also depicted by asterisk in **(c)**.

2.3.4 *In vitro* OB Slice Imaging

To establish patterns of expression and signals obtained from the OB of Thy1-GCaMP6f- GP 5.11 animals, imaging experiments were conducted in OB slices. These animals show GCaMP6f expression in the main olfactory bulb as well as other areas of olfactory cortex, including but not limited to piriform and anterior olfactory cortex (Dana et al., 2014). Slice work verified strong expression in MT somas and dendrites (Figure 2.2A). Although we believe MT cells to drive the signal imaged in the OB, it is possible centrifugal feedback could contribute to some of the observed responses.

Horizontal OB slices (300–400 μm) were made following isoflurane anesthesia and decapitation. Olfactory bulbs were rapidly removed and placed in oxygenated (95% O2, 5% CO2) ice-cold solution containing the following (in mM): 83 NaCl, 2.5 KCl, 3.3 MgSO4, 1 NaH2PO4, 26.2 NaHCO3, 22 glucose, 72 sucrose, and 0.5 CaCl2. Olfactory bulbs were separated into hemispheres with a razor blade and attached to a stage using adhesive glue applied to the ventral surface of the tissue. Slices were cut using a vibrating microslicer (Leica VT1000S) and were incubated in a holding chamber for 30 min at 32°C. Subsequently, the slices were stored at room temperature.

Slices were placed on a Scientifica SliceScope Pro 6000, using near infrared imaging for slice placement and 488 nm LED illumination for imaging activity and a QI825 Scientific CCD Camera (Q Imaging) for image acquisition. Imaging was performed at 32–35°C. The base extracellular solution contained the following: 125 mM NaCl, 25 mM NaHCO3, 1.25 mM NaHPO4, 25 mM glucose, 3 mM KCl, 1 mM MgCl2, and 2 mM CaCl2 (pH 7.3 and adjusted to 295 mOsm), and was oxygenated (95% O2, 5% CO2). An elevated KCl solution (equimolar

replacement of 50 mM NaCl with KCl in the extracellular solution) locally applied through a borosilicate pipette using a picospritzer 2 (Parker Instrumentation) was used to stimulate cells.

2.3.5 Data Pre-processing

ImageJ was used to crop fields of view (FOVs) for data analysis. It was also used to extract pixel averaged signal for hand-drawn region of interest (ROI) analysis.

Matlab 2019b was used to analyze data and plot figures. Data was aligned using NoRMCorre software to perform piecewise rigid and non-rigid motion correction (Pnevmatikakis & Giovannucci, 2017). This alignment corrected for both global frame movement due to head jitter (rigid) and localized distortion due to brain movement (non-rigid).

2.3.6 Precise Tracking of Plume Dynamics

In the past it has been difficult to simultaneously record neural responses and plume dynamics without disrupting plume structure. Photoionization detectors (PIDs) are used to detect odorants, but PIDs sample via an active process, redirecting airflow into the sensor to detect odorants. In these experiments we used a miniaturized ethanol sensor modified from a commercially available metal oxide (MOX) sensor (Tariq et al., 2021). The sensor was placed within 4 mm of the lateral edge of the mouse's right nostril to capture the odor concentration signal across plume presentations for each trial. The sensor, a Figaro TGS 2620 Organic Solvent Vapor Sensor, was adapted similar to described in Tariq et al. 2021 by removing most of the metal head cap, including both a mesh covering and a solid metal covering. The resulting sensor was open to make direct contact with the airflow. In this adapted design, the sensor is mounted only to a circular base plate with a shortened metal cylindrical wall surrounding it. A single odor, a benzaldehyde-ethanol mixture, was used for each trial in the flow experiments. Odors released together travel together within plumes at sufficiently small scales because dispersion dominates

over diffusion (Celani et al., 2014; Yeung & Pope, 1992). In this way, the ethanol sensor measured the odor concentration of the benzaldehyde-ethanol mixture. The plume for each trial was released by an automated odor port at the upwind end of the wind tunnel, and the ethanol sensor measured the odor concentration of the ethanol across each trial. During plume presentations, the odor released from the odor port traveled in stochastic plumes through the wind tunnel. Therefore, plume onset time varied on each trial dependent on when the first filament made contact with the plume sensor. Reynold's numbers calculated within each flow condition (see Olfactory Stimuli above) show that plume dynamics are highly unsteady and dynamic, and fully turbulent at both medium and high flow. The odor was released 10 s after the trial began for a duration of 10 s. Each indicated flow condition was maintained throughout the entire trial. Flow condition was set for each trial block (Figure 2.1C) by adjusting the strength of a vacuum exhaust at the downwind side of the wind tunnel to one of three levels, low, medium, and high. Plumes were presented at medium level flow for the first 10 trials, after which flow alternated between high and low flow in blocks of five trials. Some sessions transitioned from medium to low flow initially and others transitioned from medium to high flow.

2.3.7 Ethanol Deconvolution

Recent characterization of MOX sensors comparing their deconvolved signals to simultaneously recorded PID (200B: mini photo-ionization detector) signals have validated the use of MOX sensors in capturing turbulent plume dynamics despite their slower recording dynamics (Martinez et al., 2019; Tariq et al., 2021). Tariq et al. show resolution of frequencies up to 15 Hz and high correlations between deconvolved MOX sensor and PID recordings at distances extending to >1 m in a turbulent airflow setting. For our experiments, ethanol concentration throughout each trial was measured by a modified, commercially available ethanol sensor placed

within 3.5–4 mm from the mouse's right nostril (Figure 2.1B). A single session consisted of 40 trials of odor presentation (plumes).

Sensor signal was acquired at 100 Hz and then low pass filtered at 30 Hz using a Kaiser window. The signal, e, was then normalized within each trial using the mean and standard deviation of the signal during the plume presentation. The signal was deconvolved by adapting the deconvolution specified in Tariq et al. (2021). The kernel was defined in the same manner, but instead of normalizing the range of the kernel, the integral of the kernel is normalized. Thus, the kernel, k, is calculated as follows:

$$k_0(t) = e^{\frac{-t}{\tau_{decay}}} - e^{\frac{-t}{\tau_{rise}}} \quad (2.1)$$

$$k(t) = \frac{k_0(t)}{\int_0^T k_0(s)ds} \quad (2.2)$$

where t is an array with evenly spaced timestamps at the proper sampling rate for the length of a single trial (T), τ_{decay}=0.4629, and τ_{rise}=0.0001. Both signals, e and k, are then transformed into Fourier space using the Matlab Fourier transform function, and the ethanol signal is deconvolved in Fourier space by dividing $\hat{e}$ by $\hat{k}$. The inverse Fourier transform of the resulting deconvolution is taken to obtain d such that $d = F^{-1}(\hat{e}/\hat{k})$. The deconvolved signal, d, is then normalized within each trial using the mean and standard deviation during the plume presentation, $d = \frac{(d - <d>)}{std(d)}$. The deconvolution optimizes the preservation of odor concentration dynamics across trials, but does not preserve the absolute value of odor concentration.

To optimize the parameters for the deconvolution, a complete session of 40 plume presentations was recorded with the usual ordering of flow condition blocks (Figure 2.1C). No

mice were recorded during this session. Instead, a PID was placed 4 mm from the ethanol sensor in the same position where the animal is usually head-fixed.

To optimize parameters, the PID signal, p, was first downsampled to 100 Hz to match the sensor sampling rate. Next, the signal was normalized within each trial using the mean and standard deviation of the signal during plume presentation, $p = \frac{(p - <p>)}{std(p)}$. This normalized signal was then Fourier transformed, convolved with the kernel and back-transformed to obtain the convolved signal $c = F^{-1}(\hat{p} \cdot \hat{k})$. It was then normalized and compared to the raw ethanol across a range of τ_{decay} and τ_{rise} parameter values. The Kernel parameters were chosen by minimizing mean squared error between the e and normalized c signals averaged across all trials within the paired recording session: $<\| \frac{e-(c-<c>)}{std(c)} \|^2>$. This optimized kernel is used to deconvolve the raw ethanol signal in the recording sessions. The deconvolved ethanol sensor signal allows for the recovery of plume dynamics unique to each trial (Appendix Supplementary Figure 2). It is significantly correlated with the PID signal as measured during plume presentations ($r = 0.61$, $p < 0.001$, both sampled at 100 Hz), which is a 0.22 improvement from the correlation between the raw ethanol sensor and PID signal ($r = 0.39$, $p < 0.001$, both sampled at 100 Hz).

Finally, with the exception of Appendix Supplementary Figure 1, the deconvolved trace was downsampled for figures and analyses to match the calcium trace (30 Hz) by averaging all samples taken across each camera frame. Deconvolution of the sensor signal during paired recordings is plotted and compared to both the raw sensor signal and to the PID reading from the paired recordings (Appendix Supplementary Figure 1). An initial inflection of signal at plume onset can be observed in the deconvolved ethanol signal for some trials (Figure 2.1D, Appendix Supplementary Figure 1B). This peak at plume onset is not reported by the raw sensor signal

(Appendix Supplementary Figure 1A) or by the PID signal (Appendix Supplementary Figure 1C) and is likely an artifact of the deconvolution. Since these experiments focus on how well MT activity follows odor concentration dynamics during plume encounters, the first and last seconds of the 10 s plume are omitted when analyzing neural responses to plume dynamics. The only exception is for the analysis of responsivity, which is based on the percentage of timepoints for which a significant response is observed and so this thresholded measure does not directly consider signal magnitude. Therefore, any artifact of plume onset dynamics in the sensor signal due to the deconvolution of its slower dynamics do not affect correlations reported between stimulus and response.

2.3.8 Defining Dynamic Flow

Dynamic flow was calculated within each session. In the experimental setup, flow condition is defined by wind speed. Intermittency was measured within a trial during the middle 8 s of the 10 s plume presentation by calculating asymmetry or by using the 3rd moment of the sampled distribution (the distribution odor concentration magnitude as measured for each time point across the window) (Figure 2.1E). Low and high flow trials were separable using either of these measures. As determined by these measures, intermittency increased with airflow moving from low to high flow conditions. The PID signal from the paired odor recording session shows this difference in dynamics as the concentration plotted across high flow trials exhibits increased intermittency as compared to that for low flow trials (Appendix Supplementary Figure 1C).

To see if there was a main effect of flow condition on these stimulus properties, skewness and asymmetry, a one-way analysis of variance (ANOVA) test was conducted for each parameter. For each ANOVA, multiple comparisons using a Tukey's test were performed to look for significant differences of the parameter between flow where comparisons were considered

significant for $p < 0.01$. These tests indicated that both skewness and asymmetry vary significantly across flow condition [$F_{(2,155)} = 52.7, p < 0.001$ and $F_{(2,155)} = 54.9, p < 0.001$, respectively]. Multiple comparison tests examining the differential effect of flow on these parameters showed that, for both, there was a significant difference between low and medium flow and a significant difference between low and high flow. No significant difference was found between medium and high flow. Therefore, only low and high flow conditions were selected when examining the effect of air flow on neural parameters.

2.3.9 Measuring Glomerular Responses to Plume Dynamics

Widefield imaging of the dorsal surface of the OB in Thy1-GCaMP6f-GP5.11 mice was used to capture MT cell activity at the glomerular level (Figure 2.2B). Thy1 mice exhibit fast kinetics and strong expression in MT cells within the OB (Dana et al., 2014). Global MT activity is clustered into dendritic complexes known as glomeruli. Widespread activity of secondary dendrites in the external plexiform layer (EPL) of the dorsal OB causes diffuse fluorescence across the imaging field. Therefore, CaImAn, a constrained non-negative matrix factorization (CNMF) algorithm, was used on each FOV to find regions of interest (ROIs) (FOV 1, FOV 2, and FOV 3 from mouse 1, $n = 27$, 17, and 6 glomeruli, respectively; FOV 4 from mouse 2, $n = 35$; FOV 5 from mouse 3, $n = 26$) and their activity traces (Pnevmatikakis et al., 2016). Thus, the spatial decomposition of CNMF provided the ROI for each glomerulus, and the temporal decomposition provided its corresponding denoised activity trace. The denoising of the CNMF temporal decomposition helps to remove correlated signals between neighboring glomeruli, accounts for calcium drift within recording sessions, and separates glomeruli overlapping in the dorsal-ventral dimension. The change in the distribution of correlation coefficients between ROIs before and after denoising (Appendix Supplementary Figure 3) shows a decorrelation of

glomerular signals. A two-sample Kolmogorov-Smirnoff test shows the distributions of correlation coefficients between the pixel averaged ROI traces, 0.87 ± 0.07 (mean ± std), and the CNMF ROI traces, 0.36 ± 0.28 (mean ± std), are significantly different ($D = 0.86$, $p < 0.001$).

To protect against over-segmenting a single glomerulus into multiple ROIs, neighboring ROIs whose baseline CNMF activity was correlated above 0.75 were selected as candidates for ROI merging (Appendix Supplementary Figure 4). The baseline period was examined as criteria for possible merging since glomeruli might have similar response profiles to the stimulus dynamics during plume presentations. The baseline activity of the neighboring ROIs was then binarized using a threshold of ± 1 std. If the correlation of the binarized activity between neighboring ROIs exceeded 0.75, the ROI with the lower mean activity (presumably encompassing less of the glomerulus) was dropped from the analysis.

To validate the use of CNMF for ROI selection, results were compared to a hand-drawn ROI analysis conducted on one of the fields of view (FOV 5) in ImageJ (Appendix Supplementary Figure 5). Using this standard, manual ROI selection, we show CNMF decomposition and denoising does not qualitatively change the interpretation of the data. Rather, CNMF recovers spatial and temporal resolution of MT activity by increasing the number of ROIs detected per field and decreasing pairwise correlation between ROIs. This decrease in pairwise correlation between ROIs suggests CNMF reduces common global signal, such as that from neuropil activity where secondary dendrites and global centrifugal feedback in the OB produce diffuse excitation across the dorsal surface of the OB. Hand-drawn ROIs were selected after viewing footage and reviewing standard deviation and maximum value projections of activity from the FOV within each trial. The activity averaged from within hand-drawn ROIs has higher pairwise correlations than denoised CNMF activity traces. This mirrors what is seen when pixel-averaged

activity from within CNMF ROIs (without denoising) is compared to the denoised traces. Thus, the denoising of CNMF recovers the spatiotemporal resolution of glomerular activity observed in the dorsal OB recordings in both types of analyses. A two-sample Kolmogorov-Smirnoff test shows the distributions of correlation coefficients between the deconvolved hand-drawn ROIs, 0.81 ± 0.08 (mean ± std), and the deconvolved CNMF traces, 0.1935 ± 0.3471 (mean ± std), are significantly different ($D = 0.86$, $p < 0.001$). Results of the hand-drawn ROI analysis (power and correlation analyses, Appendix Supplementary Figures 5D,E, respectively) were qualitatively similar to those found using CNMF corroborating the ability of glomerular networks to resolve odor concentration dynamics. Cross-correlations show a relation between glomerular and ethanol signals during odor presentation with all glomeruli having significant correlation with the plume during odor presentation as compared to their respective null distributions from trial shuffled correlation analyses. In addition, a strong correlation between glomerular response power (0–5 Hz) and ability to track odor concentration dynamics is also present in the hand-drawn ROIs ($r = 0.80$, $p = < 0.001$). Thus, we find that CNMF captures the relationship between glomeruli and plume dynamics while improving the resolution of glomerular network activity and inter-glomerular temporal dynamics.

The CNMF activity traces from the identified glomeruli were baseline normalized using the mean and standard deviation of a 5 s baseline activity period prior to stimulus onset. Traces for each glomerulus were then deconvolved in the style of Stern et al., (Stern et al., 2020) to recover the average activity rate of each glomerulus. To find the optimal penalty parameter, λ, for deconvolution, λ was optimized within each glomerulus. Then the median of this optimized distribution was used as the λ in the deconvolution for all glomeruli. After deconvolution, traces were standardized using the standard deviation of the glomerulus's entire trace. Deconvolved

signals were standardized in this way since the florescence range of a glomerulus's response depends on the number of expressing MT cells, the depth of the glomerulus from the dorsal surface, and other methodological factors unrelated to the magnitude of the response.

2.3.10 Testing for Responsive Glomeruli

A glomerulus was considered to be responsive to odor if its deconvolved trace exceeded threshold more time points than expected by chance during plume presentations as compared to its activity level during odorless baseline periods (Figure 2.6). Since this preliminary measure does not rely on stimulus dynamics, it captures glomeruli that respond to the plume even if their response is unrelated to odor concentration dynamics or only present for part of the plume.

First, the deconvolved trace of a single glomerulus was split into two periods: baseline activity and odor response. The baseline period is a 5 s period at the beginning of each trial prior to plume onset. The odor response period is the time during which the plume is present as well as 1 s immediately following the plume since inhibition has been shown to induce excitatory rebound responses in tufted cells (Cavarretta et al., 2018). The signal is first baseline normalized by subtracting the mean and dividing by the st. dev of the baseline activity within each trial. Next, it is binarized, thresholding for time points where activity exceeded the 95% confidence interval of the glomerulus's original baseline activity (thresholded at ± 1.96 baseline mean). In this way, each time point that crossed the threshold was considered an event. Within each trial's plume presentation, if the number of events exceeded the null expectation (5% of the total number of time points during plume presentation rounded up to the nearest integer), the glomerulus was considered to be responsive to the plume during that trial. The proportion of trials to which the glomerulus responded was calculated within three sets of flow conditions (all flows, low flow, and high flow). To illustrate responsivity scores within and between glomeruli

simultaneously, scores are plotted as a stacked bar graph (Figure 2.6A, cumulative scores are not used for analytic purposes).

2.3.11 Cross-Correlation Between Plume Dynamics and Corresponding Neural Responses

To understand the relation between stimulus and response time series, a preliminary analysis was conducted by calculating the correlation coefficients between the two signals for each glomerulus. In the future, more sophisticated techniques will be used to establish how much of the neural representations can be explained by high-fidelity odor concentration encoding.

Due to the stochastic nature of plume onset and offset times, the correlation is only calculated for the middle 8 s of the 10 s plume so that onset and offset dynamics are not included and the correlation measure represents the magnitude of plume tracking during plume encounters. The cross-correlation coefficient of a glomerulus r_g is calculated between the ethanol e and calcium c deconvolutions during plume presentations. For a single glomerulus, the correlation coefficient between the two deconvolutions within a single trial n is calculated at all possible lags l. Using the xcorr() function in Matlab to compute the coefficients, both signals are mean subtracted prior to calculating the cross-correlations such that the correlation coefficients are synonymous with calculating the Pearson correlation coefficient between the two signals at each respective lag value.

$$r_{g,n,l} = corr(e_{n,l}, c_{n,l})$$

The mean coefficient for each glomerulus, $\underline{r}_{g,l}$ is calculated by averaging across all trials within the session (n = 40 for 3 FOVs, and n = 39 for 2 FOVs) at each possible lag. The maximum coefficient mean is selected from all lags within a 500 ms window w of the neural activity following the ethanol signal.

$$r_g = \underline{r}_{g,l}$$

This is considered to be a window of sufficient size to account for variable delays in glomerular processing. The average time lag of r_g was 130 ms ± 100 (mean ± st. dev).

Within flow cross-correlations are calculated in the same manner but averaged only across trials within the specified flow condition.

For plotting of tracking ability (Figures 2.5A,B), r_g is compared to a single trial shuffled analysis using the same method as detailed above. The difference between the matched and shuffled coefficients suggest correlations are not solely a result of plume structure, but are driven by the temporal dynamics unique to each trial. Trials were shuffled within each glomerulus by calculating the correlations between $e_{n,l}$ and $c \neq_n$. In this way, any relation dependent on the dynamics of the stochastic fluctuations within each plume presentation is lost, but other statistical features of the plume presentation are preserved, yielding a baseline value for the cross-correlation. Glomeruli are plotted in Figures 2.5A,B if their correlation coefficient from the matched analysis exceeds ± 2 standard deviations (st. dev of the coefficient distribution from the shuffled analysis) of the shuffled mean coefficient. Since correlation varies significantly within a glomerulus across flow conditions, a glomerulus is considered to exceed the shuffled mean if it does so in at least one of the three defined conditions, all flows, low flow, or high flow.

Using the same shuffled correlation, a bootstrap analysis was conducted (10,000 iterations) creating a null distribution of the shuffled mean correlation coefficients to test for significance (Supplementary Figure 2.7C). The mean correlations are compared to their respective 95% confidence interval for the null distribution. Glomeruli are considered to respond significantly to plume dynamics when their mean coefficients exceed their null expectation. Non-significantly responding glomeruli are depicted in stacked bar graphs using gray hues

(Figures 2.5C, 2.6A).

Comparison of correlation coefficients in the matched vs. shuffled cross-correlations does not naturally divide the glomeruli into two subpopulations, but rather the strength of this relationship varies continuously across glomeruli. Therefore, instead of dividing glomeruli into subpopulations of tracking vs. non-tracking, our analyses consider how the strength of odor concentration tracking compares to other properties of the glomerulus and its response.

2.4 Results

2.4.1 Measuring Glomerular Response to Plume Dynamics

Using a modified, commercially available odor sensor combined with widefield calcium imaging techniques in head-fixed mice, we reliably tracked plume dynamics and investigated glomerular responses to this fluctuating input. Imaging was conducted in Thy1-GCaMP6f-GP5.11 mice which have fast kinetics and expression in mitral and tufted (MT) cells within the olfactory bulb (OB) (Dana et al., 2014) (Figure 2.2A). Widefield imaging of the dorsal surface of the OB allows for glomerular level resolution of the neural response (Figure 2.2B) (Fletcher et al., 2009). To explore a range of plume dynamics an animal may encounter in its natural environment, we changed the airspeed in the wind tunnel to create stochastic plumes with different odor concentration dynamics (Figures 2.1D–H). Odor identity, concentration and volume released from the odor port remained constant across all flow conditions, making the plume dynamics the only source of variation (Figures 2.2C–E).

2.4.2 Mitral and Tufted Population Activity Correlates with Plume Dynamics

At the bulbar level, imaging of MT cell activity shows activation of glomerular networks during odor exposure (Figure 2.3A). The global MT activity for a given field of view (FOV) was subjected to principal component analysis (PCA) and compared to the simultaneously recorded

plume dynamics (Figure 2.3B). The FOV's were aligned prior to PCA, but no segmentation or denoising was performed. To search for component activity responsive to plume dynamics, the correlation between each principal component and the odor concentration dynamics was calculated. There exists a high ranking component for each mouse that correlates strongly with plume dynamics (Figures 2.3C,D). Plotting the loading weights of the maximally correlated component shows dense clusters of high variance resembling partial spatial maps of glomerular activity. These findings demonstrate that MT population activity recorded in the first relay of olfactory processing is correlated to odor concentration dynamics during plume presentations. In order to establish whether individual glomeruli are correlated to odor cues, we sought to segment the MT activity into glomerular units to determine their respective contributions to the observed tracking of plume fluctuations by population activity.

2.4.3 Neural Activity of Glomeruli

CNMF decomposition provided locations of glomeruli and their corresponding denoised traces (Figure 2.4). To recover the average activity of synaptic complexes of MT activity known as glomeruli, CNMF traces were deconvolved in the style of Stern et al. (2020) (see methods). The mean deconvolved trace across trials was calculated for each glomerulus during plume presentations (Figure 2.4E). The mean response of a deconvolved trace (Figure 2.4F) was only considered during the middle 8 s of the 10 s odor plume to concentrate on glomerular responses to odor concentration dynamics during plume presentations and avoid responses to onset or offset plume dynamics.

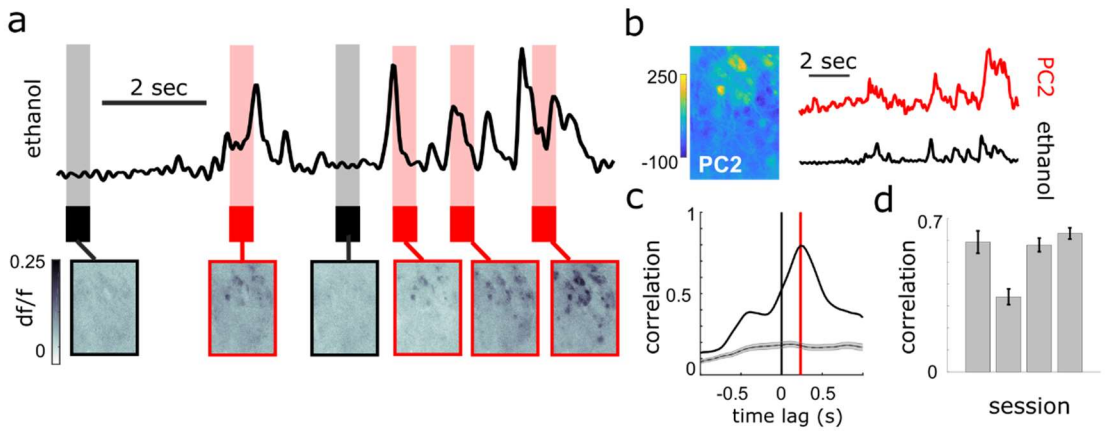

Figure 2.3: Population response of MT cells in dorsal OB respond to changes in odor concentration during plume presentations.

a) Simultaneously recorded deconvolved ethanol plume (top) and imaging of calcium signals from MT cell activity in an example FOV of a Thy1-GCaMP6f (GP5.11) mouse (bottom). Baseline and odorless periods (black) and odor plume input (red) are shown from the indicated time points. Fluctuations in the odor plume elicit repeatable activation of specific glomerular networks in response to whiffs of odor during plume presentations. **b)** (Left) An image of the principal component loadings corresponding to the odor-evoked activity [principal component 2 (PC2)]. (Right) Time series of PC2 (top, red) aligned to the simultaneous ethanol signal (bottom, black). Scale bar indicates 2 s. **c)** Cross-correlogram between the two signals in **(b)**. Red line indicates a slight offset from 0 for the peak correlation (~250 ms mean lag across FOVs from sensor to OB response). Gray plots average the null correlation ± SEM (correlation of neural activity from the example trial with odor signal from all non-matched trials in session). **d)** Cross-correlations (mean ± SEM) between odor evoked population activity (principal component) and ethanol sensor signal are strong across 3 Thy1-GCaMP6f (GP5.11) mice ($r = 0.54 \pm 0.07$).

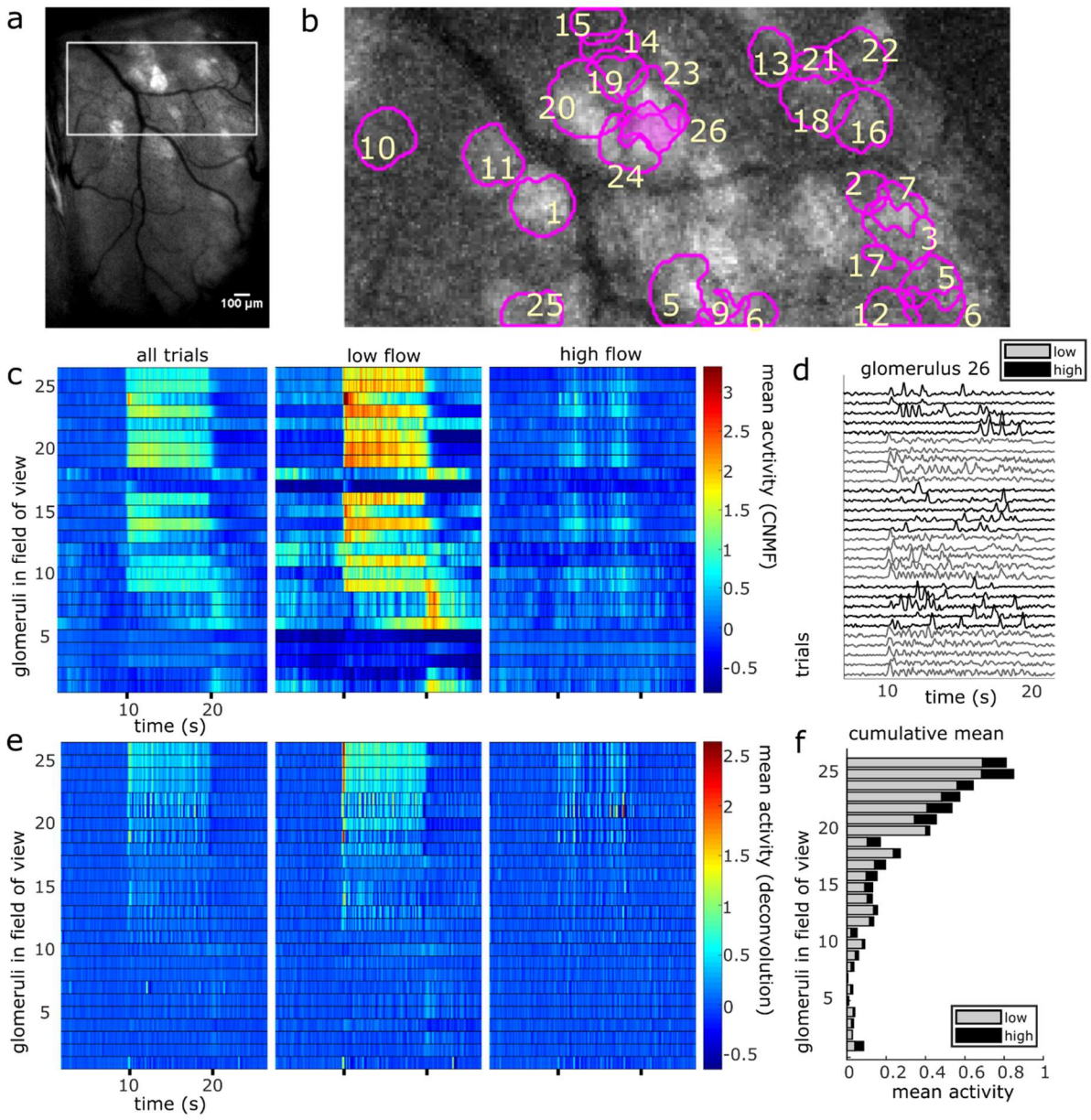

Figure 2.4: The spatial and temporal decomposition of CNMF identifies glomeruli and denoises their traces.

a) The white box outlines the FOV used for analysis as it relates to the larger recording window. The image shows the standard deviation projection of the aligned recording during a single odor presentation. **b)** Mean subtracted maximum projection of the same trial overlaid with ROIs from CNMF spatial decomposition shows segmentation of glomeruli for a single FOV using CNMF spatial decomposition. The spatial decomposition of the FOV results in 26 glomeruli (four dropped units after merge analysis not pictured) as outlined and numbered. **c)** Shows the mean traces of each glomerulus's CNMF temporal decomposition within each flow condition (left to right : all trials, low flow, high flow). Trials sorted by magnitude of normalized mean deconvolved response (**e)** during odor exposure. **d)** The deconvolved CNMF response of a single

glomerulus [pink fill **(b)**] to all low (gray) and high (black) flow trials across the recording session shows glomerular responses vary due to the unique odor concentration dynamics of each plume. **e)** Deconvolution accelerates dynamics of glomerular responses as shown by the mean deconvolved traces of the corresponding glomeruli depicted in **(c)**. **f)** The cumulative mean, a sum of the mean responses for each glomerulus in low and high flow, are plotted as a stacked bar graph so that comparisons between mean responses can be made within and across glomeruli simultaneously. Mean responses are calculated for the deconvolution **(e)** within each flow condition during the plume release and vary significantly between conditions [$t(110) = 11.43$, $p < 0.001$] with higher average responses in low flow.

For each glomerulus, the mean response across plumes was also calculated within low and high flow conditions. A paired samples t-test found that glomerular response means varied significantly across low and high flow conditions [$t_{(110)} = 9.71, p < 0.001$]. Mean responses were higher in low flow conditions, during which lower airspeed resulted in plume dynamics that were less intermittent, as shown by lower skewness and asymmetry in the deconvolved odor signals of low flow trials as compared to high flow trials [$F_{(2,155)} = 52.7, p < 0.001$ and $F_{(2,155)} = 54.9, p < 0.001$, respectively] (Figures 2.1E–H). In high flow conditions, increased intermittency produced more brief, high concentration fluctuations followed by blanks, or periods without odor signal. This decreased response observed across high flow conditions could be due to a decrease in odor concentration means as plumes had lower concentration means in high flow. PID recordings from the paired recording experiment show a significant 50% decrease of the mean concentration in high flow as compared to low flow ($z = 6.65$, $p < 0.001$). Thus, the mean MT activity increased in low flow trials following the increase in stimulus mean, but activity became less correlated with plume dynamics, suggesting the response of glomerular populations are moderated by plume dynamics.

2.4.4 Correlation Between Stimulus and Glomerular Activity

To determine if plume dynamics could be moderating the glomerular population response, cross-correlation was used to quantify the relation between odor concentration dynamics and simultaneously recorded glomerular activity (Figure 2.5). Most glomeruli significantly followed plume dynamics when correlation between neural activity and odor activity was calculated across all trials (100/111), across low flow (97/111) trials, or across high flow (100/111) trials. Significant tracking of the stochastic changes in odor concentration across plume presentations is determined by comparing mean correlation coefficients to a null

distribution created using a trial shuffled bootstrap analysis (see methods) (Supplementary Figure 2.7C). Within glomeruli that significantly responded to plume dynamics, the degree of tracking (the strength of the correlation between plume dynamics and a glomerulus's response) varied along a continuum such that some glomeruli were more responsive to fluctuations in odor concentration than others (Figures 2.5C,D). Higher correlation coefficients are not observed when glomerular responses are trial shuffled and ethanol recordings are no longer compared to the glomerular responses they elicited (Figures 2.5A,B, Appendix Supplementary Figure 7C). This shows that it is not the statistics of stimulus presentations that drive this correlation, but rather the plume's temporal dynamics unique to each trial.

Correlation coefficients (tracking) increased from the null expectations by 0.13 ± 0.08 (mean ± std) across all flow conditions, 0.08 ± 0.07 within low flow, and 0.16 ± 0.11 within high flow. Glomeruli were significantly better at tracking plume dynamics in high flow than they were in low [$t_{(110)} = 12.81, p < 0.001$] (Figure 2.5C) with average correlation coefficients increasing by 0.11 ± 0.09 (mean ± std). We wondered if this increase in correlation could result from increased sparsity. Indeed, correlation between two signals where the values are constant or zero for most of the time is automatically high, even if the peaks are entirely uncorrelated. If this was the case, the shuffled correlations in high flow should be significantly higher than in low flow, but this is not observed when looking at the confidence intervals for the null correlation coefficients computed within flow conditions (Appendix Supplementary Figure 7C). Thus, a large fraction of the glomerular population follows fluctuations during plume encounters, and the degree of dynamic tracking is moderated by plume dynamics, becoming stronger on average during plumes with higher levels of intermittency (as measured by increased skewness in high flow trials).

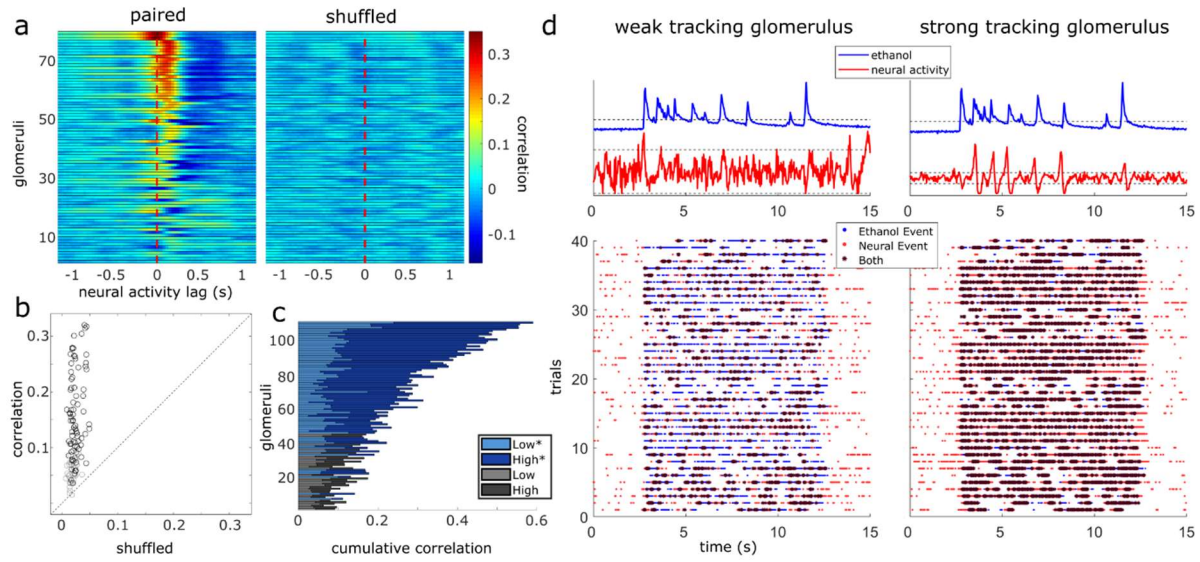

Figure 2.5: Glomerular population activity follows odor concentration dynamics across plume encounters.

a) (Left) The cross-correlation between the deconvolved ethanol trace and each glomerulus's deconvolved activity trace is calculated within each trial and then averaged across trials. Each row is a glomeruli and each time point represents the cross-correlation at the indicated lag. Glomeruli are sorted in order of decreasing magnitude of correlation coefficient (see methods). (Right) Same as left but glomerular responses are trial shuffled so that the signals compared are not from the same trial. Glomeruli are sorted to match their corresponding unshuffled cross-correlation in the right panel. **b)** Scatterplot of the correlation coefficient of all glomeruli if compared to their respective shuffled coefficient. Glomeruli plotted in (A) are marked in black if their coefficient exceeds their shuffled coefficient from a single trial shuffled comparison by 2 standard deviations. **c)** The cumulative correlation, a sum of correlation coefficients for each glomerulus in low and high flow, are plotted as a stacked bar graph so that comparisons between mean responses can be made within and across glomeruli simultaneously. The cumulative plotting shows variation in ability to detect changes in odor concentration dynamics across glomeruli both within and across flow conditions. On average, a glomerulus's tracking ability varies significantly between conditions [$t_{(110)} = 12.81, p < 0.001$], with most glomeruli having stronger correlation coefficients in high flow trials. Glomeruli that significantly correlate with plume dynamics in at least one condition are plotted in blues (*) while those that do not are plotted in grays. **d)** Binary cross-correlation. Top: Simultaneously recorded signals shown for two example glomeruli responding to the same example trial's odor plume. Odor and glomerular activity traces plotted with their respective thresholds (dotted, odor threshold: mean during plume presentation, neural threshold: ± 2 st. dev of baseline). Bottom: Resulting binarized traces plotted for each trial illustrate the magnitude of concurrent activity as events (stars) between the plume and the response of each glomerulus across the experimental session.

A second set of experiments, an odor panel, was used to assess whether the tracking behavior seen in the flow experiments is generalizable beyond the benzaldehyde mixture used. We recorded MT activity as it responded to plumes of three different odors within a single session. Plumes consisted of either ethanol (without a mixed odorant), benzaldehyde, or isoamyl acetate. For all trials, flow stayed constant and was set to the high flow condition. Results corroborated the ability of MT activity to respond to odor concentration dynamics and show tracking behavior generalizes beyond the benzaldehyde mixture used in the flow experiments. Glomeruli that significantly responded to odor concentration dynamics were found in the ethanol only condition (41/59 glomeruli), the benzaldehyde/ethanol condition (38/59), and the isoamyl acetate/ethanol condition (41/59) (Appendix Supplementary Figure 8A), and the majority of glomeruli reached significance in at least one odor condition (54/59).

2.4.5 Plume Fluctuations Structure Glomerular Network Dynamics

We measured glomerular responsivity and response power to see the effect of flow condition on these measures and whether these measures were related to how well a glomerulus followed plume dynamics.

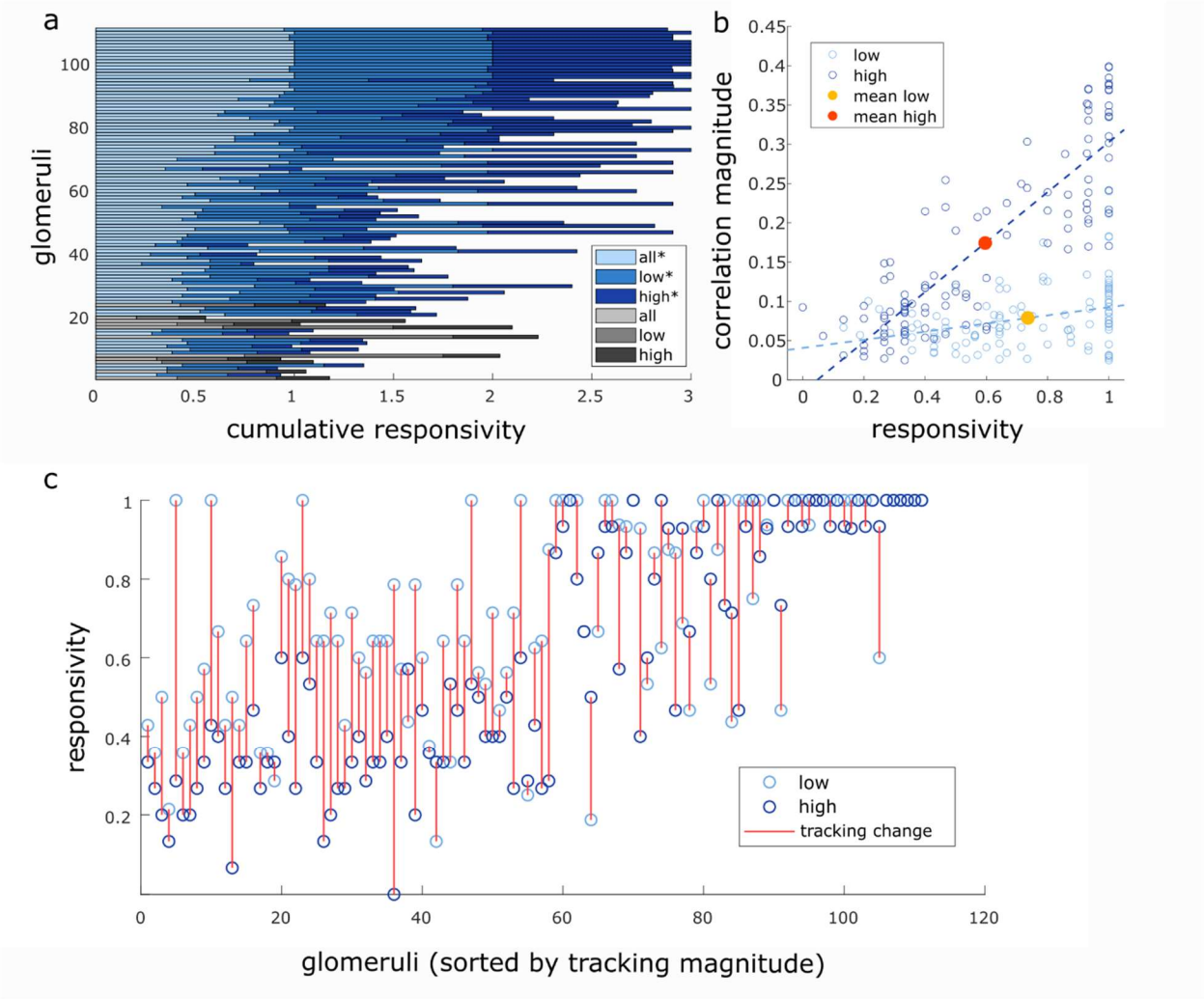

Figure 2.6: Glomeruli that respond more reliably to plumes are more correlated with their dynamics.

a) Responsivity scores plotted as a cumulative bar graph to illustrate differences within and across glomeruli when responsivity is calculated across all conditions (lightest blue) or is calculated exclusively within low flow (medium blue) or high flow (dark blue). Glomeruli are sorted top to bottom by decreasing average tracking ability (correlation magnitude) and glomeruli that significantly track plume dynamics (as defined in methods) are plotted in blue hues(*) while those that do not are plotted in gray hues. The graph shows magnitude of odor concentration tracking is correlated with ($r = 0.76$, $p < 0.001$), but is not strictly defined by response reliability as glomeruli exist that respond strongly to odor presence but not to concentration dynamics. In addition, within flow comparisons show responsivity is significantly higher in low flow than high flow [$t_{(110)} = 12.13$, $p < 0.001$]. **b)** Within flow condition, responsivity is plotted against tracking ability (correlation magnitude) for each glomerulus (circle). To represent the population response, the average responsivity across all glomeruli (low average = yellow dot, high average = red dot) is plotted against average correlation with plume dynamics within low (light blue) and high (dark blue) flow conditions illustrating how flow

moderates these relationships. Across glomeruli, responsivity is positively correlated with tracking ability as is illustrated by the lines of best fit. On average, higher flow predicts a decrease in average responsivity level but also predicts an increase in tracking ability. **c)** Average responsivity in low and high flow is plotted for each glomerulus, and the change in mean responsivity between flows shown in **(a)** is explicitly plotted for each glomerulus (red line) as well. Glomeruli are sorted by increasing tracking ability (from left to right) showing glomeruli with higher response reliability are more sensitive to plume dynamics.

We found that there was a significant effect of flow condition on glomerular responsivity. Responsivity is defined as the proportion of trials to which a glomerulus responded to the odor (see methods). Glomeruli had significantly higher responsivity during low flow trials ($t = 12.1$, $p < 0.001$), with responsivity scores increasing by 0.21 ± 0.18 (mean ± st.d) as compared to high flow (Figure 2.6). Therefore, glomeruli responded to low flow trials more reliably than they responded to high flow trials. As noted previously, the average correlation between plume dynamics and MT activity increased in high flow conditions, so although glomerular responses became less reliable as airflow increased, they became more correlated with plume dynamics (Figure 2.6B).

Responsivity is a thresholded measure that determines if a glomerulus is more active than expected by chance during a plume presentation and does not capture the dynamics present in the response. The strength of the dynamic activity of glomeruli was determined by measuring the change in cumulative response power between baseline periods and plume presentations (see methods) (Appendix Supplementary Figure 6). Fast Fourier transform was used to measure response power within 0–5 Hz, a frequency range relative to the stimulus dynamics (Figure 2.7). Response power (0–5 Hz) increased significantly from baseline during plume presentations [$t_{(110)} = 20, p < 0.001$] by 5.7 ± 3.0 a.u. (mean ± std), a 448% increase (Figure 2.7). On average 86.7 ± 4.9% (mean ± std) of cumulative stimulus power for each session was within 0–5 Hz. Stimulus power was measured using the deconvolved odor signal of the plumes to which MT cell responses were recorded (experimental flow sessions only). The majority of cumulative response power for each glomerulus, 88.5 ± 7.9% (mean ± std), was also found to be within this range. Thus, the majority of response power for each glomerulus was measured to be within a relative frequency range of the stimulus (Figures 2.7A,B). Across all glomeruli recorded,

response power was not significantly different between flow conditions. To examine the effect of flow conditions on the response power of cells that most strongly responded to the odor, we next analyzed only glomeruli whose mean response was above the 75th percentile. Within this group of glomeruli, response power did change significantly between flow [$t_{(27)} = 5.52, p < 0.001$], with stronger response power during high flow conditions (Figures 2.7D,E). This increase reflects the significant increase in stimulus power (0–5 Hz) observed in high flow as compared to low flow trials [$t_{(116)} = 31, p < 0.001$] (Figure 2.7C). Thus, the response power of glomeruli with the strongest signals was significantly affected by flow condition.

There exists a relationship between each of these two response features, responsivity and response power, and how well a glomerulus follows plume dynamics. Across all trials, glomeruli with higher responsivity to plume presentations were better at following changes in odor concentration ($r = 0.76$, $p < 0.001$). Thus, the more reliably a glomerulus responded to plume presentations, the more likely it was to better follow changes in odor concentration (Figure 2.6C). These findings were reflected in the supplementary odor panel study, where glomeruli with higher responsivity to plumes had responses that were more correlated with plume dynamics [$F_{(2,116)} = 8.06, p < 0.001$] (Appendix Supplementary Figure 8E sorted bottom to top by increasing correlation magnitude). This is not a perfect relationship as glomeruli that are responsive to the plume but not its dynamics exist (Figure 2.6A), but a glomerulus with higher responsivity is more likely to be correlated to plume dynamics than one with lower responsivity. As mentioned previously, a glomerulus's average responsivity level is also moderated by flow condition. Thus, a glomerulus's responsivity predicts its ability to track plume dynamics and is moderated by changes in dynamic regimes.

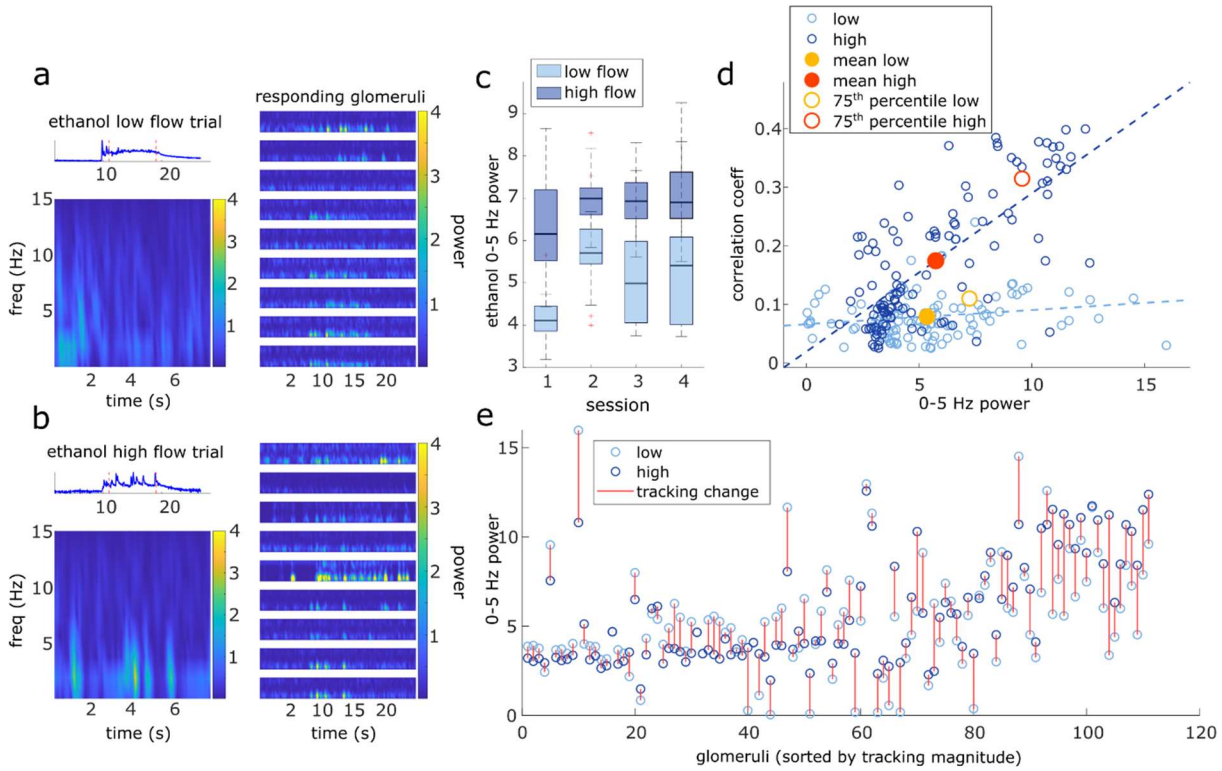

Figure 2.7: Higher magnitude of glomerular response power (0–5 Hz) is associated with higher correlation with plume dynamics.

a) Ethanol signal from a single low flow trial is plotted (top-left) and a corresponding Short-time Fourier transform (STFT) of the plume (time between red dotted lines) is shown below (bottom-left). STFTs are also shown for a sample of glomeruli responding to the plume (right). STFTs show most response power of the glomeruli and odor signal is concentrated between 0 and 5 Hz. Glomeruli STFTs are sorted (top to bottom) by increasing correlation with plume dynamics. **b)** Same as **(a)** but for a single high flow trial from another example FOV. **c)** Box plots for the distributions of stimulus power (0–5 Hz) for all trials within the demarcated flow condition are plotted for each session. On average, high flow distribution means (dark blue) significantly exceeded low flow distribution means (light blue) [$t_{(116)} = 31, p < 0.001$]. **d)** Within both high and low flow conditions, tracking (correlation magnitude of glomerular responses with plume dynamics) is plotted against response power (0–5 Hz power spectrum change between "odor off" and "odor on" periods) for each glomerulus (blue hues, circles). Glomeruli with stronger tracking have a greater increase in response power during plume presentations ($r = 0.74$, $p < 0.001$). When calculated within flow, this relationship is significant within high flow ($r = 0.73$, $p < 0.001$), but not within low flow ($r = 0.19$, $p = 0.05$). The average response across all glomeruli is plotted (low average = yellow dot, high average = red dot) to represent the population response. Mean response power of the glomerular population is not significantly different between low and high flow, except for when calculated with glomeruli whose mean activity is in the 75th percentile (low average = yellow circle, high average = red circle). **e)** Response power of each glomerulus is again plotted, but the change within a glomerulus between low flow (light blue) and high flow (dark blue) is signified by the red line. Glomeruli are plotted sequentially along

the x-axis and are sorted left to right by increasing tracking ability. As tracking ability increases, so does the change in response power between flow conditions. This is consistent with the significant change in mean response between flow condition observed in the 75th percentile [plotted as red/yellow circles in **(d)**].

As for the second response feature, response power was also correlated with how well the glomerulus followed changes in odor concentration, when averaged across all trials glomeruli with higher response power were significantly better at following plume dynamics ($r = 0.74$, $p < 0.001$) (Figure 2.7E). When this relationship was examined within flow conditions (Figure 2.7C), high flow was significantly correlated ($r = 0.73$, $p < 0.001$), but low flow was no longer significantly correlated ($r = 0.19$, $p = 0.05$). This significant correlation in high flow was driven by a subset of the strongest responding glomeruli (75th percentile) whose response power was significantly moderated by flow condition. This relationship between response power and tracking ability (correlation with plume dynamics) was also observed in the supplementary odor panel study where higher average response power predicted higher correlations between that response and plume dynamics [$F(2,116) = 29.2$, $p < 0.001$] (Appendix Supplementary Figure 8C). Thus, a glomerulus's response power predicts its ability to track plume dynamics and for stronger responders, this relationship is moderated by changes in dynamic regimes.

These results suggest that both the reliability and the temporal pattern of MT activity is significantly moderated by the odor concentration dynamics of the incoming stimuli. Thus, the spatiotemporal dynamics of plumes play a role in structuring activity in the first olfactory relay of the mouse's brain during natural olfactory processing.

2.5 Discussion

Mice are adept at olfactory guided search despite the stochasticity and complexity of odor plumes used in navigation. Spatiotemporal cues present in natural odor scenes are thought to drive decision-making in olfactory search (Mafra-Neto & Carde, 1994; Pang et al., 2018; Vickers, 2006), but how they moderate population activity in the olfactory bulb (OB) is unknown. Releasing odor within a custom-built wind tunnel, we were able to hold constant all properties of

the odor stimulus and the animal's position relative to the source and vary only the air velocity through which the plume traveled. By using this approach, we altered the Reynolds number of the flow and created plumes with varying statistical structures and odor concentration dynamics. In this way, the effect of plume dynamics on MT population activity could be examined using naturally evolving odor plumes. Recording MT activity in mice expressing GCaMP6f, we show that a significant fraction of glomerular populations of MT cells follow odor plume dynamics. Additionally, the strength with which they do so is moderated by airflow, such that increased flow velocity and turbulence (Reynolds number) results in increased correlation of MT cell activity with plume dynamics. This work shows that plume dynamics structure the activity of the OB, the first relay of olfactory coding in the mouse's brain.

The recent history of an odor stimulus has been shown to be present in olfactory encoding in both serial sampling of odor concentration in mice (Parabucki et al., 2019) and tracking of odor concentration in invertebrates (Geffen et al., 2009), showing odor concentration changes influence olfactory encoding. Although inter-sniff comparisons in mice show that MT cells can detect the sign and magnitude of changes in odor concentration (Parabucki et al., 2019), it is unknown whether they are able to resolve the dynamics of natural plumes, which span across a range of temporal scales. If odor concentration dynamics are resolved, computational work has shown that they are informative for olfactory search (K. L. Baker et al., 2018; Gumaste et al., 2020). To avoid the complexity of stochastic odor plumes, the averaging of odor concentration dynamics could be an alternative strategy to navigate olfactory environments. Mean odor concentration levels are moderated both by the distance from an odor source and by how close an animal is to the central stream of the plume (Crimaldi & Koseff, 2001). While this measure is potentially informative, it does not by itself sufficiently inform decision-making on

the timescale observed in rodents (Gumaste et al., 2020). Therefore, it is likely that the mouse relies upon spatiotemporal features of the plume for olfactory search as information can be extracted from odor concentration dynamics (K. L. Baker et al., 2018).

Our study found a correlation between MT activity and odor concentration dynamics during plume presentations. The temporal information conveyed by MT cells could support a variety of navigation algorithms. For instance, two important dynamic features are the length of odor encounters, whiffs, and the timing between odor encounters, blanks. Whiff and blank duration are moderated by the distance between an animal and the odor source. As an animal approaches an odor source, plume encounters become shorter and more frequent (Celani et al., 2014; Wright & Thomson, 2005). Blank duration has been shown to be particularly informative even when olfactory environments change. Computational modeling of olfactory search in invertebrates (Park et al., 2016; Rapp & Nawrot, 2020) as well as fluid dynamics modeling (Celani et al., 2014) shows that the time between odor encounters, blank duration, is less sensitive to environmental conditions, such as plume velocity or potency of the odor source that are known to affect interpretation of odor concentration dynamics (Connor et al., 2018; Webster & Weissburg, 2001). Specifically, Park et al., found blank duration to be a more efficient source of information for olfactory search than instantaneous tracking of odor concentration. In our study, we observed that MT activity was more correlated with plume dynamics in high flow trials than low flow trials. Odor concentration in low flow trials was less skewed, meaning that these trials had lower intermittency and odor concentration tended to fluctuate around a central value. Alternatively, high flow trials were more skewed and were characterized by a whiff and blank structure. The fact that correlations are higher in high flow suggests MT activity may be more responsive to whiff and blank features as opposed to tracking fine fluctuations in odor concentration across

more constant plume encounters. One limitation of this study is that medium flow was not statistically distinguishable from high flow, therefore, we were unable to include intermediary intermittency levels between low and high flow conditions in our analysis. Future studies exploring the effect of a broader range of intermittency levels on MT activity during plume encounters could help determine which spatiotemporal features of intermittency are moderating MT responses to plume dynamics.

A network where the majority of glomerular activity responds to concentration dynamics could be considered to be inefficient when the OB has to perform other tasks, such as odor identification and segmentation. Glomerular spatial maps, i.e., glomerular ensembles consistently responding to an odor, are thought to be one of the primary means of odor identification (Wachowiak & Shipley, 2006). Odors maps vary with concentration (Wachowiak & Cohen, 2001; Xu et al., 2000), but are stable enough to reliably encode odor identity (Belluscio & Katz, 2001). Although pulsed odors can be rapidly discriminated (<200 ms, or a single sniff, (Uchida & Mainen, 2003)), in a natural olfactory environment where odors are intermittent (Celani et al., 2014; Murlis et al., 2000) and mixed, identification becomes a much more complicated task especially for identification of mixtures. Glomerular ensembles reliably responding across odor encounters could aid odor discrimination in mixed odor environments. Spatial maps of odor identification will overlap in natural olfactory scenes where an animal encounters signals from multiple odor sources as it navigates a plume. Odors co-released travel together (Celani et al., 2014), and therefore a mixture of odors emanating from the same source will have correlated temporal dynamics in the plume and will thus be experienced by a searcher as having correlated encounters across whiffs. This means the probability of the signal from separate sources arriving together reliably across whiffs would be low if odors are released from spatially separated

sources. Grouping and demixing these odor representations using the correlation, or lack thereof, in the odor concentration dynamics could aid odor discrimination in complex environments (Hopfield, 1991).

Since our studies are not recorded at the individual cell level, the potential degree of heterogeneous tuning to different features among MT cells within a single glomerulus was not examined. It could be that observed correlations of glomerular MT populations were a product of the collective activity of heterogeneously tuned MT cells within a glomerulus, but MT responses have been shown to linearly sum odor inputs (Gupta et al., 2015), which contradict the idea that they are directly tuned to different features of plume dynamics. At the same time, this does not infer MT activity responding to plume dynamics is homogeneous as the responsiveness (Adam et al., 2014) and the response (Geramita & Urban, 2017) varies between MT cells across concentration levels (Cleland & Borthakur, 2020). Future research across a variety of odor concentration dynamic regimes and odor mixtures at both the cellular and population level are needed to further investigate the degree to which bulbar responses are tuned to features of odor concentration dynamics and how this tuning may impact optimal encoding of odor information.

Sniff frequencies are known to influence bulbar oscillations, and thus if sniffing behavior varied significantly between flow conditions, this may have contributed to some of the observed differences in tracking behavior between low and high flow trials. For example, it could be that faster stimulus dynamics in high flow may cause the mouse to miss features of the dynamics due to an inability to resolve them with sufficient sampling speed. However, recent work suggests sniff frequency does not necessarily limit the resolution of plume frequencies in such a manner (Dasgupta et al., 2022). Dasgupta et al. (2022) found subthreshold MT activity was able to couple with frequencies of odor pulsed at supra-sniff frequencies. Thus, if sniff frequency was

moderated significantly between flow conditions, it would not necessarily set an absolute bound on the resolution of plume dynamics. We believe it is important to monitor sniff frequency in the future to observe how it affects inter-sniff and intra-sniff activity, and consequently how these changes relate to tracking behavior observed in MT populations across flow conditions.

Our data show that MT activity in the OB of mice follows the temporal dynamics of odor plumes. Additionally, we demonstrate that this effect is stronger under conditions that generate larger Reynolds numbers. Following odor concentration dynamics within plumes could enable MT cells to convey information useful for olfactory search. Following the temporal dynamics of odor plumes may also be an efficient form of multiplexing odor identity and source location for the first olfactory relay in mice. Although MT activity responds to changes in odor concentration, the observed correlations do not suggest perfect tracking at the level of individual glomeruli and indicate inter-individual differences in the degree to which glomeruli follow plume dynamics. Future research focusing on location encoding across a wide range of both intermittency regimes and odor panels is needed to clarify the degree to which bulbar activity is tuned to features of plume dynamics and how a balance between identity coding and concentration coding is instrumental in supporting the wide variety of behaviors enabled by olfaction.

Chapter 3. Using Neuropixels probes to examine plume following at the cellular level in the main olfactory bulb of awake mice

3.1 Introduction

It has been established that within glomerular networks of the OB, subpopulations of these networks have responses that significantly correlate with odor dynamics during plume encounters (Lewis et al., 2021). The activity of a glomerulus is the collective response of around ~20 mitral cells and ~50 tufted cells (Nagayama et al., 2014), and thus the integrated signal from a glomerulus does not provide insight into cellular level encoding in the OB. Therefore, wide-field observations of GCaMP6f activation lack the spatial resolution to determine if individual cells follow concentration dynamics across plumes or if this is an emergent response at the glomerular level. Here we provide a methodology to examine this question using high-density recordings to capture the response of individual cells in the OB during natural plume presentations. Additionally, we propose a new technical approach for the use of correlated changes between LFP frequency bands as a tool for estimating the location of the MCL in extracellular recordings.

Previous work has shown the feasibility of acquiring high-density, awake extracellular recordings in the OB of mice (Chockanathan et al., 2021; Steinmetz et al., 2021). Here we display the effective use of Neuropixels 2.0 electrode arrays to analyze OB activity responding to the dynamics of natural odor scenes. We record from the OB in head-fixed mice while they are passively exposed to a series of 10-second-long plume presentations. The four-shank Neuropixels 2.0 probe design captures extracellular recording spanning a cortical space approximately ~750 μm by ~720 μm large (Steinmetz et al., 2021). Thus, the use of the four-shank probes captured individual cells across multiple layers of the OB.

To understand the positioning of these cells within the OB, we used coincident physiological features of LFP at multiple frequency bands to estimate the position of the MCL. The OB is known to have strong oscillatory activity across multiple frequency bands (Gervais et al., 2007; Kay et al., 2009; Tank et al., 1994). Relative changes in oscillatory activity across the layers of the OB are tied to the structure and connectivity of specific cell types. As cell types have strong and well documented positions (Imamura et al., 2020; Nagayama et al., 2014; Shipley & Ennis, 1996) across OB layers, changes in OB oscillatory activity can be tied to layers of the OB. Specifically, in the OB LFP, there is a dipole between the GL and GCL across the principal neurons in the theta frequency band (Kay, 2015) and a dipole across the MCL in the gamma frequency band (Rall & Shepherd, 1968; Wróbel et al., 2020). Additionally, the GCL consists largely of axon-less granule cells (GCs) that exhibit dendritic spiking (Nagayama et al., 2014), which has lower amplitude signatures in LFP than axonal spiking (Häusser et al., 2000). Therefore, theta power, gamma power, and high frequency power (representative of cell spiking) all exhibit changes near or at the MCL.

Observing relative decreases in theta power, decreases in gamma, and increases in spiking power of spontaneously evoked LFP across the depth of the probe, we were able to estimate the location of the mitral cell layer (MCL). A continuous wavelet transform based approach was used to estimate power (Cartas-Rosado et al., 2020) in three frequency bands-theta (2-10 Hz), gamma (30-100 Hz) and spiking activity (300+ Hz). Examining how power changed across the rows of electrode sites along each electrode array, we estimated the position of the MCL by locating electrode rows that exhibited these coincident measurements. Co-localized decreases in theta power, decreases in gamma, and increases in spiking power were used to estimate the location of the MCL. These combined measures from new, high-density probes may

be a promising tool for future studies that utilize extracellular recordings to add to their analysis toolkit when estimating the position of electrode recording sites within the OB.

After estimation of the MCL, we analyzed the responses of individual cells. We found subpopulations of cells that significantly responded to plume presentations, establishing our setup is able to simultaneously capture populations of cells responding to natural odor scenes. Manually refined, automated spike sorting yielded on average 58.3 ± 18 cells (mean ± std) per session. Responsivity of the cells to the plumes were variable as observed in our study, but the use of odor panels or other techniques to target cells directly innervated by glomeruli encoding the odor stimulus is likely to provide less variability in future studies, and a way to examine both individual and collective encoding in OB populations while utilizing the high spatiotemporal resolution of electrophysiological recordings. Optically targeted Neuropixels recordings of odor-responsive populations in the OB encoding natural odor scenes could provide an efficient method to begin to answer how populations of cells capture the dynamics of natural odor scenes in the first relay of olfactory processing.

Together the results presented in this chapter of work establish Neuropixels as an effective method for assessing the response of specific cell types of the OB to natural odor scenes using high-density electrophysiology recordings, and provides a method for the use of convergent LFP features to estimate layer positions across the OB in high-density extracellular recordings.

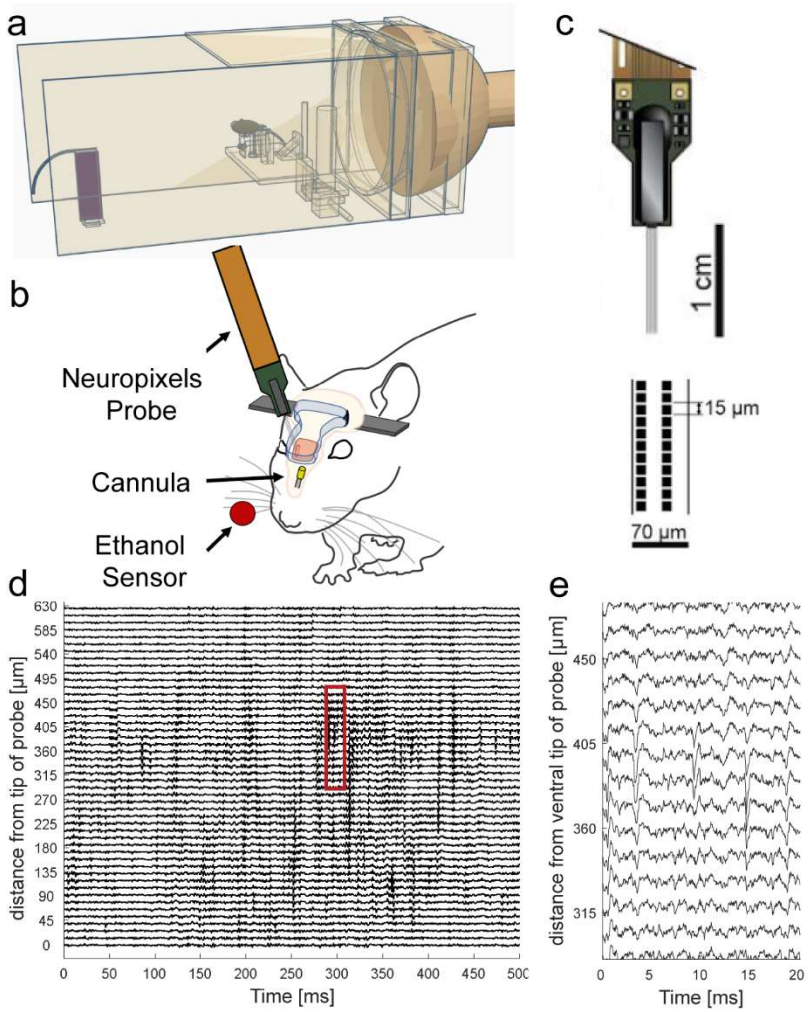

Figure 3.1: Experimental setup for acquisition of high-density electrophysiological recordings using Neuropixels electrode arrays in the OB.

a) Graphic depicting the wind tunnel in which plumes were released by an upwind odor source and pulled through the wind tunnel by a rear exhaust vacuum. **b)** Graphic depicting experimental setup in which simultaneous recordings of neural activity, plume dynamics, and sniffing behavior were obtained. Large-scale neural population activity in the dorsal olfactory bulb was recorded using 4 shank, Neuropixels 2.0 probes. Odor concentration is recorded using a modified, passive ethanol sensor placed ~4mm from the edge of the nostril closest to the sensor. Sniffing behavior is recorded using a pressure cannula. **c)** (top) A schematic of the 4 shank Neuropixels 2.0 probe with a closeup showing the spacing of sites along a single shank (bottom) (Steinmetz., et al 2021). **d)** Raw down sampled recording from the ventral OB shows dense patches of spiking when moving from sites deeper in the OB (further from the ventral tip of the probe) to more superficial and ventral sites. Sites plotted are from the left column of one of the four NP shanks. **e)** A 20ms clip (red box in **(d)**) shows the electrophysiological signature of individual cells displaying strong amplitude spiking events across multiple recording sites.

3.2 Materials and Methods

3.2.1 Mice

Experiments were performed on seven B6 mice (one female and six male) from the Jackson Laboratory (Strain # 000664) between 14-17 months of age. Animals were maintained on a 12-hour reverse light/dark cycle. All experimental procedures were approved by the Institutional Animal Care and Use Committee at the University of Washington.

3.2.2 Olfactory Stimuli

Olfactory stimuli were released by an automated odor port within a 40cm x 40cm x 80cm acrylic wind tunnel where airspeed was controlled by a vacuum at the rear of the wind tunnel, posterior to the animal's location (Figure 3.1A). Concentration dynamics of olfactory stimuli varied stochastically from trial to trial creating plumes with unique concentration dynamics on each trial. Plumes were created using the methods as described in Lewis et al., 2021 and in Chapter 2, such that odor vapor was released upwind of the animal in the wind tunnel, and then a vacuum exhaust at the rear of the wind tunnel pulled the odor plume past the animal. Each session consisted of 60 trials (except two sessions, 22 and 31 trials in duration respectively, were terminated early due to odor sensor acquisition errors). In each trial, mice passively experienced a 10-second-long plume presentation of the odorant mixture.

Ethanol concentration throughout each trial was measured as described in Lewis et al., 2021 by using a modified, commercially available ethanol sensor placed within 3.5-4mm from the mouse's right nostril (Figure 3.1B). For all sessions, an odorant mixture of 5 odorants was used to try to increase the number of responsive glomeruli and ethanol was used as a tracer for

the ethanol sensor to capture the odor concentration. The same mixture ratio (0.3% ethyl tiglate, 0.3% methyl tiglate, 0.3% allyl butyrate, 0.3% isobutyl propionate, 0.3% ethyl valerate, 92.8% 200 proof ethanol, and 5.7% distilled water) was used for 9 of the 10 sessions. For the first session of the 10 sessions a mixture with a slightly lower ethanol percentage was used (0.6% ethyl tiglate, 0.6% methyl tiglate, 0.6% allyl butyrate, 0.6% isobutyl propionate, 0.6% ethyl valerate, 85.7% 200 proof ethanol, and 11.3% distilled water), but the ethanol was increased for future sessions to optimize the odor concentration signal of the ethanol sensor. Odor solutions were stored in odor reservoirs (centrifuge tubes) with air-tight, customized tops. Tops had two openings connected by tubing. One tube was connected to a Clippard electric valve (part no. EV-2-12) to create airflow and the other was attached to a 3D printed odor port. For each plume presentation, the valve was opened to allow airflow into the tube such that odor vapors exited the odor reservoir and traveled through cylindrical tubing (1/16” inner diameter) to the release point at the odor port.

3.2.3 Surgery

The mice underwent two surgeries prior to electrophysiological recordings. During the time between surgeries, animals were conditioned to the head-fix setup. For the first surgery, a cannula and head plate were implanted. After a complete recovery was made from surgery, mice were conditioned to the head-fix setup. The second surgery, a craniotomy over a dorsal area of the main olfactory bulb, was then performed. For both surgeries, Mice (n = 7) were anesthetized with isoflurane for surgery.

During the first surgery, a custom-built cannula (see Sniff Monitoring) was implanted in the style of (Findley et al., 2021) over one of the mouse's nostrils. Next, a customized stainless-steel head plate was glued directly on the skull centered near lambda coordinates. White

Metabond (Radiopaque) was then added to cover all exposed skull except for the skull above the olfactory bulbs. Over the bulbs, a layer of clear Metabond was used to cover the skull. This allowed for easy targeting of the bulbs during the craniotomy procedure later. Once the animal recovered from this surgery (2-3 days), handling and subsequent conditioning to the head-fix setup began.

Once the animal was conditioned to the head-fix setup (1-2 weeks), the second surgery, a craniotomy, was performed a 1mm x 1.5mm rectangle was removed above one of the two olfactory bulbs. First, a dental drill was used to remove the clear Metabond over one skull. Then, a small well was drilled into the white Metabond caudal to the bulb to hold more ringer's solution during the grounding (this protected the grounding solution from evaporating in the wind tunnel during recordings). A gold-plated socket (Newark D Sub contact socket, 66504-9) was attached with super glue resting into the bath space so that the grounding pin could be securely and easily attached during surgery. The craniotomy was then performed and then Kwik-Cast (Silicone Elastomer) was applied to seal off the craniotomy. Afterwards a small wall was built using rings of superglue each cured with Zip Kicker (CA accelerator) immediately after application to create a pool (Figure 3.1B) to hold the ground solution. Zip Kicker was used sparingly and care was taken to make sure it was applied only on the outside of the rings so that the Zip Kicker did not touch the inside of the pool where the Ringer's solution would later reside. After, a layer of Krazy glue was applied to the outside of the wall and cured with the accelerant to make sure the pool was leakproof. The pool was gently rinsed multiple times with sterile saline solution.

3.2.4 Sniff Monitoring

Cannulas were used to measure airflow through intranasal pressure (Verhagen et al., 2007). Cannulas implants and surgical implantation followed methods of Smear et al., 2011 (Smear et al., 2011). For sniff measurements, a Polyethylene tubing was used to connect the cannula to a Sensirion SDP37 differential pressure sensor, mounted on a custom-designed PCB, allowing for high precision pressure monitoring within the nasal cavity. The data from the pressure sensor was acquired through a National Instruments USB 6009 DAQ. Sniff signal was not used in the analysis presented within this thesis.

3.2.5 Electrophysiological Recordings

Four shank Neuropixels 2.0 electrode arrays were used to record bulbar activity during plume presentations. Probes were mounted on dovetail caps (uMp-NP2-CAP) with Metabond. The caps were attached to extension rods (uMp-NPR-200) by Neuropixel adapter heads (uMp-NPH). The extension rods were held by a four-axis micromanipulator (uMp-4).

Across the 5,120 possible recording sites, up to 384 can be chosen for simultaneous data acquisition. For all recording sessions, the bottom most 96 sites from each of the four shanks (the bottom 48 rows on each shank) were selected. Together, the four shanks covered an area of ~750µm wide and ~720µm deep, allowing for multiple layers of the OB to be captured simultaneously with sites placed 15µm apart along each shank. Probes were inserted into one olfactory bulb such that the four shanks ran in a rostral to caudal direction along the sagittal plane of the OB. Recordings targeted either the dorsal (3/10) or ventral (7/10) OB. Recording sessions favored the ventral OB as stronger spiking activity was observed there, as has been previously reported (Paseltiner et al., 2020), facilitating stronger signal to noise ratio for isolating units in spike sorting.

Recordings were either performed on the same day as the craniotomy (n = 8 of 10) or on the day after (n = 2 of 10). For recordings performed on the same day, the mouse was anesthetized using isoflurane for surgery performed in the morning, and then recordings were performed in the afternoon once the mouse had fully recovered. Before the recording began, the Kwik-cast was removed and the grounding pool was filled with Ringer's solution. Recording were made using an external reference, and for grounding, a gold-plated pin (Newark D Sub contact pin, 66506-9) soldered to an Ag wire (A-M Systems, No. 787000) was inserted into the socket in the grounding bath (see Surgery) with the other end of the wire soldered to the probe. The probe was then advanced into the OB and allowed to settle for 15-25 minutes prior to the start of the recording.

For the single shank recording of spontaneously evoked activity used in Supplemental Figure 3.2.1, surgery and electrophysiological acquisition are done in the style of Steinmetz et al., 2021. These plotted data show findings of LFP and spiking near the estimated MCL in four-shank recordings spanning ~750 μm (a distance shorter than the dorsal/ventral axis across most of the OB) qualitatively reflects activity near the estimated MCLs of a single shank spanning ~1.8mm. This recording was done during an odor-less, spontaneously evoked period of activity. As this recording did not use the same experimental setup described in the methods, spontaneously evoked activity is plotted, but data is not included further in any analysis reported in this paper.

3.2.6 Data Analysis

Neural recordings were acquired using SpikeGLX (https://github.com/billkarsh/SpikeGLX). The data was next automatically spike sorted using

Kilosort3 (https://github.com/MouseLand/Kilosort), and then manually curated using phy2 (https://github.com/cortex-lab/phy).

Units with contaminated refractory periods, unstable firing rates across the session, or waveforms indicative of multi-unit activity were marked as 'Multi-Unit Activity', and their use is explicitly labeled as such whenever discussed in the paper. Recordings without at least 25 good cells were excluded from analysis.

Matlab 2021a was used to analyze data and plot figures. Code by Nick Steinmetz from the Spikes repository (Waveform statistics and plotting: https://github.com/cortex-lab/spikes) and the npy-matlab repository (https://github.com/kwikteam/npy-matlab) were used, as well as code by David Tingley from the Buzode Repository (CCG plots: https://github.com/buzsakilab/buzcode).

3.2.7 Analysis of Frequency Bands Using a Continuous Wavelet Transform Based Method

To estimate power across frequency ranges, we used a continuous wavelet transform method (CWT) as described in Cartas-Rosado et al 2020 (Cartas-Rosado et al., 2020). Amplitude plots and power estimates for each frequency band were calculated using neural activity across 5 seconds of the inter-trial interval, a time in which no odor or other stimulus was presented. The signal was first down sampled from 30 kHz to 1 kHz, and then transformed into the time frequency domain using the CWT Matlab function (cwt). The amplitude of these frequency ranges over time were extracted using the inverse continuous wavelet transform Matlab function (icwt). Frequency ranges extracted were theta (2-10 Hz), gamma (30-100 Hz), and spiking (300-434 (limit with sampling rate)) frequency ranges. The power for each frequency band was defined as the square of the root mean square amplitude values. The activity from an 8 second long clip was transformed and inverted, but only the middle 5 seconds of the clip were used for

the power estimation to ensure all CWT coefficients used were located outside the cone of influence, protecting against known edge effects of the CWT.

3.2.8 Estimation of the Mitral Cell Layer

The MCL(s) for each shank were estimated by eye based on LFP, density of spiking and spike amplitude during recording sessions (no histology was performed). The row of recording sites estimated to lie along the MCL was hand scored using 3 parameters: theta amplitude, gamma amplitude, and spiking amplitude.

LFP polarity reversals are due to transitions between sources and sinks in extracellular recordings. In previous research, the point of polarity reversal in LFP across the depth of the bulb has been used to locate the MCL in extracellular LFP recordings without histological identification of the MCL (Fourcaud-Trocmé et al., 2014). In our study, we searched for transitions between sources and sinks, or dipoles, as indicated by areas of low amplitude in the LFP. The OB has dipoles that can be observed in the LFP at both theta (X. Hu et al., 2022; Kay, 2015) and gamma (Rall & Shepherd, 1968; Rojas-Líbano & Kay, 2008; Wróbel et al., 2020). As theta and gamma frequencies are thought to be generated by unique circuitry in the OB (Fukunaga et al., 2014), the sources and sinks associated with these oscillations are not interchangeable. Therefore, we determined the location of the MCL using coincident changes in both theta and gamma LFP amplitude across the depth of the OB. For theta, polarity reverses across the principal cells, between the GL and the GCL (Kay, 2015), and for gamma polarity reverses at the MCL, between the EPL and the IPL (Rojas-Líbano & Kay, 2008). As the theta dipoles were not localized as strongly with the MCL location as the gamma frequency, gamma frequency changes were prioritized and a change in theta power near the MCL was used as supporting evidence. Therefore, reductions in theta power in the vicinity of the MCL and reductions in gamma power

at the MCL are both used as localizers. Additionally, spiking power should drop when crossing the MCL into deeper tissue, as without principal somas, the GCL and IPL consist predominantly of axon-less granule cells (Nagayama et al., 2014). In this way, coincident transitions to low theta power, low gamma power, and high spiking power were used to pinpoint the recording sites within the MCL.

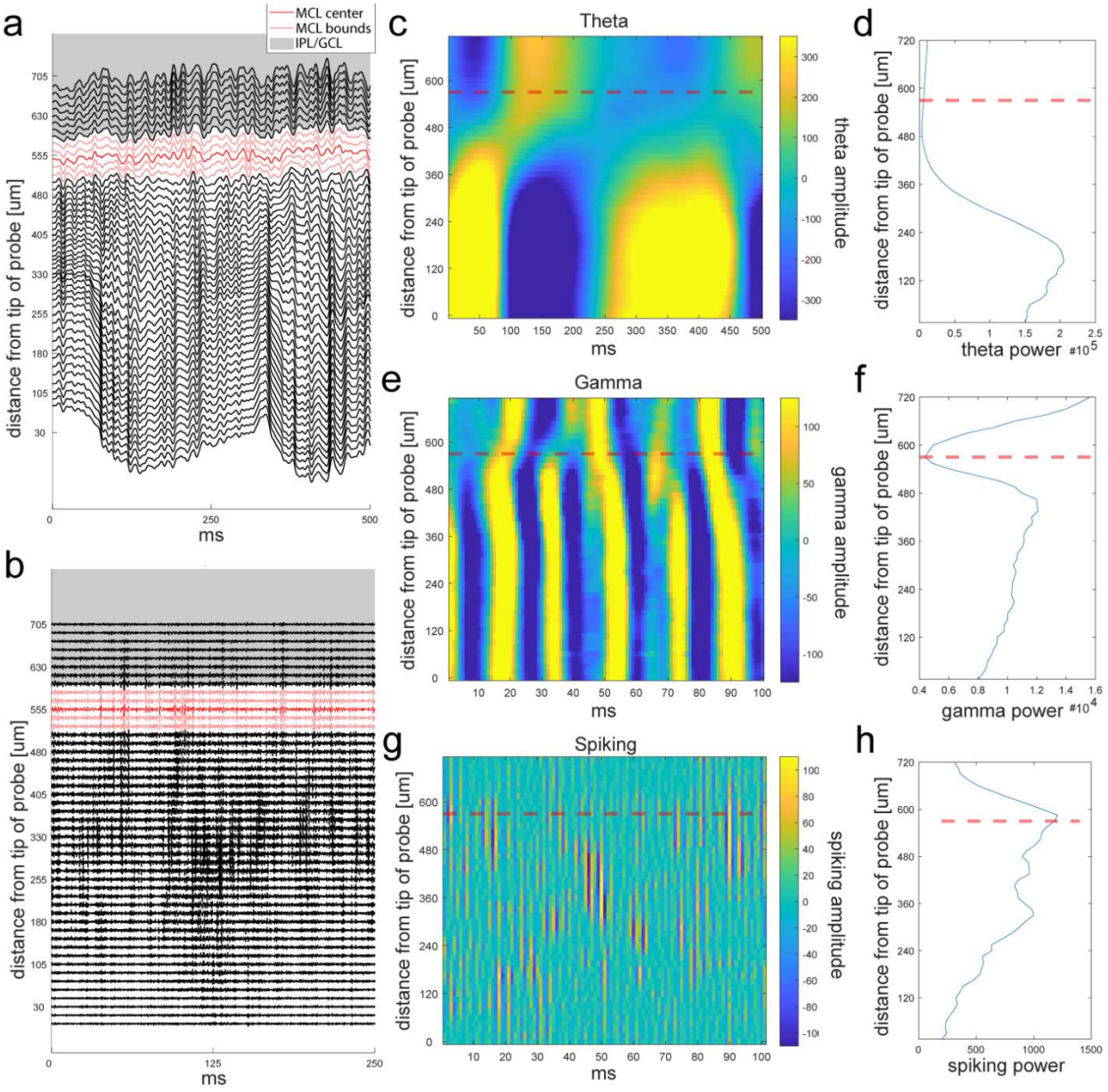

Figure 3.2: Estimating the location of the MCL by characterizing frequency band power changes across recording sites.

a) Bandpass filtered LFP activity (1-100Hz) from one column of a single shank during a recording of the ventral OB smoothed with a gaussian filter with a std of 3.3 ms and down sampled by a factor of 10. The estimated center of the MCL (dark red) and the estimated boundaries of the MCL (light red) are indicated. The plot displays differences in LFP activity when moving from ventral superficial OB layers towards the deeper OB layers (further distances from the ventral tip of the probe). The IPL/GCL side of the estimated MCL indicated by gray shading. **b)** A bandpass filtered clip (300-3000 Hz, down sampled by a factor of 5) from the recording sites plotted in **(a)** captures spiking activity and shows dense clusters of spiking near the MCL and superficial to the MCL. **c)** Theta LFP (2-10 Hz) amplitude plotted across 500ms from the same recording sites **(a)** extracted using CWT based method show polarity reversal in

theta frequency amplitude in the vicinity of the MCL. **d)** Plot of average theta power for each recording site calculated from theta amplitude across a 5 second period of spontaneous activity. **e-f)** Same as **(c-d)** but for gamma frequency band amplitude (30-100 Hz) showing a drop in gamma amplitude near the MCL and, in this case, a reversal of amplitude polarity on either side of the MCL. **g-h)** Same but for spiking frequencies (300-434 Hz) showing most of the spiking amplitude decreases rapidly when moving away from the MCL towards the IPL/GCL.

If a shank did not have a drop in gamma power coincident with a rise in spiking power, the shank was labeled as not crossing the MCL. Data from these shanks were not used in the analysis. Also, a reduction in all power frequencies indicates the recording site is above the dorsal surface (Figure 3.2.1 E,J,I).

For all recordings, recording site rows more superficial than the estimated MCL edge are referred to as EPL/SFLs. Those deeper are referred to as IPL/GCL.

3.2.9 Evaluating changes across the estimated MCL

Before analyzing mean power across shanks, power was normalized between 0-1 for each shank within each frequency band such that only relative changes in frequency across each shank were considered.

When comparing the power on either side of the estimated MCL, the power for each side was calculated using all sites within 240μm of either edge of the MCL. For the shanks that had less than 240μm distance of electrode site rows on one side of the MCL, the available sites were to calculate the average. If the MCL was at the edge of the probe and no electrode site rows were available on one side of the shank, only one side of the shank was included in the analysis. A Wilcoxon rank-sum test was used to determine if the power change was significant.

3.2.10 Waveform Analysis of Cells

To calculate the location of cells and their waveform amplitudes, 1000 waveforms were randomly extracted using the Spikes Repository function getWaveForms. The mean waveform was then calculated for each recording site. The recording site with the largest amplitude change between the minimum and maximum amplitude value was used to define the location of the cell or cluster across the electrode array. Waveform amplitude was defined as the maximum amplitude change across all recording sites.

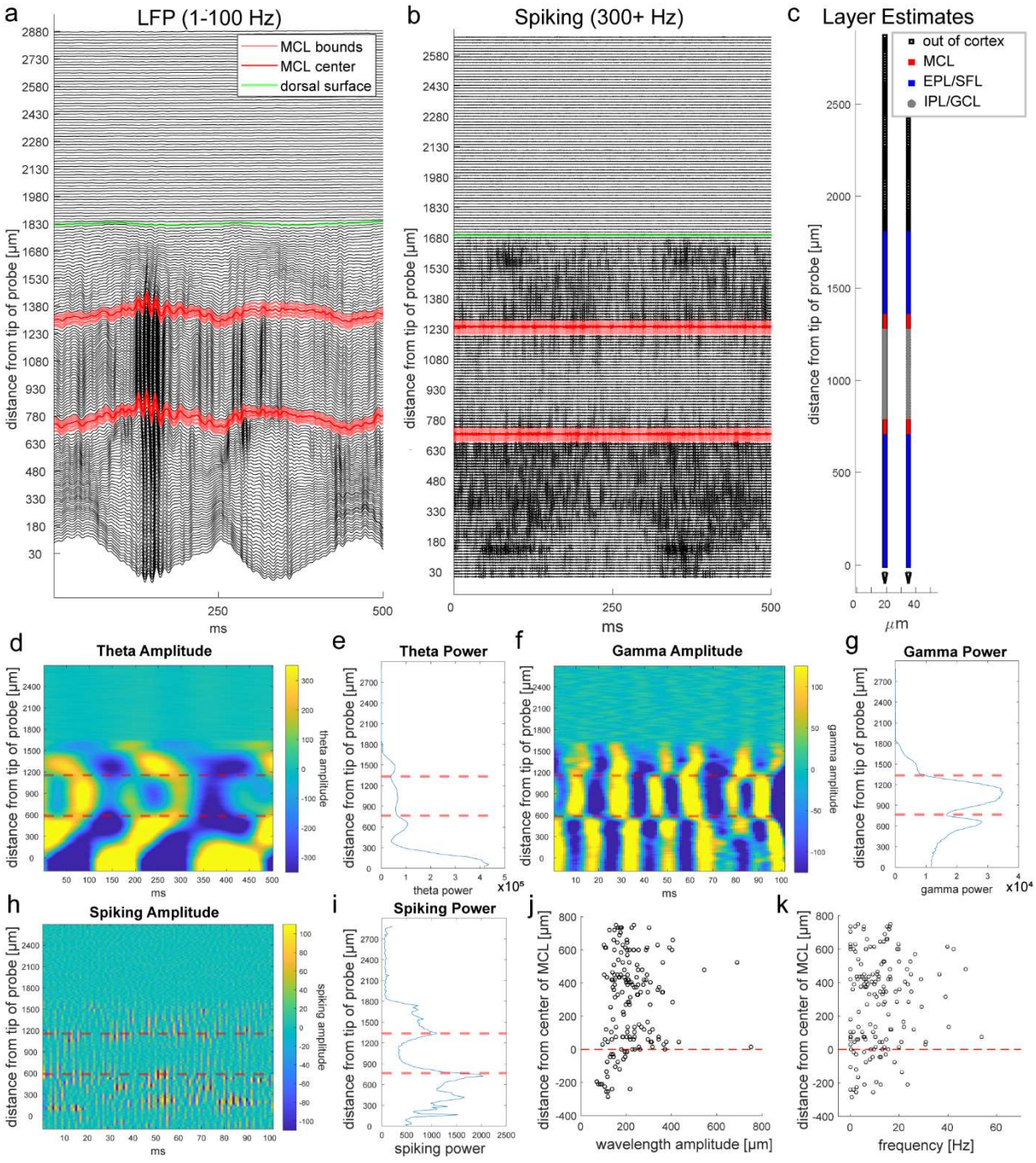

Figure 3.2.1: A single shank Neuropixels 2.0 recording shows changes in LFP and spiking activity across the dorsal/ventral span of the OB.

a) Bandpass filtered LFP activity (1-100 Hz) from a single shank Neuropixel 2.0 electrode array, smoothed using a gaussian filter with a std of 3.3ms, covering ~1.8 mm from the dorsal surface (green) towards the ventral OB. The estimated dorsal and ventral MCL are indicated (center of MCL dark red, bounds of MCL light red). The plot displays changes in LFP activity when moving from the dorsal surface (green line) towards the ventral OB. The IPL/GCL (grey)

between the MCLs is indicated. **b)** A bandpass filtered clip from the same recording captures spiking activity (300-3000 Hz), showing dense clusters of spiking stretching from dorsal and ventral superficial layers to the estimated MCLs. Notably, the central OB (deep layers) displays the least spiking across the bulb. **c)** A schematic of the recording sites across the probe shows the classification resulting from the estimation of the MCLs. **d)** Theta LFP (2-10 Hz) amplitude extracted using CWT based method show polarity reversal in theta frequency amplitude in the vicinity of the estimated MCLs. **e)** The average theta power is plotted along the depth of the shank pictured in **(c)** showing local minima near the estimated MCLs. Theta power is calculated for each recording site along a single column of one shank during a 5 second period of spontaneous activity. **f-g)** Same as **(d-e)** but for gamma frequency band amplitude (30-100 Hz) showing a drop in gamma amplitude near the MCL and in this case the amplitude reflects a strong polarity reversal near the ventral MCL. **h-i)** Same but for spiking (300-434 Hz) showing most of spiking amplitude decreases rapidly when moving away from the MCL into the IPL/GCL and towards the center of the OB. **j)** The waveform amplitude for each cell is plotted against its distance from the center of the MCL (positive direction is superficial to the MCL, negative is deep). **k)** The same is shown for the relationship between spiking average spiking rate and the distance from the center of the MCL for all cells.

3.2.11 Plume Responsivity of Cellular Responses

A cell was considered to be responsive to odor if its firing rate exceeded threshold more time windows than expected by chance during plume presentation as compared to its activity level during odorless baseline periods (Figure 3.5). Since this preliminary measure does not rely on stimulus dynamics, it captures cells that respond to the plume even if their response is unrelated to odor concentration dynamics or only present for part of the plume.

First, the spiking activity of a cell was split into two periods: baseline activity and odor response. The baseline period is a 6 second period at the beginning of each trial prior to plume onset. The odor response period is the first six seconds following the first whiff of the plume (scored by eye). The signal is then divided into 200ms bins (a time period comparable to a single sniff), and the number of spikes is summed across each bin.

First, the difference in the distributions of spike count values between the baseline and plume periods were tested for significance. Using the Matlab crosstab() function, a contingency table was created comparing frequency counts across the observed range of spike count values in baseline periods as compared to plumes periods for each cell. Significance was determined using a chi-squared test with an alpha of 0.05.

If the cell's spike count distribution changed significantly between periods, the responsivity was calculated as follows. The spike count values across both the baseline and plume periods are baseline normalized within trial by diving by subtracting the mean spike count for the trial's baseline period and dividing by the standard deviation spike count for the trial's baseline period. Next, the values are binarized, thresholded at ±1.96 to capture time bins for which activity exceeded the middle 95% of the null exception for spiking activity (cell's baseline distribution of spike counts across time windows). In this way, each time window that crossed

the threshold was considered an event. Within each trial's plume period, if the number of events exceeded the null expectation (5% of the total number of time windows during the plume period) the cell was considered to be responsive to the plume during that trial. The proportion of trials to which the cell significantly responded was reported as the plume period responsivity.

Next, we calculated the baseline period responsivity. As distributions of spike counts across windows are not presumed to be gaussian, setting a threshold of ±1.96 standard deviations of the baseline mean spiking average may lead to threshold crossings at a rate other than 5%. Therefore, we subtracted a cell's baseline period responsivity from the plume period responsivity to ensure we account for any baseline threshold crossing rates other than 5%. If cell's baseline period responsivity was higher than its plume period responsivity resulting in a negative total responsivity score. Negative scores do not represent inhibited cells, as the threshold crossing is counted whether in the positive or the negative direction. Instead, this likely represented that the cell's response had less variability during plume presentation, and though this may be considered a type of response, it was not a type considered in this analysis (1 MC and 1 EPL/SFL cell met this criterion). Cell's with a total responsivity score of 0 after baseline subtraction were also excluded from the analysis due to the lack of change in responsivity between periods (2 MCs met this criterion). Therefore, the responsivity, or total responsivity score, was calculated as the proportion of plume periods to which the cell responded subtracted by portion of baseline periods to which the cell responded.

Therefore, to be considered as having significant responsivity, a cell must have a significant change in their spiking distribution between baseline and the plume and must also have a positive responsivity score after accounting for the baseline threshold crossing rate.

3.3 Results

3.3.1 High-Density Electrophysiological Recordings of the OB using Neuropixels electrode arrays

In order to understand how individual OB cells contribute to the plume following behavior of glomerular networks (Lewis et al., 2021), it is necessary to simultaneously record large cell populations responding to plume dynamics. In this work, we establish Neuropixels probes as a method to obtain high-density electrophysiological recordings of local OB populations in awake, head-fixed mice. Our experiment used Neuropixels 2.0 electrode arrays to record the activity of OB populations (Figure 3.1) both during baseline periods without odor exposure and during natural odor scenes consisting of passive plume presentations.

3.3.2 Changes in Frequency Band Activity Across the OB and the Relationship of power between frequency bands when aligned to the estimated MCL

After estimating the location of the MCL (Figure 3.3 a), each row of electrode sites was aligned to the center of the MCL. If the alignment agrees with our assumptions regarding the distribution of theta power, gamma power, and spiking near the MCL, then we should see some relationship between these three variables after alignment. Mean gamma power was positively correlated with mean theta power for each electrode site across all shanks ($p<0.001$, $r(1113) = -0.48$), confirming electrode sites with higher gamma power were more likely to have higher theta power as well. Additionally, spiking was significantly inversely correlated with both theta ($p < 0.001$, $r(1113) = -0.37$) and gamma ($p < 0.001$, $r(1113) = -0.60$). Plotting the normalized theta, gamma, and spiking powers (Figure 3.3B) for each electrode site against the depth of the site relative to the MCL shows that although the strong relationship between gamma power and spiking power. Theta, show more variation, consistent with polarity reversal of theta being less closely related to the MCL as discussed previously. Due to the significant relationship between

the three variables in a manner consistent with the hypothesis, MCL estimates were used to align data in this analysis to the MCL. As these relationships are somewhat variable between shanks, this analysis has refrained from assigning more exact layers (OSN, GL, EPL, MCL, IPL, GCL) and will instead refer to cells as lying in the estimated MCL as MCL, cells lying superficial to the MCL as the EPL/SFL (EPL and superficial layers (SFL)), and cells lying deeper than the MCL in the IPL/GCL.

Power was also calculated across theta, gamma, and spiking frequencies for one single shank recording of spontaneously evoked activity (Figure 3.2.1). A single shank traversing the dorsal/ventral axis should only cross the MCL twice, and the single shank recording accordingly shows only 2 areas on the shank consistent with our hypotheses of LPF activity near the MCL. These two areas on the shank show spiking power rising from negligible levels coincident with both gamma and theta polarity reversals as exhibited in the amplitude plots (Figure 3.2.1 D,F,H) and drops in theta and gamma power (Figure 3.2.1. E,G,I).

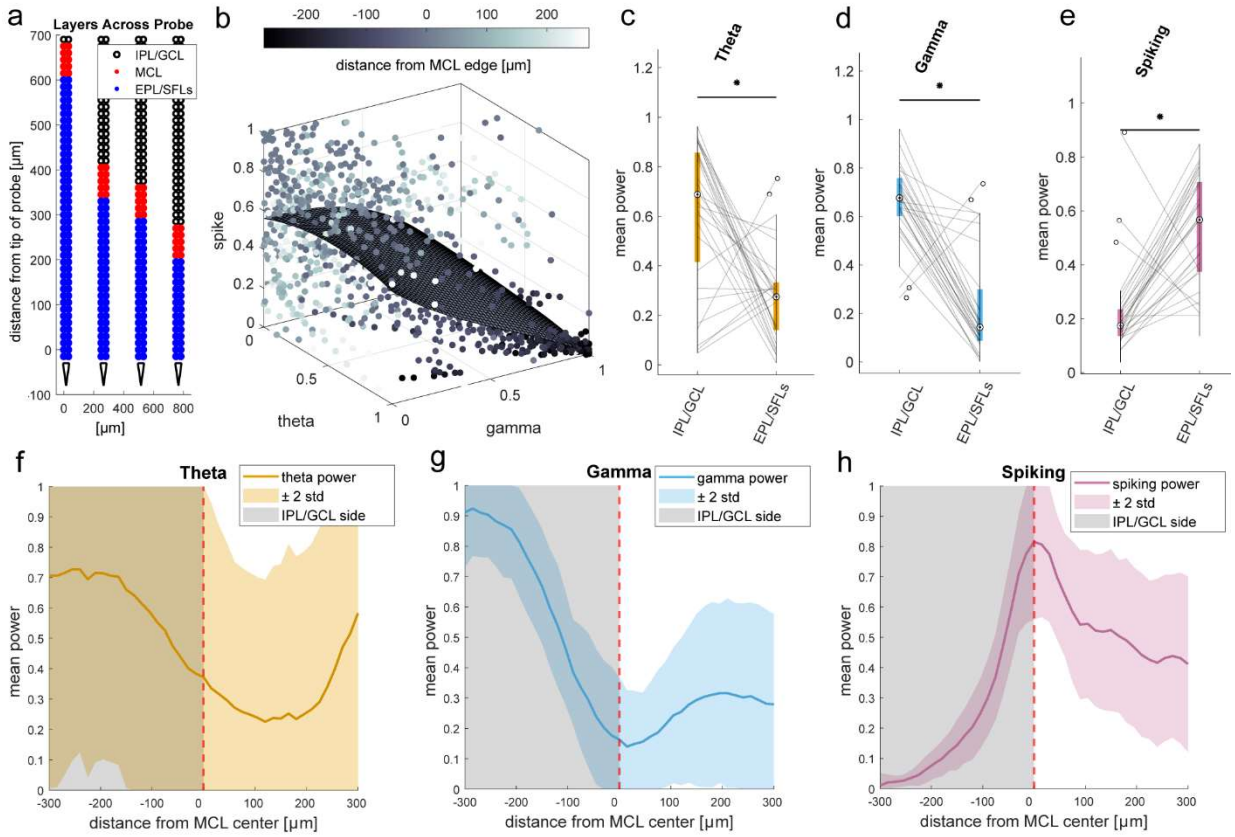

Figure 3.3: LFP changes relative to the estimated MCL.
a) A schematic for estimated layers across all four shanks from a single recording session of the ventral OB with the IPL/GCL (black), the MCL (red), and the EPL/SFL (blue) indicated. **b)** Plotting the gamma, theta, and spiking power of each electrode site against the site's distance from the MCL (indicated by colormap, negative towards IPL/GCL) shows a nonrandom relationship between the power at different distances from the MCL. Particularly, sites in the IPL/GCL show few instances of electrode sites having both high gamma power and high spiking power, reflecting the strong inverse relationship between gamma power and spiking power (p<0.001, r(1113) = -0.60). **b)** For all shanks across all sessions, the distributions of mean power for both sides of the MCL at each frequency band are plotted as boxplots. Mean power as compared between the superficial (EPL/SFL) and deep (IPL/GCL) sides of the estimated MCL is significantly different on average for all three frequency bands (Wilcoxon rank sum test, p<0.01). For each shank, the two sides are connected (gray line), unless the estimated MCL was located at the edge of the shank resulting in only one side available. **d-e)** Same but for gamma power and spiking power respectively. **f)** Mean theta power (line) ±2 std (shading) across all shanks plotted as a function of distance from the MCL center shows that the exact point at which theta power drops off or reverses polarity relative to the estimated MCL (gamma drop off and spiking rise) is not reliable resulting in high variance for the drop in Theta power relative to the estimated center of the MCL. **g)** The same is plotted but for gamma power. The drop off or polarity reversal of gamma power was useful in reliably estimating MCL location, as is shown by its strong relation to the center of the estimated MCLs across shanks. **h)** The same is plotted

for spiking power, showing a reliable rise in power when moving the GCL to EPL/SFLs, consistent with the emergence of high voltage pyramidal cell activity characteristic of the OB.

3.3.2.1 Theta Power

In the LFP of extracellular recordings, there is a dipole observed at slower rhythms in the OB, reversing polarity across the principal cells of the OB (EPL/MCL) (Kay, 2015). The polarity reversal is not coincident with MCL, but rather the MCL is bounded by the GCL and the GL across which the theta reversal occurs. Recent *in vitro* recordings across an entire slice of the olfactory bulb, found theta frequency primarily in the GL and GCL, corroborating the hypothesis that theta power should be lower in the EPL/MCL/IPL area. Though changes in theta power are exclusively positioned within the MCL, theta power should change near the edge of the GCL if it is to have higher power there relative to its nearby more superficial layers. We found mean theta power to be significantly different on either edge of the MCL when measured within 240μm of both edges (Table 3.1). Pooling all recording shanks across all sessions, we found mean theta power to be significantly higher on the IPL/GCL of the MCL ($Md = 0.66$, $n = 31$ of 34 shanks) than on the EPL/SFL side ($Md = 0.23$, $n = 32$ of 34 shanks) as determined by a Wilcoxon rank-sum test ($Z = 5.79$, $p < 0.001$, $d = 1.39$) (Figure 3.3B). As the EPL/SFL side is only measured within 240 μm of the edge of the MCL, it is likely to consist largely of the EPL as opposed to more superficial layers as the EPL is around ~200 μm in width (Hamilton et al., 2005). Despite the significant differences when measuring across all shanks, the exact moment at which theta changes relative to the center of the MCL was variable (Figure 3.3F) as shown by the ±2 std error bars depicting the variance of power at each depth relative to the center of the estimated MCL. Additionally, power within shanks was calculated at the individual level. For each shank, a rank-sum test compared the theta power measure for electrode sites on either side of the MCL, and 58.8% (20/34) of shanks had significant power changes across the MCL. Of shanks that reached significance, 10% (2/20) showed higher theta on the EPL/SFL side of the MCL. Thus, in

our recordings of bulbar activity without odor input, the relationship between the estimated MCL and theta was variable, but at the population level, theta power significantly increases on the IPL/EPL side of the MCL reflecting know changes in LFP in low frequency bulbar oscillations.

3.3.2.2 Gamma Power

Another important oscillatory band of the OB, gamma, is often hypothesized to be a result of reciprocal dendrodendritic interactions between mitral and granule cells (Lagier et al., 2004; Rojas-Líbano & Kay, 2008). In support of this hypothesis, optogenetic silencing of GCs was observed to significantly lower the power of gamma oscillations in the OB, despite not significantly altering theta power (Fukunaga et al., 2014). The dendrodendritic hypothesis suggests that the excitation of an MC excites GCs to which it has dendrodendritic connections. The GCs then inhibit the MC in return, as well as other MCs to which they share dendrodendritic connections. This creates a negative feedback loop and expands the influence of the inhibition to larger MC populations via lateral inhibition. Over a window of time, the excitation of MCs combined with the local negative feedback loop leads to alternating phases of excitation and inhibition periods in the gamma frequency range (Rojas-Líbano & Kay, 2008).

The gamma oscillations create sinks and sources in the extracellular LFP that reverse polarity across the MCL (Rojas-Líbano & Kay, 2008). When the MCs are excited, there is a net influx of current to their dendrites and to dendrites of GCs they have excited, resulting in a sink in the LFP superficial to the MCL. In turn, deep dendrites and granule somas have a net outflux of current, creating a source in the LFP beneath the MCL. Thus, the sinks and sources of gamma oscillations lead to a polarity reversal near the MCL. Calculating gamma power across time, the area near the center of the reversal will display low amplitude. Thus, the MCL, the area near the polarity reversal of gamma oscillations, displays less gamma power than its surroundings,

creating a local minimum. In our studies, we observed a significant increase in gamma power on the IPL/GCL side of the MCL (m = 0.66, std = 0.15) as compared to the EPL/SFL side (m = 0.23, std = 0.22) as determined by a rank-sum test (Z = 5.79, p < 0.001, d = 2.27) (Figure 3.3D). At the individual level, 67.7% (23/34) of shanks had significant power changes across the MCL. Additional variance was observed as a minority of shanks did not show high power in the GCL, but instead power increased moving away to layers superficial of the MCL. Of shanks that reached significance, a minority of shanks (2/23) showed higher gamma on the EPL/SFL side of the MCL. Despite this variability in which side of the MCL had higher power, there was a significant change between the two side of the MCL and between gamma power in the MCL (m = .17, std = 0.20) and gamma power in the IPL/GCL (z = 6.17, p < 0.001, d = 2.7353) (Table 3.2). Gamma power was not significantly different between the MCL and the EPL/SFL, suggesting transitions were steeper on the deep side of the MCL as is illustrated in the full shank recording (Figure 3.2.1G). Across the shanks, after alignment we observed strong changes in gamma power near the MCL, and gamma power tended to be higher on power in the IPL/GCL side of the MCL.

3.3.2.3 Spiking Power

The third parameter used was spiking power, defined as power in the 300 Hz+ range (300-434 Hz). As granule cells are axon-less cells and rely on reciprocal dendrodendritic connections, the spiking activity observed in the GCL is generally dendritic spiking which exhibits lower amplitude waveforms in the extracellular LFP than axonal spiking (Häusser et al., 2000). Additionally, the majority of GCs are not observed to spike during spontaneously evoked activity (Cang & Isaacson, 2003), and power was evaluated only during spontaneously evoked activity. As a result, spiking amplitude in the GCL as measured during spontaneously evoked

activity in extracellular electrophysiological recordings is likely negligent when compared to OB layers containing the somas and dendrites of OB cells with axons. In our recordings we observed a significant drop in spiking power for areas of the shank located deeper than the MCL. Spiking power was significantly lower in the IPL/GCL (m = 0.22, std=.16) as compared to the EPL/SFL (m = 0.52, std = 0.20) (z = 5.79, $p < 0.001$, d = 2.27) (Figure 3.3E). The MCL (m = .77, std = 0.20) has significantly higher spiking power than either side (Table 3.1). Principal cells in the EPL, tufted cells (TCs), have been found to have higher odor elicited firing rates than MCs (Burton & Urban, 2014), but we evaluated spontaneously evoked spiking activity during a window of the session in which no odor was present. Additionally, spiking power includes many factors other than firing rate. Higher waveforms amplitude or a larger population of cells in the recording range could both lead to increases in spiking power. The MCL is more densely populated with principal cells than the elsewhere in the OB (Burton, 2017), making it more likely that MCs may first, be found closer to electrode sites, and second, be present in larger numbers within the recording range. This would lead to an increase in waveform amplitude and cell number respectively, which could both contribute to increased spiking power coincident with MCL. It should be noted that shanks were not aligned to a local maximum in spiking power, but rather to a drop off or decline in spiking power that was coincident with an increase in gamma power and a nearby change in theta power. For example, a plateau in power across both the MCL and the EPL/SFL areas would not have produced this same result and would not have changed the estimated location of the MCL. Therefore, after alignment, spiking power of the extracellular recording peaked significantly at the MCL.

3.3.3 Physiological features of cells with relation to their distance from the MCL

Across all recordings and shanks with identifiable MCLs, we recorded from 117 cells in the MCL, 254 cells in the EPL/SFL, and 147 clusters in the IPL/GCL (Figure 3.4). Representative waveforms (Figure 3.4) show cells with high amplitude waveforms in the principal cell layers. Waveform amplitude distributions shared much overlap between areas, but mean amplitude was highest in the MCL (m = 300.77 μv, std = 153.02 μv). It was significantly higher than the mean waveform amplitude of cells in the EPL/SFL (m = 227.05 μv, std = 115.55 μv) ($Z = 4.63$, $p < 0.001$, $d = 0.57$) and in the IPL/GCL (m = 126.24 μv, std = 77.56 μv) ($z = 10.60$, $p < 0.001$, $d = 1.49$). Though it should be noted that while the means are significantly different, the two distributions share much overlap. Importantly, mean waveform amplitude in the IPL/GPL was significantly lower as compared to either other area (Table 3.2). Therefore, waveform amplitude is highest in the MCL, second highest in the EPL/SFL, and lowest in the GCL. Mean soma sizes for each area also decrease in a similar manner. MC somas are on average larger than most tufted cell (TC) subtypes in the EPL/SFL (Nagayama et al., 2010). The average GCs soma is smallest (Nagayama et al., 2014). As the amplitude of extracellular action potentials are known to be correlated with soma size (Gold et al., 2006), hypotheses of differences in amplitude as they relate to somas size corroborate the alignment results.

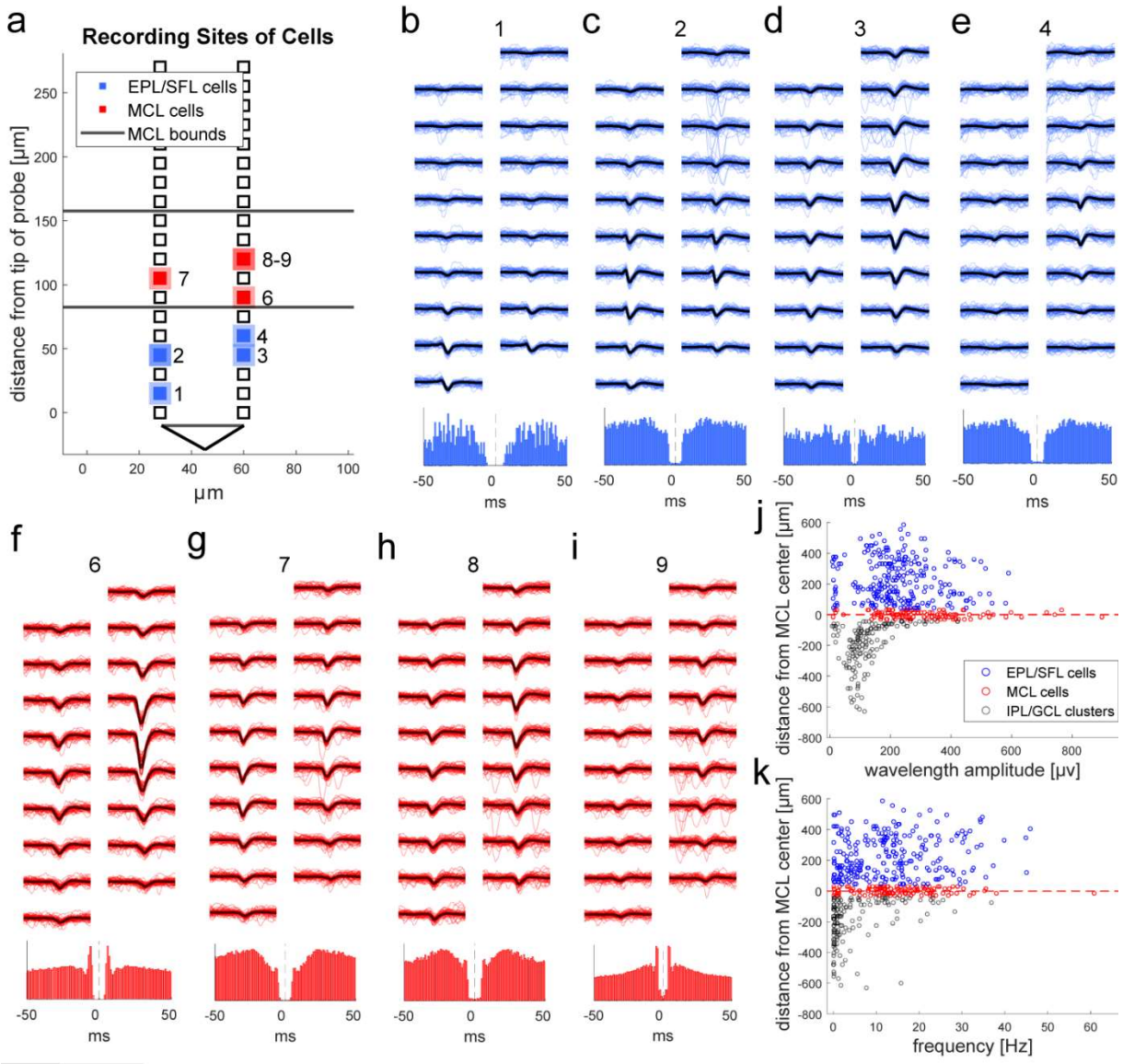

Figure 3.4: Individual cells and their physiological features relative to the estimated MCL. **a)** A schematic showing the location of MCL cells (red squares) and EPL/SFL cells (blue squares) across an example electrode array. The edges of the estimated MCL are indicated by gray lines. **b)** (top) The mean waveform (black line) of a single cell EPL/SFL example cell from the estimated ventral MCL across 9 rows of recording sites (18 sites total) is plotted on top of 50 randomly selected individual waveforms (blue). The number indicates the cell's location in the schematic **(a)** (bottom) The auto-correlogram of the cell is plotted (±50ms) showing the cell displays a refractory period. **c-e)** The same is plotted for three more example cells from the EPL/SFL and **(f-i)** four example cells from the MCL. **j)** A plot of each cell's distance from the center of the MCL center against its waveform amplitude shows amplitude declines moving toward the IPL/GCL, as displayed by the lower amplitude of IPL/GCL clusters (gray) as

compared to MCL cells (red) and EPL/SFL cells (blue). **k)** The same relationship can be observed for the average spiking rate of cells/clusters across the OB layers.

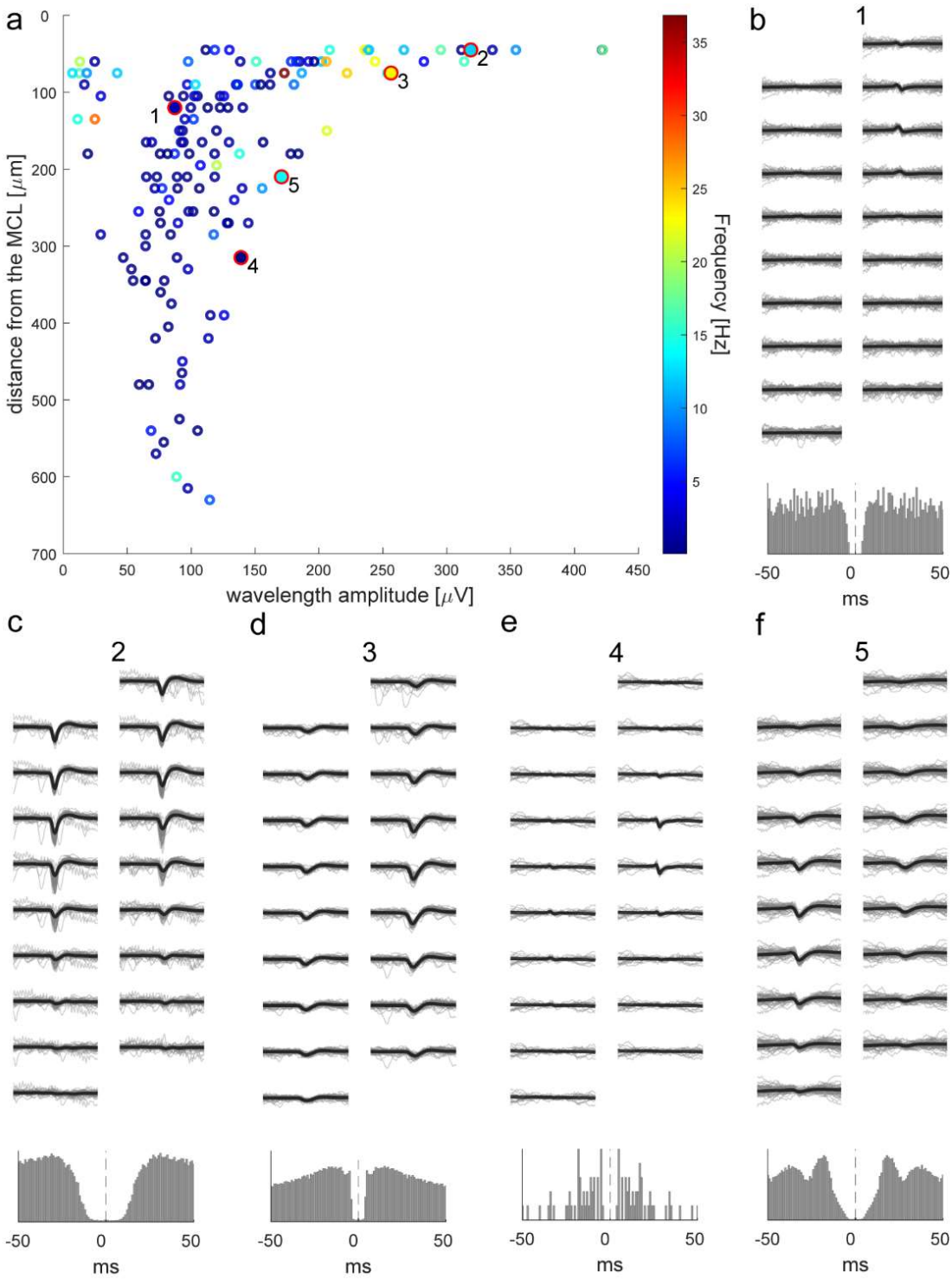

Figure 3.4.1: Clusters with waveforms in the IPL/GCL display low amplitude and low firing rates.

a) Distance from the MCL center (moving deeper into the bulb) is plotted against waveform amplitude for all IPL/GCL clusters, showing a decline of both waveform and amplitude for

clusters when moving deeper into the OB and away from the edge of the estimated MCL. The colormap indicates the firing rate of each cluster. **b)** (top) The mean waveform (black line) of an example cluster from the IPL/GCL area is plotted for 9 rows of recording sites (18 sites total). The mean waveforms are plotted over 50 randomly selected individual waveforms (gray). The number corresponds to the red highlighted cluster in (a). (bottom) The auto-correlogram of the cluster (±50ms) displays a refractory period. **c-f)** The same is plotted for additional IPL/GCL examples providing more examples of representative clusters. Even though IPL/GCL clusters are not referred to as cells, the study only includes clusters with physiologically feasible waveforms and refractory periods.

Spiking rates dropped moving away from MCL and deeper in to the IPL/GCL, but spiking rates did not change to the same degree in the direction of the superficial layers. The mean spiking frequency of the MCL (m = 15.44 Hz, std = 9.56) and EPL/SFL (m = 13.08 Hz, std =10.18) were significantly different from clusters in the IPL/GCL (m = 5.14 Hz, std = 7.33) as determined by rank-sum tests ($Z = 9.08$, $p < 0.001$, $d = 1.24$ and $Z = 8.90$, $p < 0.001$, $d = 0.86$ respectively). The MCL and EPL/IPL firing rates were significantly higher, but the effect size was small ($Z = 2.43$, $p = 0.02$, $d = 0.24$). Therefore, we found spiking rates as calculated across the entire recording session to be highest in the MCL, and close to rates observed in the EPL/SFL.

It is to be noted that clusters found in the IPL/GCL are not multi-unit activity clusters, but rather only good units from the IPL/GCL that exhibited physiologically feasible waveforms and refractory periods (Figure 3.4.1) were included in the analysis. In fact, it is likely that some clusters with high amplitude near the deep edge of the MCL (Figure 3.4.1A) are cells with somas located in the IPL or superficial GCL such as deep short axon cells. Despite this, given the difficulty in extracellular recordings *in vivo* of differentiating between axonal activity and interneurons when sorting low amplitude waveforms (Barry, 2015), we refer to IPL/GCL units as clusters instead of cells.

3.3.4 Plume Responsivity

We measured cellular responsivity to plume presentations to observe population responses to natural odor scenes at the cellular level. Cells were considered to respond significantly to plumes when their spiking activity during plume periods exceeded baseline expectations (see methods). No cells showed robust reliability to plume presentations across trials, but a subset of cells showed significant responses to plume presentations. In the MCL,

23.93% (28/117) of cells significantly responded and in the EPL/SFL 27.56% (70/254) of cells significantly responded (Figure 3.5). Of cells that significantly responded to plume presentations, responsivity scores were higher in MCs ($m = 0.31$, $std = 0.12$) than in the EPL/SFL ($m = 0.24$, $std = 0.15$) as determined by a rank-sum test ($Z = 5.31$, $p < 0.001$, $d = 0.53$). Though responsivity rates were comparable between MCL and EPL/SFL areas, MCs that exhibited significant responsivity did so more reliably across trials on average than EPL/SFL cells.

Although responsivity scores of the individual cells did not reach levels observed at the glomerular level in wide field imaging (Lewis et al., 2021), this does not refute the existence of individual cells capable of following odor concentration dynamics during natural scenes. One interpretation of the variable responses is that latent features of the plume dynamics make a subset of the cells more likely to respond. There may be latent features not present in every plume presentation at threshold level. Plume presentations are stochastic, so there may be timing or intensity cues that vary sufficiently between trials, recruiting subpopulations of responsive cells only during plume presentations in which these latent features reach threshold levels.

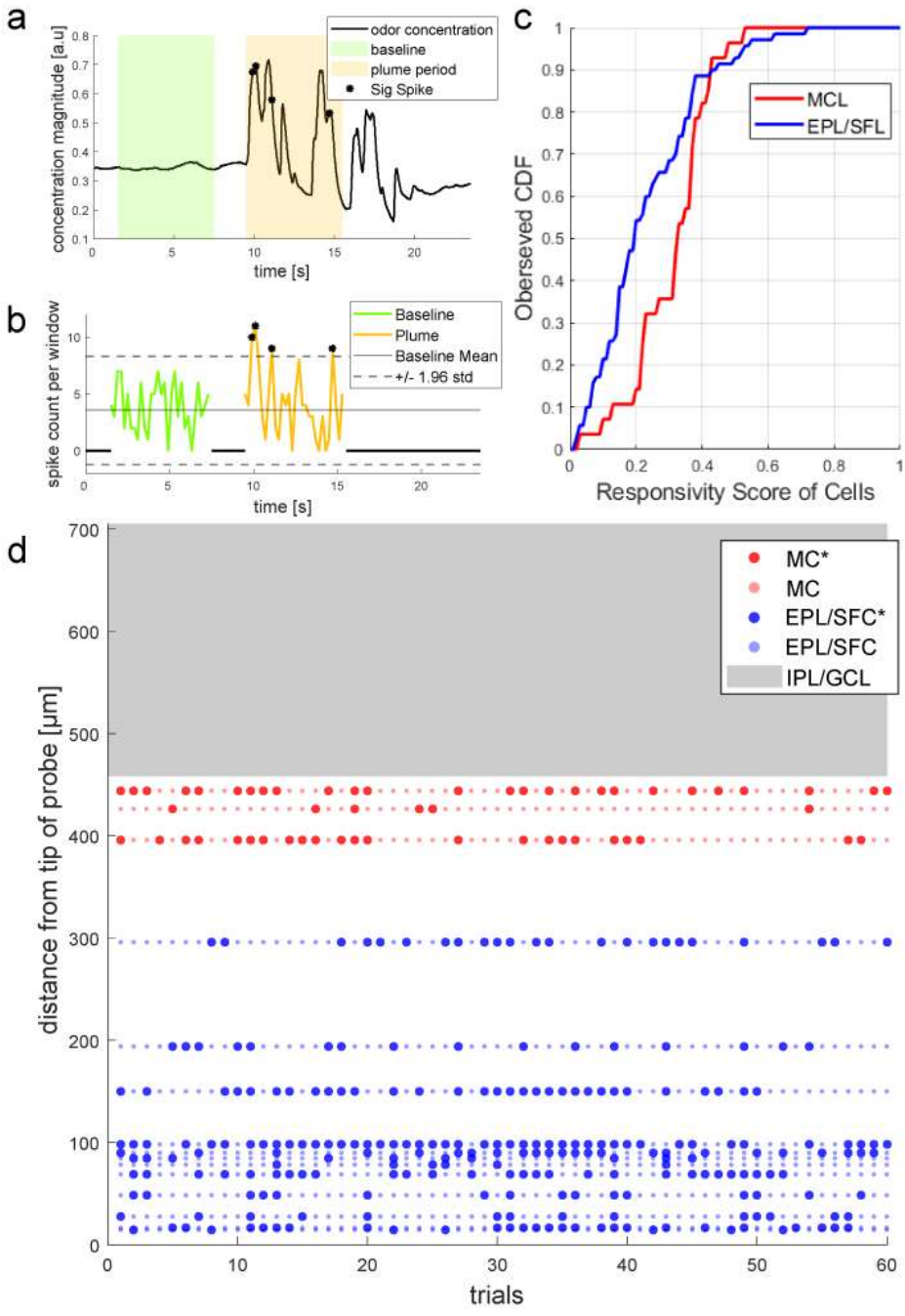

Figure 3.5: A subset of cells show significant responses to plumes.
a) The odor concentration from a single example trial is plotted, and the baseline period (green) and the plume period (orange) are both indicated. **b)** The response of cell to **(a)** that significantly responds to plume presentations is depicted. Spike counts binned at 200ms and ±1.96 std of the mean baseline spike count (dotted line) is indicated. Windows for which the cell significantly responds are plotted over the spike count **(b)** and the odor concentration **(a)**. **c)** The distribution of responsivity scores for MCL and EPL/SFL populations that exhibit significant responsivity to

the plume are plotted showing similar distribution in both areas. **d)** Cells with significant responsivity scores across the session are plotted from the MCL and EPL/SFL across all trials for a single session showing that the variability of responsivity is displayed in both early and late plume presentations of the session. Cells are plotted according to their position along the shank. The response to each trial is plotted as responding more than the baseline expectation during the trial (large circle) or within the expected baseline activity for the trial (small circle).

3.4 Discussion

In this study, a high-density electrophysiological approach using Neuropixels probes examined bulbar LFP and cellular responsivity to natural odor scenes.

Physiological characteristics of dipoles at different frequency ranges in the OB impact extracellular LFP. These characteristics can help determine the position of a recording site within the bulb relative to OB layers. Our hypothesis of theta, gamma, and spiking power changes near the MCL suggest that when moving towards the MCL from deeper layers, theta and gamma power should both decrease and spiking power should increase. Additionally, when moving from the MCL to more superficial layers, theta and gamma power should both rise, with gamma power rising close to the superficial edge of the MCL and theta power rising at some point before the GL. If this is the case, alignment should reveal a significant relationship between these three variables consistent with this anatomical hypothesis. Accordingly, after alignment, we found a significant positive correlation between theta and gamma oscillatory power and significant inverse correlations between spiking and gamma power and between spiking and theta power. It could be possible that these parameters have a similar relationship elsewhere in the bulb and that the use of these parameters would lead to estimations of the MCL in areas elsewhere in the bulb. Importantly, in a full shank recording traversing the dorsal/ventral axis of the OB, we find only two occurrences within the OB where spiking rises from negligible levels and both gamma and theta power drop. Both occurrences are in a position feasible for the location of the MCL. Thus, we found alignment using theta, gamma, and spiking LFP parameters did reflect expectations given known bulbar dipoles and physiological features of deep OB cells. Without ground truth from anatomical labeling, it is impossible to assess the error of our estimates, but convergent evidence seen in the relationship between these three features

establishes that our alignment results are consistent with anatomy-based hypotheses. Thus, using coincident features of relative changes in theta, gamma, and spiking LFP power across the depth of the OB could help future studies when estimating layer locations within high-density extracellular recordings.

Our alignment showed variability in the exact point at which spiking power rose and gamma and theta power declined relative to the MCL. A portion of this variability is likely due to inter-mouse variation in layer width and to estimation error, but some changes in the alignment protocol may help reduce this noise in future studies. First, differences in the probe's angle relative to the MCL layer could make it harder to capture the polarity reversal. It is known that polarity reversals are best captured when probes are aligned perpendicular to the layer, or in line with the columnar organization of the cells (Kay, 2015). Thus, ensuring that probes are inserted tangentially to the cortical surface could help to capture polarity reversals more efficiently, and remove some of the variability seen in power differentials on either side of the reversal. In fact, some of the shanks did not show a true local minima near the MCL, despite exhibiting a noticeable reversal of polarity in the LFP amplitude over time (dorsal MCL, Figure 3.2.1 F-G). Another way to reduce noise would be to change the time over which power was calculated. We used spontaneously evoked activity because granule spiking is hypothesized to be lowest and because gamma oscillations that are odor-evoked result in polarity reversal located slightly more superficial than other types of stimulation such as antidromic excitation via the LOT or centrifugal feedback. This is thought to be due to the fact that odor input results in a sink in the LFP at the GL in addition to the EPL since apical dendrites are excited by glomerular input when stimulated by odor (Rojas-Líbano & Kay, 2008). Even using spontaneous activity though, extracting only moments in which the gamma oscillations are present and the polarity reversal is

observed at the MCL would likely make the local minima in the power plot more clear. In fact, most current source density (CSD) analyses compute power across average activity that has been aligned to a particular stimulus or event. Our choice of analyzing over seconds of spontaneously evoked activity instead of averaged activity aligned to specific LFP events may have contributed variability in power changes around the MCL. Future studies could align to LFP events by calculating phase of the CWT (Roux et al., 2007) and aligning to specific cycles (Fourcaud-Trocmé et al., 2014). However, the robustness of our approach is well-demonstrated by its success despite such precise and hand-tuned alignment.

In addition to changes in the analysis procedure, pairing relative changes in cell properties with relative changes in LFP power could aid estimates. Although this study did not assign putative cells types outside of the MCL, in future analyses, the use of cell-type specific physiological features such as odor-evoked firing rate or odor-evoked response latency could be paired with LFP features for strong layer estimates. Tufted cells (TCs), whose somas are located in the EPL (Imamura et al., 2020a), show shorter response latencies and have higher odor-evoked firing rates on average as compared MCs (Burton & Urban, 2014). Therefore, using coincident measures of theta, gamma, and spiking power in combination with known cell properties may refine putative cell type and layer estimation in future extracellular recordings. Taken together, looking for changes in LFP power and physiological features of cells could provide tools to aid alignment protocols and alignment software, such as that designed to be compatible with Neuropixel recordings (). The alignment procedure here is not suggested as an error free estimate of layer location, but rather a tool that could be used and improved upon to lead to reliable layer estimates in future studies.

In terms of examining cellular level responses to natural odor scenes, this study establishes Neuropixels as an effective high-density electrophysiological technique of recording OB activity in mice responding to natural odor scenes. Examination of cellular responsivity showed a lack of highly reliable responses across plume presentations. Responsivity was not observed at the same magnitude as seen previously in wide-field recordings at the glomerular level in response to the same olfactory stimulus setup (Lewis et al., 2021). One possible interpretation of this could be that the widefield technique of Lewis et al., 2021 recorded from larger areas across the bulbar surface and in turn sampled much larger populations of principal cells. Another biasing factor is that cells that are more active will fluoresce more (controlling for how well a cell expresses the calcium indicator in question). Principal cells are known to have large changes in firing rate (some cells around ten-fold) in response to odor (Ly et al., 2021). Therefore, the wide-field recordings sampled larger areas of OB and within that area were biased to capture dendritic clusters with high activity levels, such as that seen in odor-evoked responses. Therefore, the electrophysiological recordings may have captured fewer MTCs directly innervated by responsive glomeruli. Using an odor panel in future recordings could screen for responsive MTCs within range of the electrode arrays. This is a common method used in olfactory studies. In this experiment, instead of an odor panel, a single odor mixture optimized for dorsal OB activation was used as the study originally planned to capture largely dorsal activity. In addition to ethanol, the odor mixture included five odorants that have been observed to have strong and differential activation patterns across the dorsal surface. During Neuropixels data collection, the difference between the amplitude of spiking activity in dorsal and ventral recordings resulted in 7 of 10 recordings targeting ventral OB. Therefore, despite capturing many individual cells, the recordings may not have captured many cells directly innervated by

responsive glomeruli. In fact, glomerular odor coding is observed to be sparse, and at threshold levels of odor concentration encoding is often even uniglomerular in nature (Burton et al., 2022). Future studies could avoid this limitation simply by using an odor panel of short odor pulses prior to beginning the experiment. Another less brute-force solution could be to make targeted recordings, where glomerular maps obtained in wide field imaging prior to recording are used to target probe insertion near responsive glomeruli.

As for the cells that were captured in our study and that displayed significant responsivity to the plume presentations, one explanation for their varied reliability (lower responsivity rates) could be that the cells were responding to latent features of the plume dynamics that were not present at a detectable level in every plume presentation. Plumes are stochastic, and as a result timing and intensity cues of the dynamics can vary between trials. If cells are tuned to sparse dynamic features, different subpopulations of cells could be recruited only when those latent features are present at sufficient threshold levels. For example, a feature such as a long blank between whiffs or a particularly high concentration whiff could both be latent features in the odor concentration dynamics of our stimulus. Both of these latent features could hypothetically arise as a product of responses already observed in the OB in previous studies. For example, in the case of the pause of sufficient duration, two previously observed responses in the OB could contribute to responses that are dependent on blank length during plume presentations. Both attenuated responses to repeated odor pulses (Storace & Cohen, 2021) and inhibition leading to rebound responses after odor exposure (Cavarretta et al., 2018) are known phenomena of odor encoding in principal OB cells. In natural odor scenes repeated odor whiffs and long odor whiffs may lead to attenuation and inhibition. It is not unreasonable to hypothesize then that a sufficient blank duration between whiffs may reset attenuation leading to increased firing rates or relieve

inhibition triggering rebound responses when the odor stimulus transitions from “on” to “off”. Taken together, these responses would then functionality allow for the encoding of blank duration, thus playing a role in the encoding of features in natural odor scenes. Therefore, perhaps a subset of cells may only respond on plume presentations in which blanks of a sufficient duration occur.

In the case of the other latent feature example, an odor whiff above a concentration threshold of relatively high magnitude, it is possible that the concentration dependent recruitment of glomerular ensembles could result in concentration threshold detection at the level of principal cells. In the OB, glomerular ensembles encode odor identity (Belluscio & Katz, 2001), and increases in odor identity results in the recruitment of additional members to the ensemble. In this way, there are some glomeruli that will only respond once the odor concentration reaches a certain threshold. Therefore, it is possible that during natural odor scenes, there may be principal cells that would only respond to plumes in which odor concentration reached a certain threshold, as the glomeruli that innervate them would not respond during odor exposure across weaker concentration levels.

Some of these feature-dependent responses create hypotheses that could be easily tested in future studies. For example, one way to examine possible latent feature dependent responses would be to use a reverse correlation analysis to examine what the plume activity looks like when the recorded cell spikes at a high rate. For blank responding MTCs, stimulus measured prior to a significant response should be low on average. For principal cells innervating by glomeruli that are only recruited to an ensemble at high concentration levels, two requirements should be met. At the individual cells level, a reverse odor correlation analysis must display higher average odor concentration levels than when the cell isn’t significantly responding.

Second, across these cells that are truly recruited in a concentration threshold dependent manner, the sparser the response, the higher the odor concentration should be that elicits the response. In this way, encoding mechanisms already observed in the bulb could contribute to feature-dependent responses, such that cells responding to sparser features of plume dynamics may only respond when these features arise leading to variable responsivity across plume presentations. Although latent feature coding may have contributed to some variability, we presume it unlikely that this is the main reason for the variable responses, as this would imply that cells tuned to sparse features are more common than cells tuned to common features of plume dynamics. Thus, it is important that future studies use methods to target MTCs directly innervating responsive glomeruli in large-scale extracellular recordings.

Our recordings demonstrate that high-density Neuropixels recordings are an efficient way to capture populations of OB activity at the cellular level. Additionally, examining relative changes in LFP across the bulb could be a tool to help future studies with layer and cell-type estimates. As the feature space of plume dynamics utilized by mice navigating plumes is still not yet fully understood, recording large populations of OB cells while mice sample complex and naturalistic odor dynamics is an important method for understanding odor encoding in the first olfactory relay of the brain.

Concluding Remarks

As mice navigate olfactory environments, they must interpret the intermittent and stochastic cues of olfactory plumes. Spatiotemporal patterns of odor concentration within plumes convey information regarding odor sources and their locations. The degree to which the OB responds to dynamic cues embedded in complex plumes has been hard to determine due to the difficulty of recording naturalistic plumes without disrupting plume dynamics. In the work presented in this dissertation, a novel approach developed by the Gire lab utilizing small, passive ethanol sensors allowed for the measurement of odor concentration across stochastic plumes. Simultaneous measurement of OB activity and plume concentration dynamics allowed for opportunities to examine OB responses to natural odor scenes using both wide-field imaging and Neuropixels high-density electrophysiology. Using these methods we were able to capture MTC activity across the bulbar surface with optical imaging and LFP and cell activity across layers of the OB with electrophysiology. Thus, this dissertation has attempted to understand some of the natural processing dynamics of the first olfactory relay in response to plume dynamics.

Previous research has studied isolated features of natural odor scenes and found the OB responds to some known dynamic features of plumes. Principal cells exhibit responses dependent on concentration changes. The subthreshold membrane activity of individual MTCs in anesthetized mice can significantly follow odor fluctuating at a frequency of up to 20 Hz (Dasgupta et al., 2022). As plumes are experienced by olfactory searchers as whiffs, this ability to capture fast fluctuations suggests the OB may resolve whiffs arriving at a similar timescale during plume encounters. Thus, the OB may be able to interpret some of the finer features of the spatiotemporal dynamics of plumes. Additionally, when odor pulses are delivered consecutively at two different concentrations, subpopulations of MTCs are able to detect the concentration

change, encode the direction of change, or encode some measure of change magnitude (Parabucki et al., 2019). A subset of cells even encoded a combination of these features. Therefore, individual OB principal neurons exhibit sensitivity to odor concentration changes at both the sub- and supra- threshold level. Whether these responses are observed when the mouse samples the full complexity of natural odor scenes, plumes, has yet to be determined. It is unknown to what extent principal cells respond to the concentration dynamics across plume encounters at the individual level, though concentration tracking or plume feature dependent responses may arise as a result of these or other unknown concentration dependent responses. Capturing sufficiently large populations of OB cells responding to plume dynamics will help determine ways in which OB cells encode features in natural odor environments, either independently or at the population level.

Understanding how the brain interprets the environment requires understanding natural responses of the brain to ethologically relevant sensory environments. Here we provide wide-field evidence plume dynamics structure information in the first olfactory relay at the population level. Additionally, we establish a methodology for exploring cellular-level responses to plume dynamics using high-density electrophysiological Neuropixels recordings. Continuing to incorporate more naturalistic, dynamic cues into the study of olfaction will help determine how mice efficiently locate odor sources despite the complexity of plume dynamics.

Table 3.1

	Mean	Standard deviation	*n*	Combination	rank-sum score	*p*-value	cohen's *d*
Theta Power							
EPL/SFL	0.28	0.19	32	EPL/SFL & IPL/GCL	4.24	<0.001	1.39
MCL	0.37	0.31	34	MCL & EPL/SFL	0.67	0.5006	*ns
IPL/GCL	0.62	0.29	31	MCL & IPL/GCL	3.26	<0.001	0.84
			31				
Gamma Power							
EPL/SFL	0.23	0.22	32	EPL/SFL & IPL/GCL	5.79	<0.001	2.27
MCL	0.17	0.20	34	MCL & EPL/SFL	1.48	0.1384	*ns
IPL/GCL	0.66	0.15	31	MCL & IPL/GCL	6.17	<0.001	2.74
			31				
Spiking Power							
EPL/SFL	0.52	0.20	32	EPL/SFL & IPL/GCL	5.79	<0.001	2.27
MCL	0.77	0.20	34	MCL & EPL/SFL	6.11	<0.001	2.52
IPL/GCL	0.22	0.16	31	MCL & IPL/GCL	3.76	<0.001	0.60

Table 3.1 Comparing theta, gamma, and spiking power relative to the MCL.

Significant differences were observed on either side of the MCL for all frequency bands evaluated. Significant differences were also observed between the MCL and the IPL/GCL for all frequency bands, but only spiking power showed a significant difference between the MCL and the EPL/SFL, suggesting power changes were steeper on the deeper side of the MCL. To test for significant changes in power, a Wilcoxon's rank-sum test was used for the average power as calculated within 240 m of either side of the MCL. If there were less than 240 m of electrode array, available sites were used to calculate the mean. If there were no electrode arrays on one side of the MCL than no measure for that side of the electrode array was included in the rank-sum analysis, thus the number of electrode arrays used to calculate the mean across the layers for each power are indicated (*n)*. Effect sizes were computed using Cohen's *d*.

Table 3.2

	Mean	Standard deviation	*n*	Combination	rank-sum score	p-value	cohen's *d*
Mean waveform amplitude							
EPL/SFL	227.05	115.55	254	EPL/SFL & IPL/GCL	9.66	p<0.001	0.98
MCL	300.77	153.02	117	MCL & EPL/SFL	4.63	p<0.001	0.57
IPL/GCL	126.24	77.56	147	MCL & IPL/GCL	10.60	p<0.001	1.49
Mean spiking frequency							
EPL/SFL	13.08	10.18	254	EPL/SFL & IPL/GCL	8.90	p<0.001	0.86
MCL	15.44	9.56	117	MCL & EPL/SFL	2.43	0.015	0.24
IPL/GCL	5.14	7.22	147	MCL & IPL/GCL	9.08	p<0.001	1.24

Table 3.2 Comparing physiological features relative to the MCL.

Significant changes both waveform amplitude and mean spiking rate were between indicated areas. Difference in physiological features between areas were calculated using a Wilcoxon rank-sum test, and effect size was calculated using Cohen's *d.* Cells or clusters located on an electrode array that did not have an identifiable MCL were excluded from the analysis.

References

Ache, B. W., Hein, A. M., Bobkov, Y. v., & Principe, J. C. (2016). Smelling Time: A Neural Basis for Olfactory Scene Analysis. In *Trends in Neurosciences* (Vol. 39, Issue 10, pp. 649–655). Elsevier Ltd. https://doi.org/10.1016/j.tins.2016.08.002

Ackels, T., Erskine, A., Dasgupta, D., Marin, A. C., Warner, T. P. A., Tootoonian, S., Fukunaga, I., Harris, J. J., & Schaefer, A. T. (2021). Fast odour dynamics are encoded in the olfactory system and guide behaviour. *Nature*, *593*(7860), 558–563. https://doi.org/10.1038/s41586-021-03514-2

Ackels, T., Jordan, R., Schaefer, A. T., & Fukunaga, I. (2020). Respiration-Locking of Olfactory Receptor and Projection Neurons in the Mouse Olfactory Bulb and Its Modulation by Brain State. *Frontiers in Cellular Neuroscience*, *14*. https://doi.org/10.3389/fncel.2020.00220

Adam, Y., Livneh, Y., Miyamichi, K., Groysman, M., Luo, L., & Mizrahi, A. (2014). Functional transformations of odor inputs in the mouse olfactory bulb. *Frontiers in Neural Circuits*, *8*. https://doi.org/10.3389/fncir.2014.00129

Arneodo, E. M., Penikis, K. B., Rabinowitz, N., Licata, A., Cichy, A., Zhang, J., Bozza, T., & Rinberg, D. (2018). Stimulus dependent diversity and stereotypy in the output of an olfactory functional unit. *Nature Communications*, *9*(1). https://doi.org/10.1038/s41467-018-03837-1

Atema, J. (1996). Eddy Chemotaxis and Odor Landscapes: Exploration and Nature With Animal Sensors. *Biological Bulletin*.

Baker, K. L., Dickinson, M., Findley, T. M., Gire, D. H., Louis, M., Suver, M. P., Verhagen, J. v., Nagel, K. I., & Smear, M. C. (2018). Algorithms for olfactory search across species. *Journal of Neuroscience*, *38*(44), 9383–9389. https://doi.org/10.1523/JNEUROSCI.1668-18.2018

Baker, T. C., Willis, M. A., Haynes, F., & Phelan, P. L. (1985). A pulsed cloud of sex pheromone elicits upwind flight in male moths. In *Phys~ologzcal Entomology* (Vol. 10).

Banerjee, A., Marbach, F., Anselmi, F., Koh, M. S., Davis, M. B., Garcia da Silva, P., Delevich, K., Oyibo, H. K., Gupta, P., Li, B., & Albeanu, D. F. (2015). An Interglomerular Circuit Gates Glomerular Output and Implements Gain Control in the Mouse Olfactory Bulb. *Neuron*, *87*(1), 193–207. https://doi.org/10.1016/j.neuron.2015.06.019

Barry, J. M. (2015). Axonal Activity in vivo: Technical considerations and implications for the exploration of neural circuits in freely moving animals. In *Frontiers in Neuroscience* (Vol. 9, Issue APR). Frontiers Research Foundation. https://doi.org/10.3389/fnins.2015.00153

Belluscio, L., & Katz, L. C. (2001). *Symmetry, Stereotypy, and Topography of Odorant Representations in Mouse Olfactory Bulbs*.

Bhattacharjee, A. S., Konakamchi, S., Turaev, D., Vincis, R., Nunes, D., Dingankar, A. A., Spors, H., Carleton, A., Kuner, T., & Abraham, N. M. (2019). Similarity and Strength of Glomerular Odor Representations Define a Neural Metric of Sniff-Invariant Discrimination Time. *Cell Reports*, *28*(11), 2966-2978.e5. https://doi.org/10.1016/j.celrep.2019.08.015

Boie, S. D., Connor, E. G., McHugh, M., Nagel, K. I., Ermentrout, G. B., Crimaldi, J. P., & Victor, J. D. (2018). Information-theoretic analysis of realistic odor plumes: What cues are useful for determining location? *PLoS Computational Biology*, *14*(7). https://doi.org/10.1371/journal.pcbi.1006275

Bolding, K. A., & Franks, K. M. (2018). Recurrent cortical circuits implement concentration-invariant odor coding. *Science*, *361*(6407). https://doi.org/10.1126/science.aat6904

Boyd, A. M., Sturgill, J. F., Poo, C., & Isaacson, J. S. (2012). Cortical Feedback Control of Olfactory Bulb Circuits. *Neuron*, *76*(6), 1161–1174. https://doi.org/10.1016/j.neuron.2012.10.020

Buck, L. B. (2004). *Olfactory Receptors and Odor Coding in Mammals*. https://doi.org/10.1301/nr.2004.nov.S184

Burton, S. D. (2017). *Inhibitory circuits of the mammalian main olfactory bulb*. https://doi.org/10.1152/jn.00109.2017.-Synaptic

Burton, S. D., Brown, A., Eiting, T. P., Youngstrom, I. A., Rust, T. C., Schmuker, M., & Wachowiak, M. (2022). Mapping odorant sensitivities reveals a sparse but structured representation of olfactory chemical space by sensory input to the mouse olfactory bulb. *ELife*, *11*. https://doi.org/10.7554/eLife.80470

Burton, S. D., & Urban, N. N. (2014). Greater excitability and firing irregularity of tufted cells underlies distinct afferent-evoked activity of olfactory bulb mitral and tufted cells. *Journal of Physiology*, *592*(10), 2097–2118. https://doi.org/10.1113/jphysiol.2013.269886

Burton, S. D., & Urban, N. N. (2021). Cell and circuit origins of fast network oscillations in the mammalian main olfactory bulb. *ELife*, *10*. https://doi.org/10.7554/eLife.74213

Cang, J., & Isaacson, J. S. (2003). In Vivo Whole-Cell Recording of Odor-Evoked Synaptic Transmission in the Rat Olfactory Bulb. *The Journal of Neuroscience*, *23*(10), 4108–4116. https://doi.org/10.1523/JNEUROSCI.23-10-04108.2003

Carey, R. M., & Wachowiak, M. (2011). Effect of sniffing on the temporal structure of mitral/tufted cell output from the olfactory bulb. *Journal of Neuroscience*, *31*(29), 10615–10626. https://doi.org/10.1523/JNEUROSCI.1805-11.2011

Cartas-Rosado, R., Becerra-Luna, B., Martínez-Memije, R., Infante-Vázquez, Ó., Lerma, C., Pérez-Grovas, H., & Rodríguez-Chagolla, J. M. (2020). Continuous wavelet transform based processing for estimating the power spectrum content of heart rate variability during hemodiafiltration. *Biomedical Signal Processing and Control*, *62*. https://doi.org/10.1016/j.bspc.2020.102031

Cavarretta, F., Burton, S. D., Igarashi, K. M., Shepherd, G. M., Hines, M. L., & Migliore, M. (2018). Parallel odor processing by mitral and middle tufted cells in the olfactory bulb. *Scientific Reports*, *8*(1). https://doi.org/10.1038/s41598-018-25740-x

Celani, A., Villermaux, E., & Vergassola, M. (2014). Odor landscapes in turbulent environments. *Physical Review X*, *4*(4). https://doi.org/10.1103/PhysRevX.4.041015

Chae, H., Banerjee, A., & Albeanu, D. F. (2020). A non-canonical feedforward pathway for computing odor identity. *BioRxiv*. https://doi.org/10.1101/2020.09.28.317248

Chen, Z., & Padmanabhan, K. (2020). Top-Down Control of Inhibitory Granule Cells in the Main Olfactory Bulb Reshapes Neural Dynamics Giving Rise to a Diversity of Computations. *Frontiers in Computational Neuroscience*, *14*. https://doi.org/10.3389/fncom.2020.00059

Chockanathan, U., Crosier, E. J. W., Waddle, S., Lyman, E., Gerkin, R. C., & Padmanabhan, K. (2021). Changes in pairwise correlations during running reshape global network state in the main olfactory bulb. *Journal of Neurophysiology*, *125*(5), 1612–1623. https://doi.org/10.1152/jn.00464.2020

Cleland, T. A., & Borthakur, A. (2020). A Systematic Framework for Olfactory Bulb Signal Transformations. *Frontiers in Computational Neuroscience*, *14*. https://doi.org/10.3389/fncom.2020.579143

Connor, E. G., McHugh, M. K., & Crimaldi, J. P. (2018). Quantification of airborne odor plumes using planar laser-induced fluorescence. *Experiments in Fluids*, *59*(9). https://doi.org/10.1007/s00348-018-2591-3

Crimaldi, J. P., & Koseff, J. R. (2001). High-resolution measurements of the spatial and temporal scalar structure of a turbulent plume. In *Experiments in Fluids* (Vol. 31). Springer-Verlag.

Dana, H., Chen, T. W., Hu, A., Shields, B. C., Guo, C., Looger, L. L., Kim, D. S., & Svoboda, K. (2014). Thy1-GCaMP6 transgenic mice for neuronal population imaging in vivo. *PLoS ONE*, *9*(9). https://doi.org/10.1371/journal.pone.0108697

Dasgupta, D., Warner, T. P. A., Erskine, A., & Schaefer, A. T. (2022). Coupling of Mouse Olfactory Bulb Projection Neurons to Fluctuating Odor Pulses. *The Journal of Neuroscience : The Official Journal of the Society for Neuroscience*, *42*(21), 4278–4296. https://doi.org/10.1523/JNEUROSCI.1422-21.2022

Davison, I. G., & Katz, L. C. (2007). Sparse and selective odor coding by mitral/tufted neurons in the main olfactory bulb. *Journal of Neuroscience*, *27*(8), 2091–2101. https://doi.org/10.1523/JNEUROSCI.3779-06.2007

de Jan, D. saint, Hirnet, D., Westbrook, G. L., & Charpak, S. (2009). External tufted cells drive the output of olfactory bulb glomeruli. *Journal of Neuroscience*, *29*(7), 2043–2052. https://doi.org/10.1523/JNEUROSCI.5317-08.2009

Demir, M., Kadakia, N., Anderson, H. D., Clark, D. A., & Emonet, T. (2020). Walking drosophila navigate complex plumes using stochastic decisions biased by the timing of odor encounters. *ELife*, *9*, 1–31. https://doi.org/10.7554/eLife.57524

Dhawale, A. K., Hagiwara, A., Bhalla, U. S., Murthy, V. N., & Albeanu, D. F. (2010). Non-redundant odor coding by sister mitral cells revealed by light addressable glomeruli in the mouse. *Nature Neuroscience*, *13*(11), 1404–1412. https://doi.org/10.1038/nn.2673

Eiting, T. P., & Wachowiak, M. (2020). Differential impacts of repeated sampling on odor representations by genetically-defined mitral and tufted cell subpopulations in the mouse olfactory bulb. *Journal of Neuroscience*, *40*(32), 6177–6188. https://doi.org/10.1523/JNEUROSCI.0258-20.2020

Ennis, M., Hamilton, K. A., & Hayar, A. (2007). Neurochemistry of the Main Olfactory System. In *Handbook of Neurochemistry and Molecular Neurobiolog* (pp. 137–204).

Esquivelzeta Rabell, J., Mutlu, K., Noutel, J., Martin del Olmo, P., & Haesler, S. (2017). Spontaneous Rapid Odor Source Localization Behavior Requires Interhemispheric Communication. *Current Biology*, *27*(10), 1542-1548.e4. https://doi.org/10.1016/j.cub.2017.04.027

Eyre, M. D., Antal, M., & Nusser, Z. (2008). Distinct deep short-axon cell subtypes of the main olfactory bulb provide novel intrabulbar and extrabulbar gabaergic connections. *Journal of Neuroscience*, *28*(33), 8217–8229. https://doi.org/10.1523/JNEUROSCI.2490-08.2008

Findley, T. M., Wyrick, D. G., Cramer, J. L., Brown, M. A., Holcomb, B., Attey, R., Yeh, D., Monasevitch, E., Nouboussi, N., Cullen, I., Songco, J. O., King, J. F., Ahmadian, Y., & Smear, M. C. (2021). Sniff-synchronized, gradient-guided olfactory search by freely moving mice. *ELife*, *10*. https://doi.org/10.7554/eLife.58523

Fletcher, M. L., Masurkar, A. v., Xing, J., Imamura, F., Xiong, W., Nagayama, S., Mutoh, H., Greer, C. A., Knöpfel, T., & Chen, W. R. (2009). Optical imaging of postsynaptic odor representation in the glomerular layer of the mouse olfactory bulb. *Journal of Neurophysiology*, *102*(2), 817–830. https://doi.org/10.1152/jn.00020.2009

Fourcaud-Trocmé, N., Courtiol, E., & Buonviso, N. (2014). Two distinct olfactory bulb sublaminar networks involved in gamma and beta oscillation generation: A CSD study in the anesthetized rat. *Frontiers in Neural Circuits*, *8*(JULY). https://doi.org/10.3389/fncir.2014.00088

Fried, H. U., Fuss, S. H., & Korsching, S. I. (2002). *Selective imaging of presynaptic activity in the mouse olfactory bulb shows concentration and structure dependence of odor responses in identified glomeruli*. https://www.pnas.org

Fukunaga, I., Berning, M., Kollo, M., Schmaltz, A., & Schaefer, A. T. (2012). Two Distinct Channels of Olfactory Bulb Output. *Neuron*, *75*(2), 320–329. https://doi.org/10.1016/j.neuron.2012.05.017

Fukunaga, I., Herb, J. T., Kollo, M., Boyden, E. S., & Schaefer, A. T. (2014). Independent control of gamma and theta activity by distinct interneuron networks in the olfactory bulb. *Nature Neuroscience*, *17*(9), 1208–1216. https://doi.org/10.1038/nn.3760

Gaillard, I., Rouquier, S., Pin, J. P., Mollard, P., Richard, S., Barnabé, C., Demaille, J., & Giorgi, D. (2002). A single olfactory receptor specifically binds a set of odorant molecules. *European Journal of Neuroscience*, *15*(3), 409–418. https://doi.org/10.1046/j.0953-816x.2001.01871.x

Gardiner, J. M., & Atema, J. (2010). The function of bilateral odor arrival time differences in olfactory orientation of sharks. *Current Biology*, *20*(13), 1187–1191. https://doi.org/10.1016/j.cub.2010.04.053

Geffen, M. N., Broome, B. M., Laurent, G., & Meister, M. (2009). Neural Encoding of Rapidly Fluctuating Odors. *Neuron*, *61*(4), 570–586. https://doi.org/10.1016/j.neuron.2009.01.021

Geramita, M., & Urban, N. N. (2017). Differences in glomerular-layer-mediated feedforward inhibition onto mitral and tufted cells lead to distinct modes of intensity coding. *Journal of Neuroscience*, *37*(6), 1428–1438. https://doi.org/10.1523/JNEUROSCI.2245-16.2016

Gervais, R., Buonviso, N., Martin, C., & Ravel, N. (2007). What do electrophysiological studies tell us about processing at the olfactory bulb level? *Journal of Physiology Paris*, *101*(1–3), 40–45. https://doi.org/10.1016/j.jphysparis.2007.10.006

Gire, D. H., Franks, K. M., Zak, J. D., Tanaka, K. F., Whitesell, J. D., Mulligan, A. A., Hen, R., & Schoppa, N. E. (2012). Mitral cells in the olfactory bulb are mainly excited through a multistep signaling path. *Journal of Neuroscience*, *32*(9), 2964–2975. https://doi.org/10.1523/JNEUROSCI.5580-11.2012

Gire, D. H., Kapoor, V., Arrighi-Allisan, A., Seminara, A., & Murthy, V. N. (2016). Mice develop efficient strategies for foraging and navigation using complex natural stimuli. *Current Biology*, *26*(10), 1261–1273. https://doi.org/10.1016/j.cub.2016.03.040

Gire, D. H., & Schoppa, N. E. (2009). Control of on/off glomerular signaling by a local GABAergic microcircuit in the olfactory bulb. *Journal of Neuroscience*, *29*(43), 13454–13464. https://doi.org/10.1523/JNEUROSCI.2368-09.2009

Gold, C., Henze, D. A., Koch, C., & Buzsáki, G. (2006). On the origin of the extracellular action potential waveform: A modeling study. *Journal of Neurophysiology*, *95*(5), 3113–3128. https://doi.org/10.1152/jn.00979.2005

Greer, C. A., Whitman, M. C., Rela, L., Imamura, F., & Rodriguez Gil, D. (2008). Architecture of the Olfactory Bulb. *The Senses: A Comprehensive Reference*, *4*, 623–640. https://doi.org/10.1016/B978-012370880-9.00117-1

Gumaste, A., Coronas-Samano, G., Hengenius, J., Axman, R., Connor, E. G., Baker, K. L., Ermentrout, B., Crimaldi, J. P., & Verhagen, J. v. (2020). A comparison between mouse, in silico, and robot odor plume navigation reveals advantages of mouse odor tracking. *ENeuro*, *7*(1). https://doi.org/10.1523/ENEURO.0212-19.2019

Gupta, P., Albeanu, D. F., & Bhalla, U. S. (2015). Olfactory bulb coding of odors, mixtures and sniffs is a linear sum of odor time profiles. *Nature Neuroscience*, *18*(2), 272–281. https://doi.org/10.1038/nn.3913

Hamilton, K. A., Heinbockel, T., Ennis, M., Szabó, G., Erdélyi, F., & Hayar, A. (2005). Properties of external plexiform layer interneurons in mouse olfactory bulb slices. *Neuroscience*, *133*(3), 819–829. https://doi.org/10.1016/j.neuroscience.2005.03.008

Häusser, M., Spruston, N., & Stuart, G. J. (2000). Diversity and Dynamics of Dendritic Signaling. *Science*, *290*(5492), 739–744. https://doi.org/10.1126/science.290.5492.739

Hayar, A., Karnup, S., Ennis, M., & Shipley, M. T. (2004). External tufted cells: A major excitatory element that coordinates glomerular activity. *Journal of Neuroscience*, *24*(30), 6676–6685. https://doi.org/10.1523/JNEUROSCI.1367-04.2004

Homma, R., Kovalchuk, Y., Konnerth, A., Cohen, L. B., & Garaschuk, O. (2013). In vivo functional properties of juxtaglomerular neurons in the mouse olfactory bulb. *Frontiers in Neural Circuits*, *FEBRUARY 2013*. https://doi.org/10.3389/fncir.2013.00023

Hopfield, J. J. (1991). *Olfactory computation and object perception (neural network/learning/sensory systems)* (Vol. 88). https://www.pnas.org

Hu, B., & Tu, Y. (2014). Behaviors and Strategies of Bacterial Navigation in Chemical and Nonchemical Gradients. *PLoS Comput Biol*, *10*(6), 1003672. https://doi.org/10.1371/journal.pcbi.1003672.g001

Hu, X., Khanzada, S., Klütsch, D., Calegari, F., & Amin, H. (2022). Implementation of biohybrid olfactory bulb on a high-density CMOS-chip to reveal large-scale spatiotemporal circuit information. *Biosensors and Bioelectronics*, *198*. https://doi.org/10.1016/j.bios.2021.113834

Igarashi, K. M., Ieki, N., An, M., Yamaguchi, Y., Nagayama, S., Kobayakawa, K., Kobayakawa, R., Tanifuji, M., Sakano, H., Chen, W. R., & Mori, K. (2012). Parallel mitral and tufted cell pathways route distinct odor information to different targets in the olfactory cortex. *Journal of Neuroscience*, *32*(23), 7970–7985. https://doi.org/10.1523/JNEUROSCI.0154-12.2012

Imai, T. (2014). Construction of functional neuronal circuitry in the olfactory bulb. In *Seminars in Cell and Developmental Biology* (Vol. 35, pp. 180–188). Elsevier Ltd. https://doi.org/10.1016/j.semcdb.2014.07.012

Imamura, F., Ito, A., & LaFever, B. J. (2020). Subpopulations of Projection Neurons in the Olfactory Bulb. In *Frontiers in Neural Circuits* (Vol. 14). Frontiers Media S.A. https://doi.org/10.3389/fncir.2020.561822

Jacobs, L. F. (2012). From chemotaxis to the cognitive map: The function of olfaction. In *Proceedings of the National Academy of Sciences of the United States of America* (Vol. 109, Issue SUPPL.1, pp. 10693–10700). https://doi.org/10.1073/pnas.1201880109

Jacob, V., Monsempès, C., Rospars, J. P., Masson, J. B., & Lucas, P. (2017). Olfactory coding in the turbulent realm. *PLoS Computational Biology*, *13*(12). https://doi.org/10.1371/journal.pcbi.1005870

Jones, P. W., & Urban, N. N. (2018). Mice follow odor trails using stereo olfactory cues and rapid sniff to sniff comparisons Abbreviated title: Following odors using stereo and sniff-sniff change. *BioRxiv*. https://doi.org/10.1101/293746

Jones, S., Zylberberg, J., & Schoppa, N. (2020). Cellular and Synaptic Mechanisms That Differentiate Mitral Cells and Superficial Tufted Cells Into Parallel Output Channels in the Olfactory Bulb. *Frontiers in Cellular Neuroscience*, *14*. https://doi.org/10.3389/fncel.2020.614377

Justus, K. A., Murlis, J., Jones, C., & Cardé, R. T. (2002). Measurement of Odor-Plume Structure in a Wind Tunnel Using a Photoionization Detector and a Tracer Gas. In *Environmental Fluid Mechanics* (Vol. 2).

Kajiya, K., Inaki, K., Tanaka, M., Haga, T., Kataoka, H., & Touhara, K. (2001). *Molecular Bases of Odor Discrimination: Reconstitution of Olfactory Receptors that Recognize Overlapping Sets of Odorants*.

Katada, S., Hirokawa, T., Oka, Y., Suwa, M., & Touhara, K. (2005). Structural basis for a broad but selective ligand spectrum of a mouse olfactory receptor: Mapping the odorant-binding site. *Journal of Neuroscience*, *25*(7), 1806–1815. https://doi.org/10.1523/JNEUROSCI.4723-04.2005

Kay, L. M. (2015). Local Field Potential in Olfaction. In *Encyclopedia of Computational Neuroscience* (pp. 1527–1533). Springer New York. https://doi.org/10.1007/978-1-4614-6675-8

Kay, L. M., Beshel, J., Brea, J., Martin, C., Rojas-Líbano, D., & Kopell, N. (2009). Olfactory oscillations: the what, how and what for. In *Trends in Neurosciences* (Vol. 32, Issue 4, pp. 207–214). https://doi.org/10.1016/j.tins.2008.11.008

Kikuta, S., Fletcher, M. L., Homma, R., Yamasoba, T., & Nagayama, S. (2013). Odorant Response Properties of Individual Neurons in an Olfactory Glomerular Module. *Neuron*, *77*(6), 1122–1135. https://doi.org/10.1016/j.neuron.2013.01.022

Kosaka, K., Toida, K., Aika, Y., & Kosaka, T. (1998). How simple is the organization of the olfactory glomerulus?: the heterogeneity of so-called periglomerular cells. In *Neuroscience Research* (Vol. 30).

Kosaka, T., & Kosaka, K. (2004). Neuronal gap junctions between intraglomerular mitral/tufted cell dendrites in the mouse main olfactory bulb. *Neuroscience Research*, *49*(4), 373–378. https://doi.org/10.1016/j.neures.2004.04.003

Lagier, S., Carleton, A., & Lledo, P. M. (2004). Interplay between Local GABAergic Interneurons and Relay Neurons Generates γ Oscillations in the Rat Olfactory Bulb. *Journal of Neuroscience*, *24*(18), 4382–4392. https://doi.org/10.1523/JNEUROSCI.5570-03.2004

Lei, H., Riffell, J. A., Gage, S. L., & Hildebrand, J. G. (2009). Contrast enhancement of stimulus intermittency in a primary olfactory network and its behavioral significance. *Journal of Biology*, *8*(2). https://doi.org/10.1186/jbiol120

Lewis, S. M., Xu, L., Rigolli, N., Tariq, M. F., Suarez, L. M., Stern, M., Seminara, A., & Gire, D. H. (2021). Plume Dynamics Structure the Spatiotemporal Activity of Mitral/Tufted Cell Networks in the Mouse Olfactory Bulb. *Frontiers in Cellular Neuroscience*, *15*. https://doi.org/10.3389/fncel.2021.633757

Liu, A., Papale, A. E., Hengenius, J., Patel, K., Ermentrout, B., & Urban, N. N. (2019). Mouse navigation strategies for odor source localization. *BioRxiv*. https://doi.org/10.1101/558643

Liu, A., Papale, A. E., Hengenius, J., Patel, K., Ermentrout, B., & Urban, N. N. (2020). Mouse Navigation Strategies for Odor Source Localization. *Frontiers in Neuroscience*, *14*. https://doi.org/10.3389/fnins.2020.00218

Liu, X., & Liu, S. (2018). Cholecystokinin selectively activates short axon cells to enhance inhibition of olfactory bulb output neurons. *Journal of Physiology*, *596*(11), 2185–2207. https://doi.org/10.1113/JP275511

Ly, C., Barreiro, A. K., Gautam, S. H., & Shew, W. L. (2021). Odor-evoked increases in olfactory bulb mitral cell spiking variability. *IScience*, *24*(9), 102946. https://doi.org/10.1016/j.isci.2021.102946

Mafra-Neto, A., & Carde, R. T. (1994). *Fine-scale structure of pheromone plumes modulates upwind orientation of flying moths*.

Mainland, J. D., Lundström, J. N., Reisert, J., & Lowe, G. (2014). From molecule to mind: An integrative perspective on odor intensity. In *Trends in Neurosciences* (Vol. 37, Issue 8, pp. 443–454). Elsevier Ltd. https://doi.org/10.1016/j.tins.2014.05.005

Malnic, B. (2007). Searching for the ligands of odorant receptors. In *Molecular Neurobiology* (Vol. 35, Issue 2, pp. 175–181). Humana Press. https://doi.org/10.1007/s12035-007-0013-2

Margrie, T. W., Sakmann, B., & Urban, N. N. (2000). Action potential propagation in mitral cell lateral dendrites is decremental and controls recurrent and lateral inhibition in the mammalian olfactory bulb. *PNAS*, *98*(1), 319–324.

Margrie, T. W., & Schaefer, A. T. (2003). Theta oscillation coupled spike latencies yield computational vigour in a mammalian sensory system. In *Journal of Physiology* (Vol. 546, Issue 2, pp. 363–374). https://doi.org/10.1113/jphysiol.2002.031245

Markopoulos, F., Rokni, D., Gire, D. H., & Murthy, V. N. (2012). Functional Properties of Cortical Feedback Projections to the Olfactory Bulb. *Neuron*, *76*(6), 1175–1188. https://doi.org/10.1016/j.neuron.2012.10.028

Martinez, D., Burgués, J., & Marco, S. (2019). Fast measurements with MOX sensors: A least-squares approach to blind deconvolution. *Sensors (Switzerland)*, *19*(18). https://doi.org/10.3390/s19184029

Matsutani, S. (2010). Trajectory and terminal distribution of single centrifugal axons from olfactory cortical areas in the rat olfactory bulb. *Neuroscience*, *169*(1), 436–448. https://doi.org/10.1016/j.neuroscience.2010.05.001

Michaelis, B. T., Leathers, K. W., Bobkov, Y. v., Ache, B. W., Principe, J. C., Baharloo, R., Park, I. M., & Reidenbach, M. A. (2020). Odor tracking in aquatic organisms: the importance of temporal and spatial intermittency of the turbulent plume. *Scientific Reports*, *10*(1). https://doi.org/10.1038/s41598-020-64766-y

Mori, K., & Sakano, H. (2020). Olfactory Circuitry and Behavioral Decisions. *Annual Review of Physiology*, 213–256. https://doi.org/10.1146/annurev-physiol-031820

Murlis, J., Elkinton, J. S., & Carde, R. T. (1992). *ODOR PLUMES AND HOW INSECTS USE THEM*. www.annualreviews.org

Murlis, J., Willis, M. A., & Cardé, R. T. (2000). Spatial and temporal structures of pheromone plumes in fields and forests. *Physiological Entomology*, *25*(3), 211–222. https://doi.org/10.1046/j.1365-3032.2000.00176.x

Mylne, K. R., & Mason, P. J. (1991). *Concentration fluctuation measurements in a dispersing plume at a range of up to 1000m* (Vol. 117).

Nagayama, S., Enerva, A., Fletcher, M. L., Masurkar, A. v., Igarashi, K. M., Mori, K., & Chen, W. R. (2010). Differential axonal projection of mitral and tufted cells in the mouse main olfactory system. *Frontiers in Neural Circuits*, *4*(SEP). https://doi.org/10.3389/fncir.2010.00120

Nagayama, S., Homma, R., & Imamura, F. (2014). Neuronal organization of olfactory bulb circuits. In *Frontiers in Neural Circuits* (Vol. 8, Issue SEP). Frontiers Research Foundation. https://doi.org/10.3389/fncir.2014.00098

Nagayama, S., Takahashi, Y. K., Yoshihara, Y., & Mori, K. (2004). Mitral and tufted cells differ in the decoding manner of odor maps in the rat olfactory bulb. *Journal of Neurophysiology*, *91*(6), 2532–2540. https://doi.org/10.1152/jn.01266.2003

Otazu, G. H., Chae, H., Davis, M. B., & Albeanu, D. F. (2015). Cortical Feedback Decorrelates Olfactory Bulb Output in Awake Mice. *Neuron*, *86*(6), 1461–1477. https://doi.org/10.1016/j.neuron.2015.05.023

Pang, R., Lansdell, B. J., & Fairhall, A. L. (2016). *Dimensionality reduction in neuroscience*. https://reader.elsevier.com/reader/sd/pii/S096098221630487O?token=7CB6905EBE5809BDBA7E7E0E859902702EEA5AD5CF43C20D1BF85F974D1FAC572806B41964381945589AB25183AFA775&originRegion=us-east-1&originCreation=20220802195309

Pang, R., van Breugel, F., Dickinson, M., Riffell, J. A., & Fairhall, A. (2018). History dependence in insect flight decisions during odor tracking. *PLoS Computational Biology*, *14*(2). https://doi.org/10.1371/journal.pcbi.1005969

Parabucki, A., Bizer, A., Morris, G., Munoz, A. E., Bala, A. D. S., Smear, M., & Shusterman, R. (2019). Odor concentration change coding in the olfactory bulb. *ENeuro*, *6*(1). https://doi.org/10.1523/ENEURO.0396-18.2019

Park, I. J., Hein, A. M., Bobkov, Y. v., Reidenbach, M. A., Ache, B. W., & Principe, J. C. (2016). Neurally Encoding Time for Olfactory Navigation. *PLoS Computational Biology*, *12*(1). https://doi.org/10.1371/journal.pcbi.1004682

Parsa, P. V., D'Souza, R. D., & Vijayaraghavan, S. (2015). Signaling between periglomerular cells reveals a bimodal role for GABA in modulating glomerular microcircuitry in the olfactory bulb. *Proceedings of the National Academy of Sciences of the United States of America*, *112*(30), 9478–9483. https://doi.org/10.1073/pnas.1424406112

Paseltiner, D., Loeffler, H., Andonian, A., Leberman, A., Gould, T. J., & Castro, J. B. (2020). *Spatially organized genomic and physiological heterogeneity of the olfactory bulb mitral cell layer*. https://doi.org/10.1101/2020.01.13.903823

Pnevmatikakis, E. A., & Giovannucci, A. (2017). NoRMCorre: An online algorithm for piecewise rigid motion correction of calcium imaging data. *Journal of Neuroscience Methods*, *291*, 83–94. https://doi.org/10.1016/j.jneumeth.2017.07.031

Pnevmatikakis, E. A., Soudry, D., Gao, Y., Machado, T. A., Merel, J., Pfau, D., Reardon, T., Mu, Y., Lacefield, C., Yang, W., Ahrens, M., Bruno, R., Jessell, T. M., Peterka, D. S., Yuste, R., & Paninski, L. (2016). Simultaneous Denoising, Deconvolution, and Demixing of Calcium Imaging Data. *Neuron*, *89*(2), 285–299. https://doi.org/10.1016/j.neuron.2015.11.037

Rall, W., & Shepherd, G. M. (1968). Theoretical reconstruction of field potentials and dendrodendritic synaptic interactions in olfactory bulb. *Journal of Neurophysiology*, *31*(6), 884–915. https://doi.org/10.1152/jn.1968.31.6.884

Rapp, H., & Nawrot, M. P. (2020). *A spiking neural program for sensorimotor control during foraging in flying insects*. *117*(45), 28412–28421. https://doi.org/10.1073/pnas.2009821117/-/DCSupplemental.y

Ressler, K. J., Sullivan, S. L., & Buck, L. 8. (1993). A Zonal Organization of Odorant Receptor Gene Expression in the Olfactory Epithelium. In *Cell* (Vol. 73).

Ressler, K. J., Sullivan, S. L., & Buck, L. B. (1994). *Information Coding in the Olfactory System: Evidence for a Stereotyped and Highly Organized Epitope Map in the Olfactory Bulb* (Vol. 79).

Rigolli, N., Magnoli, N., Rosasco, L., & Seminara, A. (2021). *Learning to predict target location with turbulent odor plumes*. http://arxiv.org/abs/2106.08988

Rojas-Líbano, D., & Kay, L. M. (2008). Olfactory system gamma oscillations: The physiological dissection of a cognitive neural system. In *Cognitive Neurodynamics* (Vol. 2, Issue 3, pp. 179–194). https://doi.org/10.1007/s11571-008-9053-1

Roux, S. G., Cenier, T., Garcia, S., Litaudon, P., & Buonviso, N. (2007). A wavelet-based method for local phase extraction from a multi-frequency oscillatory signal. A wavelet-based method for local phase extraction from a multi-frequency oscillatory signal. *Journal of Neuro-Science Methods*, *160*(1), 135–178. https://doi.org/10.1016/j.jneumeth.2006.09.001ï

Schikorski, T., & Stevens, C. F. (1999). Quantitative fine-structural analysis of olfactory cortical synapses. In *Neurobiology* (Vol. 96). www.pnas.org.

Schoppa, N. E., & Urban, N. N. (2003). Dendritic processing within olfactory bulb circuits. In *Trends in Neurosciences* (Vol. 26, Issue 9, pp. 501–506). Elsevier Ltd. https://doi.org/10.1016/S0166-2236(03)00228-5

Schoppa, N. E., & Westbrook, G. L. (2001). Glomerulus-Specific Synchronization of Mitral Cells in the Olfactory Bulb circuit interactions could enhance or disrupt an odor-induced spatial map depending on the pattern of activity within subpopulations of mitral cells. In *Neuron* (Vol. 31).

Shipley, M. T., & Ennis, M. (1996). Functional Organization of Olfactory System. *Journal of Neurobiology*.

Smear, M., Shusterman, R., O'Connor, R., Bozza, T., & Rinberg, D. (2011). Perception of sniff phase in mouse olfaction. *Nature*, *479*(7373), 397–400. https://doi.org/10.1038/nature10521

Spors, H., & Grinvald, A. (2002). Spatio-Temporal Dynamics of Odor Representations in the Mammalian Olfactory Bulb. *Neuron*, 301–315.

Steinmetz, N. A., Aydin, C., Lebedeva, A., Okun, M., Pachitariu, M., Bauza, M., Beau, M., Bhagat, J., Böhm, C., Broux, M., Chen, S., Colonell, J., Gardner, R. J., Karsh, B., Kloosterman, F., Kostadinov, D., Mora-Lopez, C., O'Callaghan, J., Park, J., … Harris, T. D. (2021). Neuropixels 2.0: A miniaturized high-density probe for stable, long-term brain recordings. *Science*, *372*(6539). https://doi.org/10.1126/science.abf4588

Stern, M., Shea-Brown, E., & Witten, D. (2020). *Inferring the Spiking Rate of a Population of Neurons from Wide-Field Calcium Imaging*. https://doi.org/10.1101/2020.02.01.930040

Storace, D. A., & Cohen, L. B. (2017). Measuring the olfactory bulb input-output transformation reveals a contribution to the perception of odorant concentration invariance. *Nature Communications*, *8*(1). https://doi.org/10.1038/s41467-017-00036-2

Storace, D. A., & Cohen, L. B. (2021). The mammalian olfactory bulb contributes to the adaptation of odor responses: A second perceptual computation carried out by the bulb. *ENeuro*, *8*(5). https://doi.org/10.1523/ENEURO.0322-21.2021

Tan, J., Savigner, A., Ma, M., & Luo, M. (2010). Odor Information Processing by the Olfactory Bulb Analyzed in Gene-Targeted Mice. *Neuron*, *65*(6), 912–926. https://doi.org/10.1016/j.neuron.2010.02.011

Tank, D. W., Gelperin, A., & Kleinfeld, D. (1994). Odors, Oscillations, and Waves: Does It All Compute? *Science*.

Tariq, M. F., Lewis, S. M., Lowell, A., Moore, S., Miles, J. T., Perkel, D. J., & Gire, D. H. (2021). Using head-mounted ethanol sensors to monitor olfactory information and determine behavioral changes associated with ethanol-plume contact during mouse odor-guided navigation. *ENeuro*, *8*(1), 1–12. https://doi.org/10.1523/ENEURO.0285-20.2020

Uchida, N., & Mainen, Z. F. (2003). Speed and accuracy of olfactory discrimination in the rat. *Nature Neuroscience*, *6*(11), 1224–1229. https://doi.org/10.1038/nn1142

Uytingco, C. R., Puche, A. C., & Munger, S. D. (2016). Interglomerular connectivity within the canonical and GC-D/Necklace olfactory subsystems. *PLoS ONE*, *11*(11). https://doi.org/10.1371/journal.pone.0165343

Vassar, R., Chao, S. K., Sitcheran, R., Nuiiez, M., Vosshall, L. B., & Axel, R. (1994). Topographic Organization of Sensory Projection to the Olfactory Bulb. In *Cell* (Vol. 79).

Vergassola, M., Villermaux, E., & Shraiman, B. I. (2007). "Infotaxis" as a strategy for searching without gradients. *Nature*, *445*(7126), 406–409. https://doi.org/10.1038/nature05464

Verhagen, J. v., Wesson, D. W., Netoff, T. I., White, J. A., & Wachowiak, M. (2007). Sniffing controls an adaptive filter of sensory input to the olfactory bulb. *Nature Neuroscience*, *10*(5), 631–639. https://doi.org/10.1038/nn1892

Vickers, N. J. (2000). *Mechanisms of Animal Navigation in Odor Plumes*.

Vickers, N. J. (2006). Winging it: Moth flight behavior and responses of olfactory neurons are shaped by pheromone plume dynamics. *Chemical Senses*, *31*(2), 155–166. https://doi.org/10.1093/chemse/bjj011

Vickers, N. J., & Baker, T. C. (1996). Latencies of behavioral response to interception of filaments of sex pheromone and clean air influence flight track shape in Heliothis virescens (F.) males. *Journal of Comparative Physiology A: Sensory, Neural, and Behavioral Physiology*, *178*(6), 831–847. https://doi.org/10.1007/BF00225831

Vladimirov, N., & Sourjik, V. (2009). Chemotaxis: How bacteria use memory. In *Biological Chemistry* (Vol. 390, Issue 11, pp. 1097–1104). https://doi.org/10.1515/BC.2009.130

Wachowiak, M., & Cohen, L. B. (2001). Representation of Odorants by Receptor Neuron Input to the Mouse Olfactory Bulb typed locations of the olfactory bulb (Vassar et al odorant-evoked activity of receptor neurons distributed. In *Neuron* (Vol. 32). Thus.

Wachowiak, M., Denk, W., & Friedrich, R. W. (2004). *Functional organization of sensory input to the olfactory bulb glomerulus analyzed by two-photon calcium imaging*. www.pnas.orgcgidoi10.1073pnas.0400438101

Wachowiak, M., & Shipley, M. T. (2006). Coding and synaptic processing of sensory information in the glomerular layer of the olfactory bulb. In *Seminars in Cell and Developmental Biology* (Vol. 17, Issue 4, pp. 411–423). Elsevier Ltd. https://doi.org/10.1016/j.semcdb.2006.04.007

Webster, D. R., Rahman, S., & Dasi, L. P. (2001). On the usefulness of bilateral comparison to tracking turbulent chemical odor plumes. In *Limnol. Oceanogr* (Vol. 46, Issue 5).

Webster, D. R., & Weissburg, M. J. (2001). Chemosensory guidance cues in a turbulent chemical odor plume. In *Limnol. Oceanogr* (Vol. 46, Issue 5).

Wilson, C. D., Serrano, G. O., Koulakov, A. A., & Rinberg, D. (2017). A primacy code for odor identity. *Nature Communications*, *8*(1). https://doi.org/10.1038/s41467-017-01432-4

Wright, G. A., & Thomson, M. G. A. (2005). *ODOR PERCEPTION AND THE VARIABILITY IN NATURAL ODOR SCENES*.

Wróbel, J., Kublik, E., Wójcik, D. K., Whittington, M. A., & Hunt, M. J. (2020). Network and synaptic mechanisms underlying high frequency oscillations in the rat and cat olfactory bulb under ketamine-xylazine anesthesia. *BioRxiv*. https://doi.org/10.1101/2020.07.23.217604

Wu, R., Liu, Y., Wang, L., Li, B., & Xu, F. (2017). Activity patterns elicited by airflow in the olfactory bulb and their possible functions. *Journal of Neuroscience*, *37*(44), 10700–10711. https://doi.org/10.1523/JNEUROSCI.2210-17.2017

Xu, F., Greer, C. A., & Shepherd, G. M. (2000). *Odor Maps in the Olfactory Bulb*. https://doi.org/10.1002/1096-9861(20000710)422:4<489::AID-CNE1>3.0.CO;2

Yeung, P. K., & Pope, S. B. (1992). Differential diffusion of passive scalars in isotropic turbulence. *Physics of Fluids A*, *5*(10), 2467–2478. https://doi.org/10.1063/1.858760

Young, B. D., Escalon, J. A., & Mathew, D. (2020). Odors: from chemical structures to gaseous plumes. In *Neuroscience and Biobehavioral Reviews* (Vol. 111, pp. 19–29). Elsevier Ltd. https://doi.org/10.1016/j.neubiorev.2020.01.009

Yu, Y. S. W., Graff, M. M., Bresee, C. S., Man, Y. B., & Hartmann, M. J. Z. (2016). Whiskers aid anemotaxis in rats. *Science Advances*, *2*(8). https://doi.org/10.1126/sciadv.1600716

Zak, J. D., Reddy, G., Vergassola, M., & Murthy, V. N. (2020). Antagonistic odor interactions in olfactory sensory neurons are widespread in freely breathing mice. *Nature Communications*, *11*(1). https://doi.org/10.1038/s41467-020-17124-5

Zhou, Z., & Belluscio, L. (2012). Coding Odorant Concentration through Activation Timing between the Medial and Lateral Olfactory Bulb. *Cell Reports*, *2*(5), 1143–1150. https://doi.org/10.1016/j.celrep.2012.09.035

Appendix

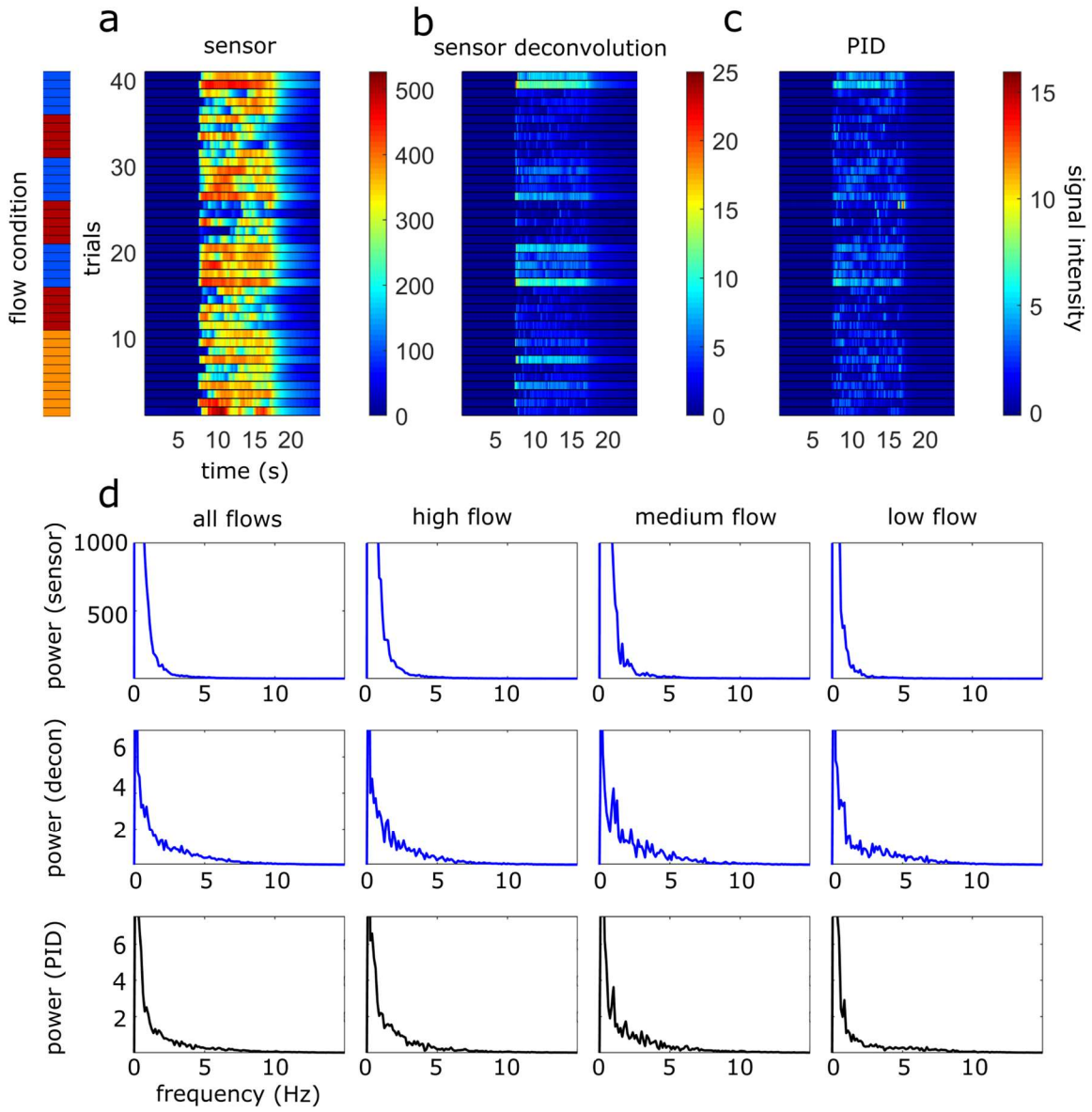

Chapter 2 Supplemental Figure 1: Deconvolved Ethanol signal and spectral decomposition from one session divided by flow type.
a) The raw ethanol sensor output is shown for all trials within a single session (n = 40). (red, orange, and blue flow condition depict high, medium and low flow respectively). b) The deconvolution of the raw ethanol signal. c) The simultaneously recorded signal from a co-localized PID. Sensor deconvolution and PID are significantly correlated as calculated during plume presentations (r = .3089, p < .001). d) (top) The spectral decomposition calculated across all trials or within flow conditions for the raw sensor signal shown in (a). Only the middle 8 seconds of the 10 second plume presentation are analyzed to avoid onset or offset dynamics. Spectral decompositions are also plotted for the ethanol deconvolution (middle) shown in (b) and for the PID (bottom) shown in (c).

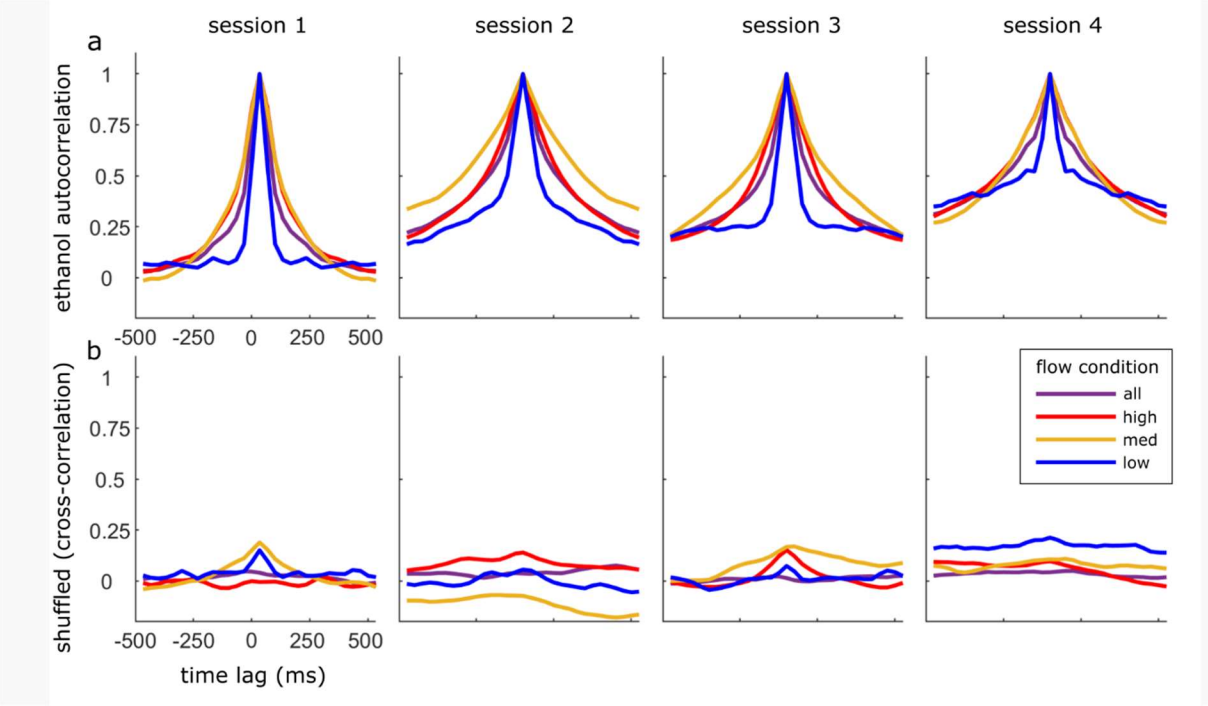

Chapter 2 Supplemental Figure 2: Normalized Autocorrelation of Ethanol trace.
a) The Normalized average autocorrelation of the deconvolved ethanol signal is plotted for each of the 4 experimental sessions showing that for all flow conditions, plume dynamics are stochastic and do not correlate across time within trials. Traces are calculated across all trials within the designated flow conditions. b) Same as (a) but trials are shuffled within session such that each cross-correlation is calculated between the deconvolved ethanol signal from two different trials. Plotted cross-correlations show concentration dynamics are not correlated across plumes.

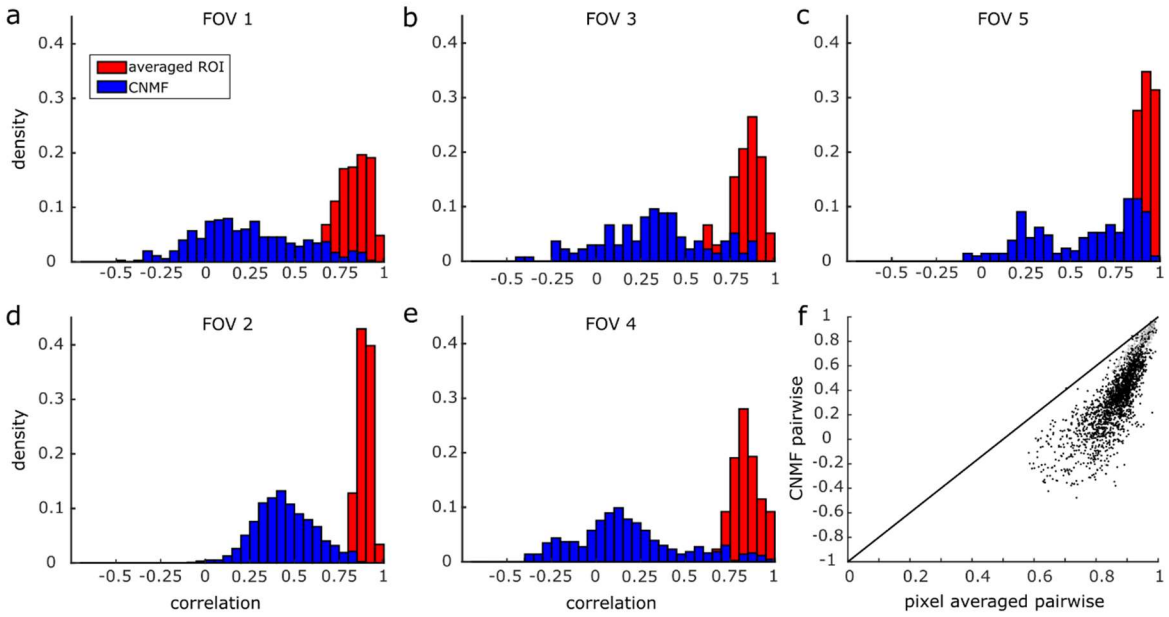

Chapter 2 Supplemental Figure 3: Pairwise correlations between glomerular ROIs are decorrelated by CNMF.
a-e) Distributions of the pairwise linear correlation coefficients from all possible glomerular pairs within each FOV. Correlations are calculated on the temporal decomposition of CNMF ROI signals (without deconvolution) which include denoising and demixing (blue) or on the raw pixel values as averaged within the same ROI boundaries (red). Pairwise correlations are calculated between the two glomeruli during stimulus presentation. f) Scatterplot of each pairwise correlation shows CNMF denoising decorrelates the signal for each pair of glomeruli. Pairwise correlations in grey are from ROI pairs that have been considered to originate from the same glomerulus after the merging threshold analysis (Supplemental Fig. 4).

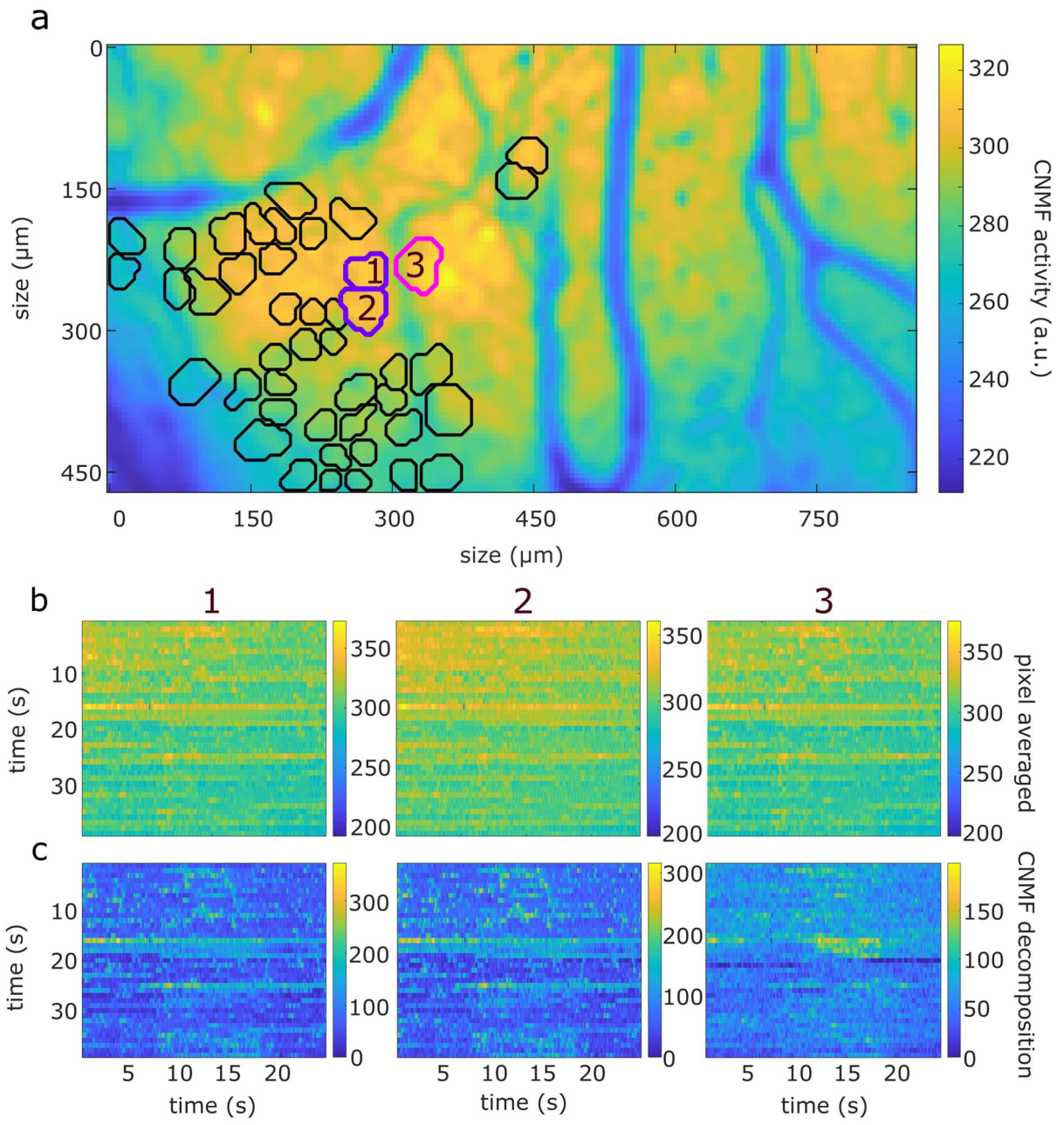

Chapter 2 Supplemental Figure 4: Detecting oversegmentation of ROIs after CNMF decomposition.

a) ROI segmentation of glomeruli for FOV 4 using CNMF spatial decomposition of activity across an entire session. ROIs circled in purple do not meet thresholds for independent ROIs (methods) and thus are considered to originate from the same glomerulus, while the ROI in magenta is considered to be a separate glomerulus. b) Raw fluorescent signal averaged across all pixels within each of the 3 ROIs (without denoising or de-mixing) is plotted for all trials in the

session. Numbers above each plot refer to ROI numbering in panel (a). c) CNMF signal (without deconvolution) across all trials plotted for the corresponding ROIs in (b).

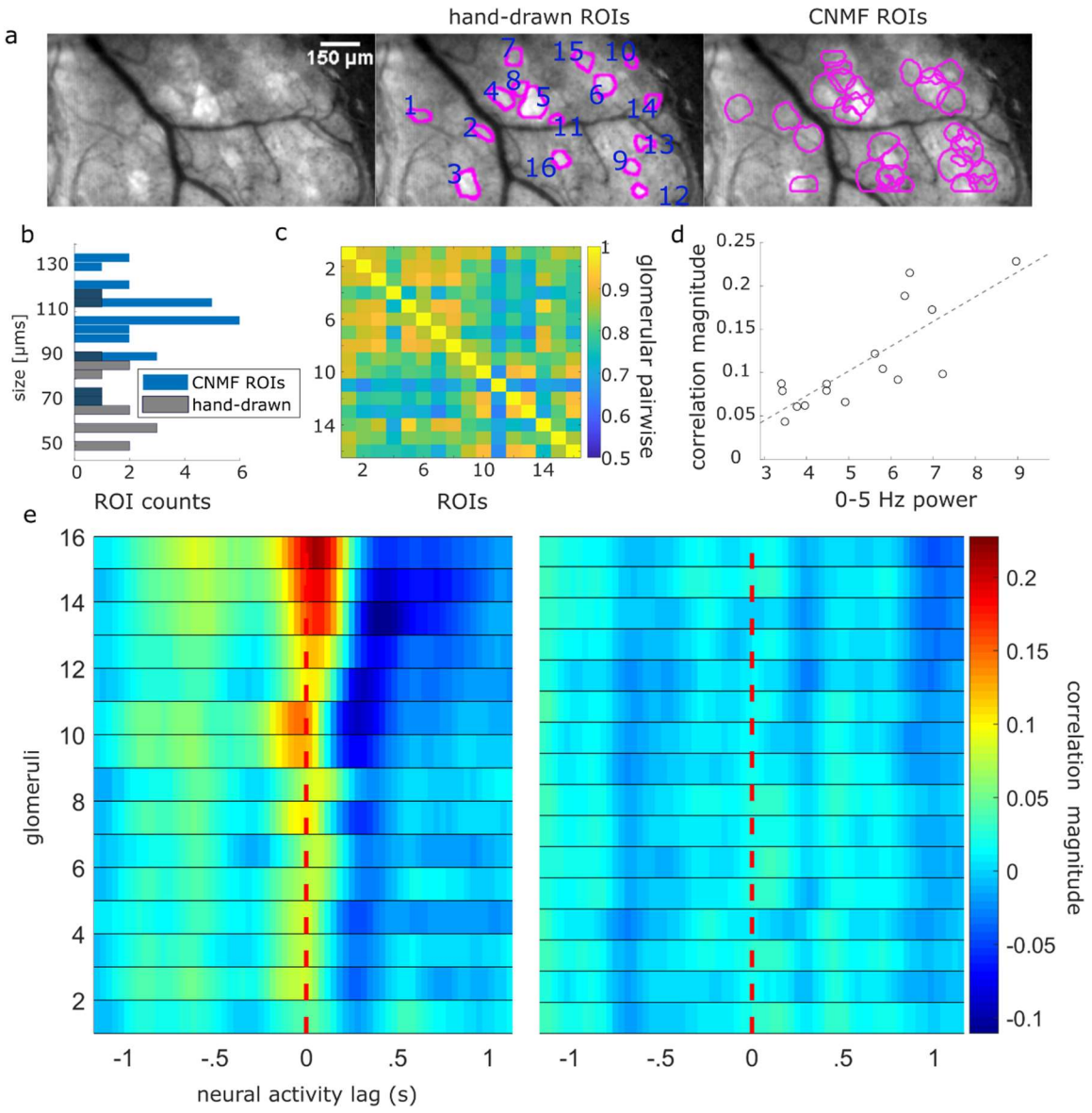

Chapter 2 Supplemental Figure 5: Hand-drawn ROIs have qualitatively similar results but higher pairwise correlations.

a) (left) St. dev projection of a single FOV during the first trial of the session. (middle) ROIs from hand-drawn analysis are plotted over the projected st. dev (left). ROIs determined using recordings and st. dev projections averaged across trials within each flow condition. (right) Same but CNMF ROIs are plotted. b) Distribution of hand-drawn ROI sizes (grey) plotted against the CNMF ROI sizes (blue) found for the same FOV. The size distribution of the hand-drawn analysis was significantly smaller than that of the CNMF analysis ($z = 3.94$, $p < 0.001$). c) Trial averaged linear pairwise correlation coefficients of ROI activity during plume presentations shows high correlations between ROIs. d) A glomerulus's correlation with odor dynamics (tracking/correlation magnitude) is plotted against their corresponding change in response power (0-5 Hz) between 'odor off' and 'odor on' periods showing glomeruli with higher correlation coefficients have higher activity power ($r = 0.80$, $p = <0.001$). The dotted line plots the line of

best fit using OLS regression. f) Glomerular activity is correlated with stimulus dynamics at varying lags (left) with all mean coefficients exceeding a 95\% confidence interval of their shuffled mean coefficients. Each row is a glomerulus (hand-drawn ROI) and each time point represents the mean correlation coefficient between odor and response deconvolutions at the indicated lag. Glomeruli are sorted in order of decreasing correlation. (right) Same but neural activity responses are shuffled so that the signals compared are not from the same trial. The glomeruli are sorted to match their corresponding unshuffled cross-correlation in the left panel.

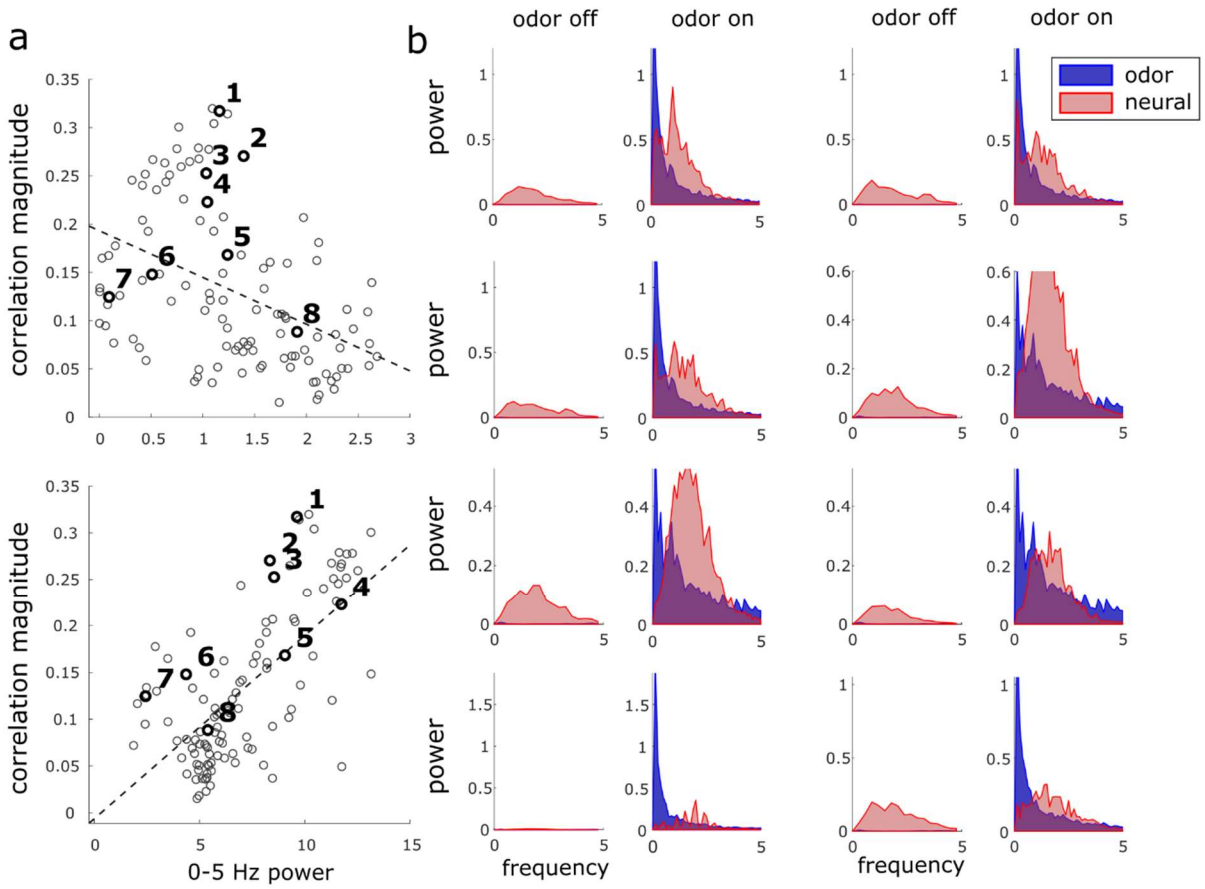

Chapter 2 Supplemental Figure 6: 0-5 Hz Power spectrums for odor and glomerular responses.
a) Average correlation magnitude (tracking ability) for each glomerulus is plotted against the power spectrum of its activity during 'odor off' (top) or 'odor on' (bottom) periods, illustrating the before and after states of the change in response power plotted in Figure 6d. b) The average power spectrums across trials of the glomerular (red) traces and the deconvolved odor (blue) to which the glomerulus responses are plotted for 8 example glomeruli (numbered accordingly in (a)) during 'odor off' and 'odor on' periods.

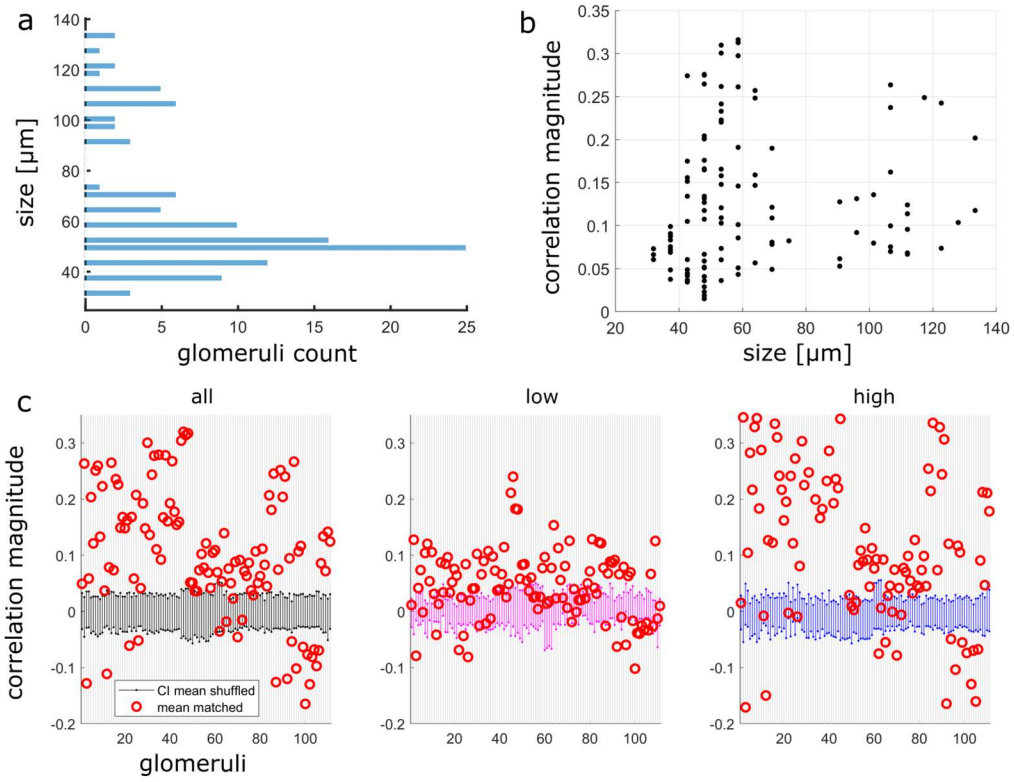

Chapter 2 Supplemental Figure 7: Glomerular sizing and plume following behavior.
a) Distribution of CNMF ROI sizes for all sessions (µm). b) ROI size (µm) plotted against the mean correlation coefficient between deconvolved glomerular and ethanol signals during odor presentation shows correlations between ROIs and plume dynamics are not driven exclusively by singular MT cell activity. Kendall's tau coefficient between size and odor concentration tracking ($r_\tau = 0.16, p = 0.20$) shows that correlation to plume dynamics is not exclusive to or related to smaller sized ROIs (ROIs similarly sized to individual MT cells). This suggests response to plume dynamics across plume encounters is also occurring at the glomerular level. c) Mean correlation coefficients of glomeruli (red) are plotted against their respective bootstrapped 95% confidence interval of null mean coefficients (see methods for trial shuffled bootstrap analysis). Null confidence intervals are calculated across all flow conditions (black), within low (pink) and within high (blue) flow.

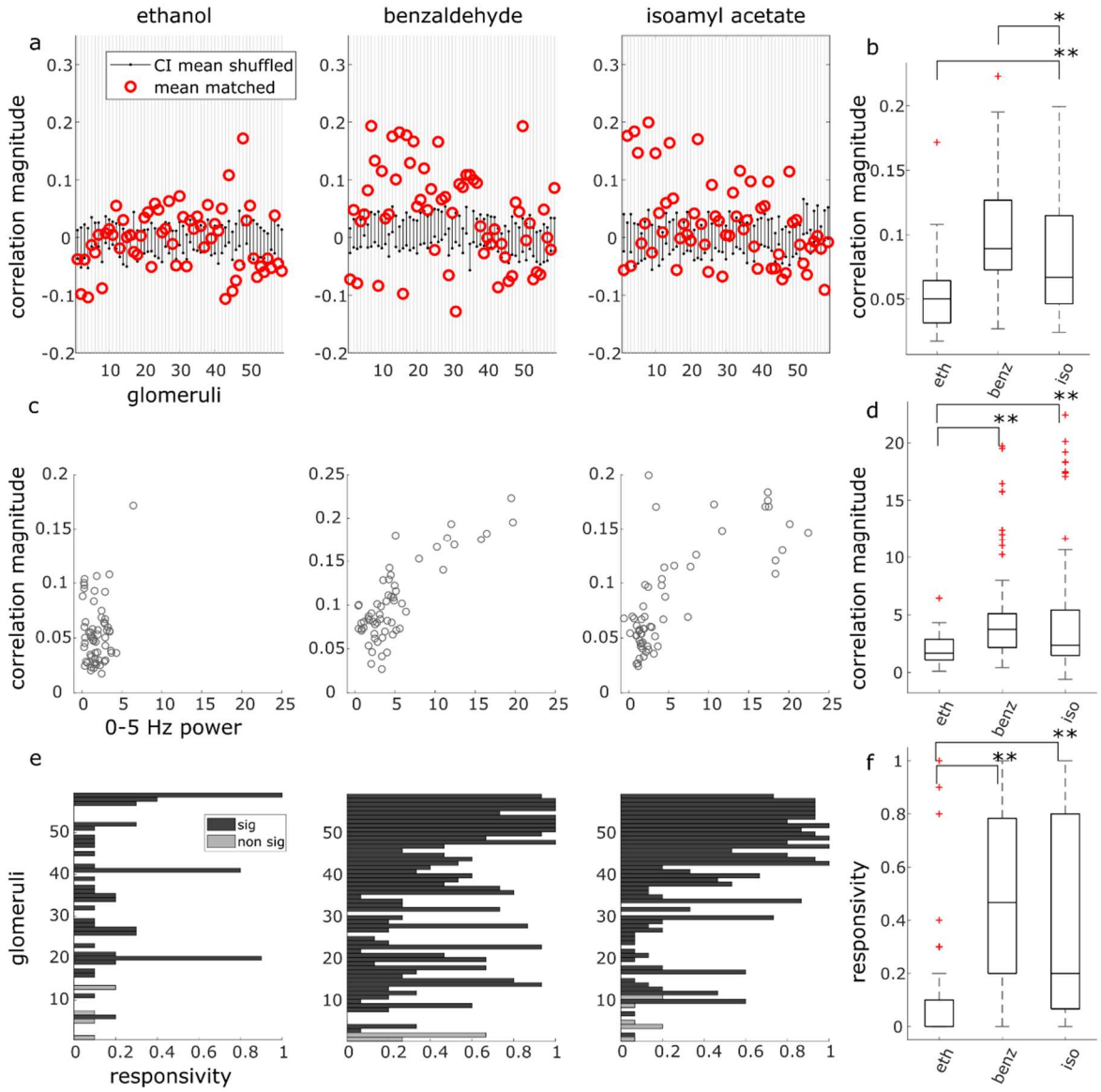

Chapter 2 Supplemental Figure 8: Significant tracking of odor concentration dynamics is observed across odors.

a) Mean correlation coefficients of glomeruli (red) are plotted against their respective bootstrapped 95% confidence interval of null mean coefficients (black). Null confidence intervals are calculated within odor type. b) Box plot shows absolute value distributions of correlation magnitude plotted for each odor in (a) where the central line indicates the median, boxes indicate 25th and 75th percentiles, whiskers indicate min and max distribution values, and outliers are plotted in red. c) Calculated within odor type, correlation magnitude (tracking ability) of the glomerulus with plume dynamics is plotted against its corresponding increase in response power (0-5 Hz) activity between 'odor off' and 'odor on' periods. This relationship is significantly correlated for both odor mixtures, but not for ethanol alone ($r = 0.12$, $p = 0.152$, $r = 0.81$, $p = <0.001$, $r = 0.74$; $p = <0.001$; ethanol, benzaldehyde, and isoamyl acetate respectively). d) Box plot of change in response power distributions for the glomerular population for each

odor depicted in (c). Repeated measures ANOVA shows significant differences in response power change of the glomerular population between ethanol and odor mixtures ($F(2, 116) = 8.06$, $p < 0.001$). e) The responsivity of each glomerulus to the specified odor is plotted. Glomeruli are sorted by decreasing average correlation with plume dynamics during the specified odor (top to bottom). Glomeruli whose correlation coefficient exceeds its null confidence interval in at least one odor condition are plotted in dark grey as significantly tracking (sig, n=54) and the minority of glomeruli that do not (non sig, $n = 5$) are plotted in light grey. Responsivity was significantly correlated with tracking ability for all odor conditions ($r = 0.36$, $p < 0.01$, $r = 0.66$, $p = <0.001$, $r = 0.82$, $p <0.001$; ethanol, benzaldehyde, and isoamyl acetate respectively). f) Box plot of responsivity distributions for the glomerular population for each odor depicted in (f). Repeated measures ANOVA shows significant differences in responsivity between ethanol and odor mixtures ($F(2, 116) = 29.2$, $p<0.001$).